Coupled Electro-Thermal Transmission Line Modelling (TLM) Method

Ahmed Elkalsh, BEng(Hons)

Thesis submitted to The University of Nottingham

for the degree of Doctor of Philosophy, September 2016

Abstract

The theme of this thesis is concerned with the modelling of the multi-physics interactions that occur in lightning and arc discharge. The main contributions of this research are presented as combining different physical studies namely, electromagnetic (EM) propagation, thermal diffusion and non-linear materials using a numerical algorithm. The algorithm was developed based on the two dimensional (2D) numerical transmission line method (TLM). The algorithm was applied to several practical examples namely, to model the electro-thermal analysis and the temperature development in a plasmonic nano-heat sources for terahertz applications; to predict the shape and the location of an arc discharge channel caused by a lightning strike using electro-thermal analysis, and to model diverter strips for lightning protection on aeroplanes. Different electro-thermal coupling approaches, such as fully and partially coupled methods were used to investigate the efficiency and accuracy of the model. In the fully coupled method the thermal model was allowed to change the electrical properties of materials in the electromagnetic model. On the other hand partial coupling did not consider the temperature dependency of the electrical properties in the electromagnetics model. Both of the models used the dissipated power from the electromagnetic model as a source signal to evaluate the temperature profile in the thermal model. Also different coupling interval timesteps were investigated to minimize the computational power needed without affecting the model accuracy.

Acknowledgements

During my PhD journey, I have received immeasurable support from many individuals who have made this thesis possible. First and foremost, I would like to express my deepest gratitude to my main supervisor, Dr Ana Vukovic for her unwavering support during my studies. I would like to thank Ana for being so approachable and understanding during the times of hardship. Thank you for the countless times where you were so patient reading my work and suggesting improvements. I would like to thank Prof Philip Sewell for the fruitful discussions, enlightening suggestions and questions. Without these inputs, it would not have been possible to complete this work. I would like to thank Prof Trevor Benson for the support and help during the preparation of the publications, where he provided immense patience and advice during my learning process for writing journals.

I would like to thank the GGIEMR group members for the fun times and the interesting discussions during my academic work and outside. Thank you all DR Xuesong Meng(Vicky), Dr Sendy Phang, Dr Daniel Simmons, Dr Brian Teo, Dr Hayan Nasser, Zhang Zhewen(Edward), Latifa Abdul Aziz, Dr Afonos almeida, Najla Najeeb, Lu Zhengyu and Andrew Morley.

I would like to thank my second family who have shared the experiences with me as a welfare tutor at the university. You have been supportive and patient with me during my writing up period, and covering my duties when extra work was needed for my PhD. Thank you Prof Glenn McDowell, Dr Lina Bader, Minh Hoang(Harry), Connor Jones, Dr Spandan karla, Yousuf Mansoor, Dr Tiziana Marrocco, Georgina Marsh, Nirav Nagda, Mina Tahsiri and Long Van.

None of this would have been possible without the support of my family and my mother Magda who brought me up and put me up on the right track early in life. Thank you mother, I am in your debt for as long I live. I would like to thank my father Ibrahim, who has shaped the core of who I am today as a person, and who would be very proud if he had lived to witness my achievements.

Last but not least I would like to thank my wife Kamr. Her unwavering love, patience, encouragement and tremendous support during all stages of my PhD has made it a much easier and better experience.

Publications related to this thesis

Peer reviewed journal articles:

[J1] **A. Elkalsh**, A. Vukovic, P. Sewell, and T. M. Benson, "Electro-thermal modelling for plasmonic structures in the TLM method," Optical and Quantum Electronics 48: 263 (2016).

Publications in conference proceedings:

[C1] **A. Elkalsh**, A. Vukovic, P. Sewell, and, T. Benson, "Coupled electromagnetic - thermal model for arc discharge in plasma," in 9th IET International Conference on Computation in Electromagnetics (CEM 2014), London, UK.

[C2] **A. Elkalsh**, A. Vukovic, P. Sewell, and, T. Benson, "Coupled arc discharge models in the TLM method," in 2015 IEEE International Symposium on Electromagnetic Compatibility (EMC), Dresden, Germany pp. 987 - 990.

Conferences with abstract:

[A1] **A. Elkalsh**, A. Vukovic, P. Sewell, and, T. Benson, "Coupled Electromagnetic Thermal Model for Plasmonic Waveguides," in Optical Wave and Waveguide Theory and Numerical Modelling Workshop (2015), London, UK.

Contents

List of Symbols

This list includes all symbols that are frequently used in this thesis.

Symbol	Description	Unit	First used
$\mathbf{E}$	Electric field vector (TD*)	V/m	(2.1a)
$\mathbf{H}$	Magnetic field vector (TD)	A/m	(2.1a)
$\mathbf{B}$	Magnetic flux density vector (TD)	Wb/m^2	(2.1a)
$\mathbf{J_m}$	Magnetic voltage density vector (TD)	V/m^2	(2.1a)
$\mathbf{D}$	Electric flux density vector (TD)	C/m^2	(2.1b)
$\mathbf{J_e}$	Electric current density vector (TD)	A/m^2	(2.1b)
ε	Electric permittivity	F/m	(2.1c)
μ	Magnetic permeability	H/m	(2.1d)
R	Resistance	Ohm	(2.9)
L	Inductance	Henry	(2.9)
C	Capacitance	Farad	(2.10)
G	Admittance	S	(2.10)
t	Time	s	(2.16)
Z_{TL}	Characteristic impedance of transmission line	Ohm	(2.17)
c	Speed of light in free space	m/s	(2.31)
ε_o	Electric permittivity of free Space	F/m	(2.31)
μ_o	Magnetic permeability of free space	H/m	(2.31)
Z_o	Impedance of free space	Ohm	(2.32)
ε_r	Electric relative permittivity	–	(2.33)
χ_e	Electric susceptibility	–	(2.33)

*Time-Domain

$\overline{\mathcal{E}}$	Electric field vector (FD[†])	V/m	(2.41)
$\overline{\mathcal{H}}$	Magnetic field vector (FD)	A/m	(2.41)
$\overline{\mathcal{B}}$	Magnetic flux density vector (FD)	$\mathrm{Wb/m^2}$	(2.41)
$\overline{\mathcal{J}}_m$	Magnetic voltage density vector (FD)	$\mathrm{V/m^2}$	(2.41)
$\overline{\mathcal{D}}$	Electric flux density vector (FD)	$\mathrm{C/m^2}$	(2.41)
$\overline{\mathcal{J}}_e$	Electric current density vector (FD)	$\mathrm{A/m^2}$	(2.41)
ω	Angular frequency	rad/s	(2.42)
χ_m	Magnetic susceptibility	–	(2.43)
σ_e	Electrical conductivity	S/m	(2.44)
σ_m	Magnetic resistivity	Ω/m	(2.45)
s	Laplace complex frequency variable	1/s	(2.54)
$\bar{s}$	Normalised Laplace variable	–	(2.54)
z	Time shift operator (Z-transform)	–	(2.54)
$\mathbf{q}_{th}$	Heat flux	$\mathrm{W/m^2}$	(3.1)
k_{th}	Thermal conductivity	W/m.K	(3.1)
T	Temperature	K	(3.1)
c_v	Specific heat capacities at constant volume	J/kg K	(3.5)
c_p	Specific heat capacities at constant pressure	J/kg K	(3.5)
ρ	Volumetric mass density	$\mathrm{kg/m^3}$	(3.9)
ω_p	Plasma frequency	rad/s	(4.1)
ν_c	Collision frequency	1/s	(4.1)
j	Imaginary number $\sqrt{-1}$	–	(4.1)
P_d	Dissipated power	$\mathrm{W/m^2}$	(4.13)

[†]Frequency-Domain

List of Abbreviations

CFC	Carbon Fibre Composites.
EM	Electromagnetic.
BEM	Boundary Element Method.
FDTD	Finite Difference Time Domain Method.
FEM	Finite Element Analysis.
MOM	Method Of Moments.
TLM	Transmission Line Method.
EM-TLM	Electromagnetic Transmission Line Modelling Method.
SP	Surface Plasmon.
SPP-WBG	Surface Plasmon Polariton Waveguide Bragg Grating.

1

Introduction

This chapter present the overall background and introduction to this thesis. It highlights the general gap in the research that this thesis addresses. Also it demonstrates the need of such research and the importance of it in real life engineering applications. This is then followed by an overview of the content of each chapter and how they fit in the overall view of this thesis.

1.1 Introduction and overview

Lightning power since the dawn of history was a mystery and even a symbol of God power in the ancient Greek myth. Scientists and engineers succeeded in harnessing the power of electricity and commercially producing it in the late 19th Century; however, they are still challenged to fully understand lightning. The best example to demonstrate the limited knowledge humans have about lightning is the lack of understanding of the unexplained ball lightning phenomenon. Ball lightning is a semi-spherical structure that accompanies lightning on rare occasions that has a steady glow for 1-5 seconds and mostly horizontal movements [1.1]. The phenomena was thought to be a myth until the 1960s when its existence was acknowledged by

scientists [1.2]; the spectral analysis of this phenomenon was first reported in 2014 in [1.3].

The destructive power of lightning was always a concern for design engineers when designing a new building or an aircraft due to the unpredictable nature of lightning. Several models have been developed for shielding buildings and objects against lightning strikes such as the rolling sphere model [1.4]. The rolling sphere model assumes that the striking distances to the ground, a wire or a mast are equal therefore evaluates the objects surrounding area that is shielded against direct lightning strikes. This method, as shown in Figure 1.1, uses a rolling virtual sphere of radius (S) to determine the exposed and the protected areas. All the objects below the lower curve of the imaginary bath of the rolling sphere are said to be protected [1.2,1.5].

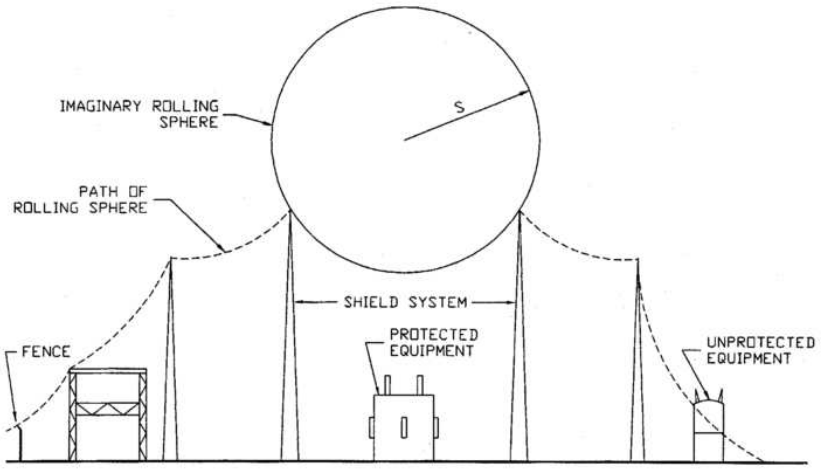

Figure 1.1: Principle of rolling sphere showing the protected area below the imaginary rolling sphere. Copyright © 1996, IEEE [1.2]

The lightning protection for very tall objects such as skyscrapers follows another approach by providing a metal rod that attracts the lightning column towards it, hence diverting the lightning current away from the building or the object [1.6]. The metal rod approach uses the singular nature of the field around sharp metal corners [1.7] to provide an attractive charge so that the lightning is more likely to hit the highly charged metal. Also undesirably for the same reason, lightning strikes

are attracted to overhead power distributed lines due their height and charge which causes a hazardous disturbance to power network systems. Different protection measures are used against lightning strikes in this case, such as surge arresters and periodically grounded shield wires as shown in [1.8,1.9]. All of these different structures and objects can avoid being hit by lightning following these protection measures but an aircraft flying in close proximity to the clouds where discharges are more likely to occur cannot escape lightning.

Commercial planes are hit by lightning once per year on average and these lightning strikes were the cause of several accidents and crashes such as the one in 1963 [1.10]. Due to the complexity of the lightning phenomenon scientists are not able to locate the exact location where the lightning strike will hit, but over time a statistical and experimental data have shown that some areas like the plane nose and wings are more likely to be hit by lightning than other parts of the plane. These data are usually considered when designing protection system for an aeroplane. To date several approaches were developed for aircraft protection against lightning strikes, such as using the Faraday cage concept by coating non-conductive materials with conducting paint or a metal grid [1.11]. The Faraday cage allows the lightning current to pass over the surface of the conducing material without being leaked to the sensitive instruments and fuel tanks [1.11]. However, in the past decade the interest in carbon fibre composites (CFCs) in aircraft manufacturing has hugely increased due to their high strength-to-weight ratio and low weight [1.12]. Despite their remarkable strength, CFCs are not as conductive as aluminium which makes them susceptible to lightning strike and secondary electrical breakdown. Examples of the damage caused by lightning strike current on a CFC panel and an aluminium plate are shown in figs. 1.2 and 1.3 respectively. The carbon composites suffers from mechanical damage when exposed to intensive current due to the gas emissions at high temperature. On the other hand metals are less affected by lightning current and the damage can be further reduced using special paints.

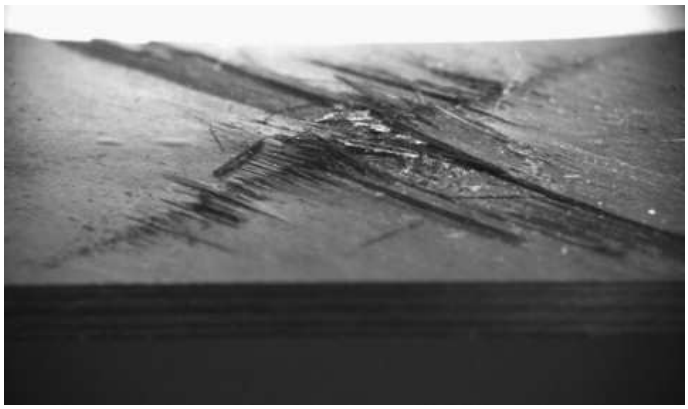

Figure 1.2: The damage caused by lightning current to CFC surface at 50kA of typical lightning strike, Copyright © 2009, Elsevier [1.13]

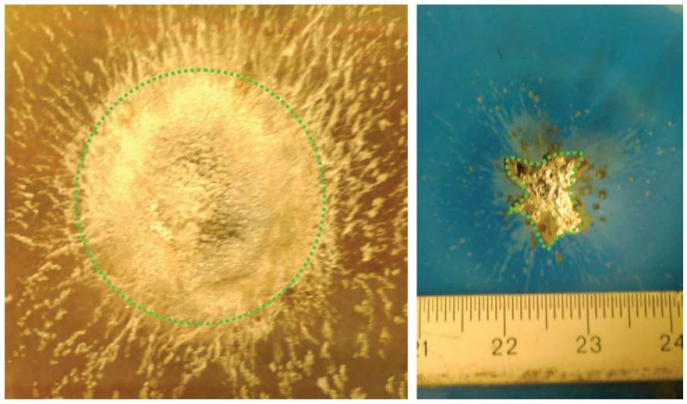

Figure 1.3: The damaged area in an aluminium plate (right) and a painted version of that aluminium plate (left) due to a 100kA current strike, Copyright © 2009, ONERA [1.14]

Using segmented strips is another approach, that consists of metal segments placed over a dielectric base, that can be installed at the locations where lightning is more likely to hit. Segmented strips provide a more focused guided path for the lightning strike current away from sensitive locations. Some of the different types of commercial segmented strips are shown in fig. 1.4. An aircraft radome is one of the locations that is susceptible to lightning and therefore requires the installation of segmented strips. Figure 1.5 shows a schematic of the places where segmented strips are installed on the aircraft radome.

Figure 1.4: Different commercial segmented strips for lightning protection , Copyright © 2013, Lightning Diversion Systems [1.15]

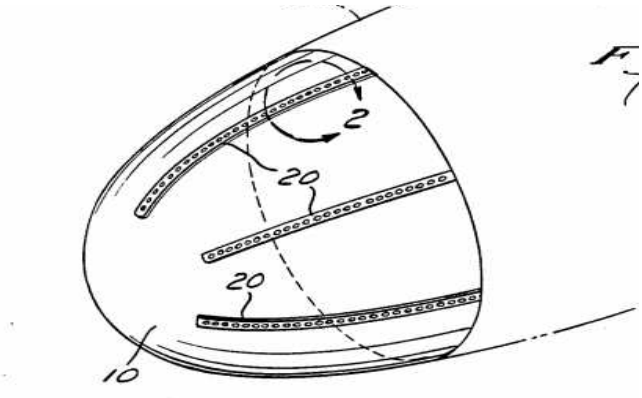

Figure 1.5: Schematic of segmented strips installed on an aircraft radome [1.16]

The lack of complete understanding of lightning limits the options for testing lightning protection to be mainly based on the expensive experimental approach. However, simulation tools are becoming more powerful and efficient due to the advances in distributed computer processes and are a cheaper option to help understanding this phenomenon.

Since the development of digital computers, numerical modelling has found its way to the heart of industry and manufacturing due its flexibility and the economic advantage that it adds to the process. Numerical modelling allows optimization and evaluations to take place in the design phase rather than after the product fabrication. This is done hand in hand with measurement in cases where numerical

analysis can't capture the entire physical phenomenon surrounding the application. Aircraft manufacturing is one of the industries in which models have to be built and pass a rigorous experimental testing process before commercial distribution due to complexity of the natural hazards its safety is threatened by, such as lightning and the extreme weather conditions during its operation. The numerical analysis for direct effects of lightning interaction with planes is attracting more attention in the past few years due to the economic value and in order to reduce the time and cost needed for testing and approving new models and designs [1.11].

Lightning phenomenon is a challenging multi-physics problem in which electromagnetic (EM)-propagation, chemical reactions, heat conduction, heat convection, mass transfer, and heat radiation interact simultaneously. Lightning starts when an intensive electric field is strong enough to cause atmosphere ionization around that field, changing the air into an ionized conductive plasma. Plasma is formed as branches of a conductive channels; hence lightning, exhibits distinctive glowing branches. The plasma channel formation in lightning is the same that which occurs in an arc discharge. Plasma channels typically have a very high temperature and therefore are used in metal welding and cutting in industry. This very high temperature influences the plasma material properties and thus adds non-linearity to the analysis, which makes the dependence on the EM analysis alone not sufficient to capture the phenomenon's physics when modelling.

The electro-thermal analysis of lightning is a challenging process as not only the time scale for each physical process (electromagnetic and thermal) is distinct but non-linear calculations add an extra layer of complexity. The EM propagation tends to occur on a time scale much shorter than the thermal reaction, hence adding a computational complexity to the problem.

Numerical methods are often used to model one side of the analysis i.e. either EM propagation or thermal diffusion. The numerical methods that model the EM

propagation are classified to either differential or integral methods based on which formulation of Maxwell's equations they solve. Differential methods uses the field differential equations to evaluate the field everywhere in the space surrounding the field source. These calculations require the entire problem domain to be discretised, and hence add a computational load on the numerical method. The fact that all the calculations are performed on each cell of the discretised space means that non-linearity and complex materials can be handled easily in differential methods. Integral methods on the other hand uses the source signal to evaluate the fields on the surfaces and the boundaries between objects and then use it to obtain the fields everywhere using integral equations. The fact that the entire domain is not discretised means that integral methods do not generally require a lot of computational power but modelling complex materials become a challenging task. In lightning where non-linearity is at the heart of the calculations differential methods become the obvious choice for modelling such phenomena.

Numerical methods are as well classified as either time- or frequency- domain methods. The time domain methods are suitable for problems where transient response is required whilst frequency domain methods capture the system response at a specific frequency. Modelling multi-physics problems is best undertaken using time domain methods to capture the evolution of the fields in time and the interaction with the system. Several numerical methods that are used widely in industry to model electromagnetic propagation are summarized in [1.17], such as asymptotic-expansion methods (AEM), the boundary element method (BEM), the finite difference time domain method (FDTD), the finite element analysis (FEM), the finite volume time domain method (FVTD), the method of moments in frequency and time domains (MOM) and transmission line method (TLM).

Among the existent numerical methods for EM propagation there are some differential numerical methods that can fit both EM propagation and thermal diffusion problems such as the finite difference time domain method (FDTD) [1.18], the finite

element method (FEM) [1.19] and the transmission line method (TLM) [1.20]. In this thesis the transmission line method (TLM) is used as a differential time domain method that is suitable for modelling all EM propagation, non-linear materials and thermal diffusion.

The TLM method is a time domain numerical method used to solve systems in which the physics of the problem are governed by second order linear partial differential equations (PDE) such as the wave equation that can describe EM propagation and thermal diffusion. The TLM method has been widely used for modelling in various microwave and electromagnetic compatibility (EMC) applications [1.21–1.23], and most recently has been applied to terahertz applications [1.24–1.27].

On their own, electromagnetic (EM) TLM and thermal TLM methods are well established methodologies for the modelling of electromagnetic wave propagation and thermal diffusion processes, respectively. The EM TLM method is an unconditionally stable time domain numerical method [1.28] that allows for great flexibility when modelling complex geometries and materials [1.29,1.30]. The EM TLM method uses the analogy between the EM field propagation and the voltage impulses travelling through a network of inter-connected transmission lines. Transmission lines are represented using equivalent RLC circuit equivalents and voltage propagation through the structure is solved in a time-stepping process of alternating scatter and connect operations [1.28]. The background material in EM TLM is assumed to be free space and different material properties such as conductivity, permittivity and permeability are incorporated using transmission line stubs [1.28]. Dispersive and frequency dependent properties may be conveniently implemented using a digital filter methodology [1.29,1.30].

The thermal TLM method uses the analogy between the heat equation and the EM wave equation to simulate the conductive heat diffusion through a network of lossy transmission lines whereby thermal properties such as the thermal conduc-

tivity and heat capacity of materials are mapped onto the equivalent resistances and impedances in the transmission line model [1.31]. The background material in the thermal model is chosen to be the material with the lowest time RC constant among the materials used in the model. Different materials are modelled using the link-stub technique [1.31,1.32]. The thermal TLM model has previously been used for heat flux modelling in several applications such as semiconductor devices [1.33], microwave heating process [1.34] and modelling thermal response in magneto-optic multi-layered media [1.35].

The implementation of a numerical model to couple the electro-thermal aspects of engineering problems and microwave heating was implemented before in the FEM and the FDTD method [1.36–1.38]. A coupling between FDTD and FEM was implemented for electro-thermal analysis in microwave heating as well [1.39,1.40] where FDTD was used to evaluate the EM aspects of the model and FEM was then applied to compute the thermal response based on the electrical power loss in the model. However, the majority of the research reported to date on the modelling of arc discharge and lightning has focused on either the electrical or thermal point of view or, in the case of industrial applications, on chemical processes and techniques to stabilize the arc discharge process [1.41,1.42]. There are few attempts done to model the lightning channel numerically such as [1.43] where a one-dimensional (1D) TLM model was proposed to model the lightning channel resistance and capacitance as a time varying quantities. The majority of the research in lightning protection and arc discharge is concerned with the direct effects of an intensive current (representing lightning) on materials and systems at the attachment points [1.44,1.45].

The gaps in the current research which this thesis is addressing, for protection against lightning strikes, are transient effects and the secondary breakdown caused on the systems due to a hit by a lightning strike. The work described in this thesis does not only combine the EM and thermal aspects of the phenomena but also includes the non-linear features of the phenomena to predict the location of the

secondary breakdown location using a fully coupled numerical model based on the TLM method. The work in this thesis demonstrates a fully coupled approach where EM properties in the model are modified according to the thermal profile. This full-coupling technique represents a more complex approach to the multi-physics modelling over most of the work in literature where the electro-thermal coupling is done only from the EM model (power loss) to the thermal model [1.44,1.45]. The coupled EM-thermal model is also validated and extended by modelling plasmonic heat sources.

1.2 Thesis organization

This section outlines the organization of the work presented in this thesis.

In chapter 2, the governing equation for EM propagation is introduced followed by an overview of the TLM method showing the analogy between EM propagation and circuit theory. The TLM model is presented for 1D and 2D cases followed by a section on modelling different materials for EM applications. The general 2D-TLM condensed node is then introduced as a method for modelling frequency dependent materials.

In chapter 3, the background to heat diffusion is introduced. An overview of the previous works related to modelling heat diffusion using the TLM method is given followed by heat conduction modelling using the 2D-TLM thermal model.

Chapter 4 overviews the condensed node TLM formulation for the modelling of EM frequency dependent behaviour of plasma. This is followed by the coupling algorithm between the EM-TLM and the thermal-TLM used in this work.

In chapter 5, the multi-physics algorithm developed in this work was applied first

to study a plasmonic nano-heat source and was validated against experimental and numerical results obtained from the literature. An investigation of efficient ways of coupling between EM-TLM and thermal-TLM is presented.

Chapter 6 outlines how the multi-physics algorithm is used to predict the shape and location of the plasma channel in arc discharge for a simplified 2D model of arc discharge in an air-gap. This is further extended to a button strip model that is used for lightning protection on airborne radomes.

Finally, chapter 7, draws together the main conclusion of the work presented in this thesis and presents a discussion on the limitation of the work and the challenges for future work.

References

[1.1] H.-C. Wu, "Relativistic-microwave theory of ball lightning," *Scientific Reports*, vol. 6, p. 28263, 2016.

[1.2] "IEEE Guide for Direct Lightning Stroke Shielding of Substations," *IEEE Std 998-1996*, no. Feb, pp. 1–176, 1996.

[1.3] J. Cen, P. Yuan, and S. Xue, "Observation of the optical and spectral characteristics of ball lightning," *Physical Review Letters*, vol. 112, no. 3, p. 035001, 2014.

[1.4] J. D. McDonald, *Electric Power Substations Engineering*, 3rd ed. New York: CRC press, 2012.

[1.5] N. Szedenik, "Rolling sphere method or theory?" *Journal of Electrostatics*, vol. 51-52, no. 1-4, pp. 345–350, 2001.

[1.6] C. B. Moore, W. Rison, J. Mathis, and G. Aulich, "Lightning rod improvement studies," *Journal of Applied Meteorology*, vol. 39, no. 5, pp. 593–609, 2000.

[1.7] J. V. Bladel, *Singular Electromagnetic Fields and Sources*. New York: Oxford Univeristy Press, 1991.

[1.8] M. S. Banjanin, M. S. Savić, and Z. M. Stojković, "Lightning protection of overhead transmission lines using external ground wires," *Electric Power Systems Research*, vol. 127, pp. 206–212, 2015.

[1.9] A. Piantini, "Lightning Protection of Overhead Power Distribution Lines," in *29 th International Conference on Lightning Protection*, 2008, pp. 1–29.

[1.10] "Civil Aeronautics Board, ICAO Accident Digest No.15 - Volume II, Circular 78-AN/66 (121-133)," Federal Aviation agency, Tech. Rep. 1, 1965. [Online]. Available: http://aviation-safety.net/database/record.php?id=19631208-0{&}lang=en

[1.11] F. A. Fisher and J. A. Plurner, *Lightning Protection of Aircraft*. Washington, D.C. USA: NASA reference publication 1008, 1977.

[1.12] P. K. Mallick, *Fiber-reinforced Composites: Materials, Manufacturing, and Design*. CRC press, 2007.

[1.13] P. Feraboli and M. Miller, "Damage resistance and tolerance of carbon/epoxy composite coupons subjected to simulated lightning strike," *Composites Part A: Applied Science and Manufacturing*, vol. 40, no. 6-7, pp. 954–967, jul 2009.

[1.14] B. Peyrou, A. Chazottes, P. Q. Elias, L. Chemartin, and P. Lalande, "Direct effects of lightning on aircraft structure : analysis of the thermal , electrical and mechanical constraints," *Journal Aerospace Lab*, no. 5, pp. 1–15, 2012.

[1.15] "Lightning Diversion Systems," 2016. [Online]. Available: http://lightningdiversion.com/home/diversion-strips/

[1.16] M. Amason, J. Schroeder, and E. Alsenz, "Lightning diversion strips for aircraft," Jan. 3 1989, uS Patent 4,796,153. [Online]. Available: https://www.google.com/patents/US4796153

[1.17] M. Niziolek, "Review of methods used for computational electromagnetics," in *2009 2nd International Students Conference on Electrodynamic and Mechatronics*. IEEE, 2009, pp. 15–16.

[1.18] J. B. Schneider, *Understanding the Finite-Difference Time-Domain Method*, 2015. [Online]. Available: www.eecs.wsu.edu/{~}schneidj/ufdtd/

[1.19] R. T. Fenner, *Finite Element mMethods for Engineers*, 2nd ed. London: Imperial College Press, 2013.

[1.20] A. Rabello, E. Silva, R. Saldanha, C. Vollaire, and A. Nicolas, "Adaptive time-stepping analysis of nonlinear microwave heating problems," *IEEE Transactions on Magnetics*, vol. 41, no. 5, pp. 1584–1587, 2005.

[1.21] T. Benson, D. Hill, M. Johnson, and A. Duffy, "Analysis of microwave resonators using transmission line modelling," *IEE Proceedings - Science, Measurement and Technology*, vol. 143, no. 6, pp. 362–368, 1996.

[1.22] C. Christopoulos, J. F. Dawson, L. Dawson, I. D. Flintoft, O. Hassan, A. C. Marvin, K. Morgan, P. Sewell, C. J. Smartt, and Z. Q. Xie, "Characterization and modelling of electromagnetic interactions in aircraft," *Proceedings of the Institution of Mechanical Engineers, Part G: Journal of Aerospace Engineering*, vol. 224, no. 4, pp. 449–458, 2010.

[1.23] V. Janyani, "Modelling of dispersive and nonlinear materials for optoelectron-

ics using TLM," PhD thesis, University of Nottingham, 2005.

[1.24] O. S. Ahmed, M. A. Swillam, M. H. Bakr, and X. Li, "Modeling and design of nano-plasmonic structures using transmission line modeling," *Optics Express*, vol. 18, no. 21, p. 21784, 2010.

[1.25] V. Janyani, J. Paul, A. Vukovic, T. Benson, and P. Sewell, "TLM modelling of nonlinear optical effects in fibre Bragg gratings," *IEE Proceedings - Optoelectronics*, vol. 151, no. 4, p. 185, 2004.

[1.26] S. Phang, A. Vukovic, H. Susanto, T. M. Benson, and P. Sewell, "Ultrafast optical switching using paritytime symmetric Bragg gratings," *Journal of the Optical Society of America B*, vol. 30, no. 11, p. 2984, 2013.

[1.27] X. Meng, P. Sewell, A. Vukovic, H. G. Dantanarayana, and T. M. Benson, "Efficient broadband simulations for thin optical structures," *Optical and Quantum Electronics*, vol. 45, no. 4, pp. 343–348, 2013.

[1.28] C. Christopoulos, *The Transmission-Line Modeling Method TLM.* Piscataway, NJ: IEEE Press, 1995.

[1.29] J. Paul, C. Christopoulos, and D. W. P. Thomas, "Generalized material models in TLM Part I : Materials with frequency-dependent properties," vol. 47, no. 10, pp. 1528–1534, 1999.

[1.30] J. Paul, "Modelling of general electromagentic material properties in TLM," Ph.D. dissertation, Univeristy of Nottingham, 1998.

[1.31] D. DeCogan, *Transmission Line Matrix (TLM) techniques for Diffusion Applications.* Amesterdam, The Netherlands: Gordon and Breach Science Publishers, 1998.

[1.32] H. C. Patel, "Non-linear 3D modelling heat of flow in magneto-optic multi-layered media," PhD thesis, University of Keele.

[1.33] R. Hocine, A. Boudghene Stambouli, and A. Saidane, "A three-dimensional TLM simulation method for thermal effect in high power insulated gate bipolar transistors," *Microelectronic Engineering*, vol. 65, no. 3, pp. 293–306, 2003.

[1.34] C. Flockhart, "The simulation of coupled electromagnetic and thermal problems in microwave heating," in *Second International Conference on Computation in Electromagnetics*, vol. 1994, no. 4. London: IEE, 1994, pp. 267–270.

[1.35] E. W. Williams, H. C. Patel, D. DeCogan, and S. H. Pulko, "TLM modelling of thermal processes in magneto-optic multi-layered media," *Journal of Physics D: Applied Physics*, vol. 29, no. 5, pp. 1124–1132, 1996.

[1.36] H. Zhang and A. K. Datta, "Coupled electromagnetic and thermal modelling of microwave oven heating of foods," *Journal of Microwave Power and Electromagnetic Energy*, vol. 35, no. 2, pp. 71–85, 2000.

[1.37] Lizhuang Ma, D.-L. Paul, N. Pothecary, C. Railton, J. Bows, L. Barratt, J. Mullin, and D. Simons, "Experimental validation of a combined electromagnetic and thermal FDTD model of a microwave heating process," *IEEE Transactions on Microwave Theory and Techniques*, vol. 43, no. 11, pp. 2565–2572, 1995.

[1.38] P. Ratanadecho, K. Aoki, and M. Akahori, "A numerical and experimental investigation of the modeling of microwave heating for liquid layers using a rectangular wave guide (effects of natural convection and dielectric properties)," *Applied Mathematical Modelling*, vol. 26, no. 3, pp. 449–472, 2002.

[1.39] K. Knoerzer, M. Regier, and H. Schubert, "A computational model for calculating temperature distributions in microwave food applications," *Innovative*

Food Science & Emerging Technologies, vol. 9, no. 3, pp. 374–384, 2008.

[1.40] P. Kopyt and M. Celuch, "Towards a multiphysics simulation system for microwave power phenomena," in *2005 Asia-Pacific Microwave Conference Proceedings*, vol. 5. IEEE, 2005, pp. 1–4.

[1.41] M. S. Benilov, "Understanding and modelling plasmaelectrode interaction in high-pressure arc discharges: A review," *Journal of Physics D: Applied Physics*, vol. 41, no. 14, p. 144001, 2008.

[1.42] M. Tanaka and J. J. Lowke, "Predictions of weld pool profiles using plasma physics," *Journal of Physics D: Applied Physics*, vol. 40, no. 1, pp. R1–R23, 2007.

[1.43] M. Da Frota Mattos and C. Christopoulos, "A nonlinear transmission line model of the lightning return stroke," *IEEE Transactions on Electromagnetic Compatibility*, vol. 30, no. 3, pp. 401–406, 1988.

[1.44] H. Tsubata, T. Nishi, H. Fujisawa, Y. Baba, and M. Nakagawa, "FDTD simulation of lightning current in a multi-layered CFRP material," in *International Conference on Lightning & Static Electricity (ICOLSE 2015)*. Institution of Engineering and Technology, 2015, pp. 16 (4 .)–16 (4 .).

[1.45] R. Neufeld, "Lightning direct effects on anisotropic materials from electrothermal simulation," in *International Conference on Lightning & Static Electricity (ICOLSE 2015)*, no. 2. Institution of Engineering and Technology, 2015, pp. 7 (5 .)–7 (5 .).

2

Electromagnetism and TLM

This chapter outlines the foundation and the implementation of the transmission line modelling (TLM) method. The TLM method introduced in this chapter is used throughout this thesis to model the electromagnetic (EM) aspects of electro-thermal problems presented in the thesis. In this chapter the theory of the TLM method is introduced using an analogy between the EM propagation and the circuit representation of transmission lines. The implementation of the TLM method is presented for 1D and 2D cases [2.1,2.2]. Modelling of material properties using a stub technique [2.1] is also discussed. Finally a 2D-TLM condensed node [2.2] is outlined for modelling non-linear materials in TLM.

* * *

2.1 Electromagnetic field analogy

In the early nineteenth century James Maxwell combined the laws of electricity and magnetism utilizing earlier work produced by fellow researchers and scientists in an attempt to describe the governing equations for electromechanics physics [2.3] which

were later to be known as Maxwell's equations. These laws have been rewritten [2.4,2.5] by Oliver Heaviside [2.6,2.7] and are known today as Maxwell's equations in differential form and are given as:

$$\nabla \times \mathbf{E} = -\frac{\partial \mathbf{B}}{\partial t} = \mathbf{J_m} - \mu \frac{\partial \mathbf{H}}{\partial t}, \tag{2.1a}$$

$$\nabla \times \mathbf{H} = -\frac{\partial \mathbf{D}}{\partial t} = \mathbf{J_e} + \varepsilon \frac{\partial \mathbf{E}}{\partial t}, \tag{2.1b}$$

$$\nabla . \varepsilon \mathbf{E} = \nabla . \mathbf{D} = \rho_v, \tag{2.1c}$$

$$\nabla . \mu \mathbf{H} = \nabla . \mathbf{B} = 0 \tag{2.1d}$$

$\mathbf{E}$, $\mathbf{H}$, $\mathbf{B}$, $\mathbf{D}$, $\mathbf{J_m}$ and $\mathbf{J_e}$ are real functions in time and space, e.g $\mathbf{E}(x, y, z; t)$, representing electric field vector in[V/m], magnetic field vector in [A/m], magnetic flux density vector in [Wb/m^2], electric flux density vector [C/m^2], magnetic voltage density vector in [V/m^2] and electric current density vector in [A/m^2] respectively. ε is electric permittivity in [F/m], μ is magnetic permeability in [H/m] and ρ_v is charge density per unit volume in [C/m^3].

The electric current density is directly proportional to the electric field and is evaluated using Ohm's law $\mathbf{J_e} = \sigma_e \mathbf{E}$ [2.7] where σ_e is electric conductivity in [S/m]. Similarly, magnetic voltage density is directly proportional to the magnetic field and is evaluated using [2.7] $\mathbf{J_m} = \sigma_m \mathbf{H}$ where σ_m is magnetic resistivity in [Ω/m]. In this section for simplicity all the derivations are obtained for non-magnetic materials i.e. ($\sigma_m = 0$) and therefore the magnetic voltage density is omitted from the future derivations in this section.

A complete field representation can be obtained by solving Maxwell's equations at any point in the space. Expanding the vector operations for the electric and magnetic fields in eqs. (2.1a) and (2.1b) in Cartesian coordinates leads to the following set of

equations:

$$\frac{\partial E_z}{\partial y} - \frac{\partial E_y}{\partial z} = -\mu \frac{\partial H_x}{\partial t}, \tag{2.2a}$$
$$\frac{\partial E_x}{\partial z} - \frac{\partial E_z}{\partial x} = -\mu \frac{\partial H_y}{\partial t}, \tag{2.2b}$$
$$\frac{\partial E_y}{\partial x} - \frac{\partial E_x}{\partial y} = -\mu \frac{\partial H_z}{\partial t}, \tag{2.2c}$$
$$\frac{\partial H_z}{\partial y} - \frac{\partial H_y}{\partial z} = J_{e_x} + \varepsilon \frac{\partial E_x}{\partial t}, \tag{2.2d}$$
$$\frac{\partial H_x}{\partial z} - \frac{\partial H_z}{\partial x} = J_{e_y} + \varepsilon \frac{\partial E_y}{\partial t}, \tag{2.2e}$$
$$\frac{\partial H_y}{\partial x} - \frac{\partial H_x}{\partial y} = J_{e_z} + \varepsilon \frac{\partial E_z}{\partial t}. \tag{2.2f}$$

In the one dimensional case the field is considered to be varying only along the propagation direction, which may be conveniently considered to be the z-direction and hence $\frac{\partial}{\partial x} = 0$ and $\frac{\partial}{\partial y} = 0$, leading to a reduced form of eqs. (2.2a) to (2.2f) as:

$$-\frac{\partial E_y}{\partial z} = -\mu \frac{\partial H_x}{\partial t}, \tag{2.3a}$$
$$\frac{\partial H_x}{\partial z} = J_{e_y} + \varepsilon \frac{\partial Ey}{\partial t}, \tag{2.3b}$$
$$\frac{\partial E_x}{\partial z} = -\mu \frac{\partial H_y}{\partial t}, \tag{2.3c}$$
$$-\frac{\partial H_y}{\partial z} = J_{e_x} + \varepsilon \frac{\partial E_x}{\partial t}. \tag{2.3d}$$

Replacing the electric field components in eqs. (2.3a) to (2.3d) with the corresponding current density component using Ohm's law, eqs. (2.3a) to (2.3d) become:

$$-\frac{\partial J_y}{\partial z} = -\mu\sigma_e \frac{\partial H_x}{\partial t}, \tag{2.4a}$$
$$\frac{\partial H_x}{\partial z} = J_{e_y} + \frac{\varepsilon}{\sigma_e} \frac{\partial J_y}{\partial t}, \tag{2.4b}$$
$$\frac{\partial J_x}{\partial z} = -\mu\sigma_e \frac{\partial H_y}{\partial t}, \tag{2.4c}$$
$$-\frac{\partial H_y}{\partial z} = J_{e_x} + \frac{\varepsilon}{\sigma_e} \frac{\partial J_x}{\partial t}. \tag{2.4d}$$

Combining eqs. (2.3a) to (2.3b) or eqs. (2.3c) to (2.3d) together, the current density in a lossy medium can be obtained from eq. (2.4) as:

$$\frac{\partial^2 J_{e_{x,y}}}{\partial z^2} = \mu\varepsilon \frac{\partial^2 J_{e_{x,y}}}{\partial t^2} + \mu\sigma_e \frac{\partial J_{e_{x,y}}}{\partial t}. \tag{2.5}$$

It can be shown [2.1] that the electric field components E_x and E_y can be evaluated in the same way using

$$\frac{\partial^2 E_{x,y}}{\partial z^2} = \mu\varepsilon\frac{\partial^2 E_{x,y}}{\partial t^2} + \mu\sigma_e\frac{\partial E_{x,y}}{\partial t}. \tag{2.6}$$

The first term on the right hand side of eq. (2.5) describes a wave-like (propagation) behaviour while the second term describes diffusion-like behaviour [2.8]. Equation (2.5) can be further reduced if the material is a poor conductor, i.e. ($\sigma_e \approx 0$) and at high frequency, i.e

$$\frac{\partial^2 J}{\partial z^2} = \mu\varepsilon\frac{\partial^2 J}{\partial t^2}. \tag{2.7}$$

which is a general form of the wave equation [2.8,2.9]. On the other hand if the material has a high conductivity and the wave form is at low frequency, so that $\mu\varepsilon\frac{\partial^2 J_{ex,y}}{\partial t^2} \ll \mu\sigma_e\frac{\partial J_{ex,y}}{\partial t}$, eq. (2.6) reduces to,

$$\frac{\partial^2 E_{x,y}}{\partial z^2} = \mu\sigma_e\frac{\partial E_{x,y}}{\partial t}, \tag{2.8}$$

which represent a diffusion-like behaviour and is more suitable for describing low frequency problems or other physical systems such as heat conduction.

This chapter is focused on modelling EM phenomena described by eq. (2.7). This is done here using the analogy between the wave equation eq. (2.7) and circuit theory which, for the one dimensional (1D) case is represented by a short section of transmission line as shown in Figure 2.1, where L, R, C and G are the series inductance in $[H]$, resistance in $[\Omega]$, shunt capacitance in $[F]$ and admittance in $[S]$ respectively.

Applying Kirchhoff's voltage and current laws to the equivalent circuit of a transmission line of length of Δz as shown in Figure 2.1 results in :

$$\Delta z\frac{\partial v}{\partial z} = -L\frac{\partial i}{\partial t} - iR, \tag{2.9}$$

$$\Delta z\frac{\partial i}{\partial z} = -C\frac{\partial v}{\partial t} - Gv, \tag{2.10}$$

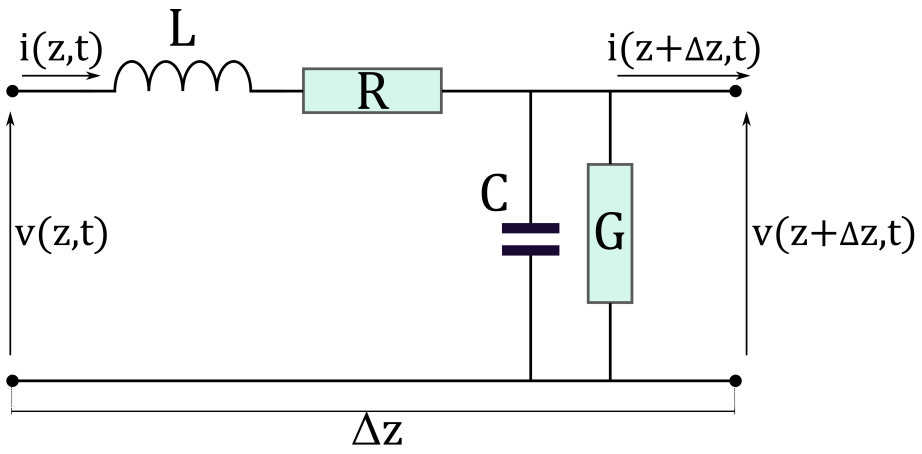

Figure 2.1: The general circuit representation for a lossy transmission line section

where $v(z,t)$ and $i(z,t)$ are the voltage and current as a function of time(t) and space (z-direction). It can be shown that combining eq. (2.9) and eq. (2.10) leads to a pair of equations for the voltage and current of the transmission line circuit:

$$\frac{\partial^2 v}{\partial z^2} = \frac{GR}{(\Delta z)^2} v + \frac{1}{(\Delta z)^2}(GL + RC)\frac{\partial v}{\partial t} + \frac{LC}{(\Delta z)^2}\frac{\partial^2 v}{\partial t^2}, \tag{2.11}$$

$$\frac{\partial^2 i}{\partial z^2} = \frac{GR}{(\Delta z)^2} i + \frac{1}{(\Delta z)^2}(GL + RC)\frac{\partial i}{\partial t} + \frac{LC}{(\Delta z)^2}\frac{\partial^2 i}{\partial t^2}. \tag{2.12}$$

If the assumption G=0 is made, eq. (2.11) becomes

$$\frac{\partial^2 v}{\partial z^2} = \frac{RC}{(\Delta z)^2}\frac{\partial v}{\partial t} + \frac{LC}{(\Delta z)^2}\frac{\partial^2 v}{\partial t^2}, \tag{2.13}$$

Using the isomorphism between eq. (2.13) and eq. (2.6), the electromagnetic field can be represented using voltage and current in the equivalent circuits using the following equivalences,

$$E \leftrightarrow \tfrac{v}{\Delta z}, \qquad H \leftrightarrow \tfrac{i}{\Delta z}, \qquad \varepsilon \leftrightarrow \tfrac{C}{\Delta z}, \qquad \mu \leftrightarrow \tfrac{L}{\Delta z}, \qquad \sigma_e \leftrightarrow \tfrac{G}{\Delta z}.$$

This analogy shows that using the correct parameter mapping, and minimizing the discretization error by following the rule of thumb $\Delta z \ll \lambda/10$ where λ is the wavelength of the highest operating frequency in the model [2.1], the solution of the 1D electromagnetic wave propagation can be obtained by solving a simple circuit of

transmission lines. This is the basis of the TLM method. A propagating signal in a section of transmission line of a length Δz requires a time Δt to travel through the transmission line section with the propagation velocity u. It can shown using eq. (2.6) that the propagation speed of a travelling wave is evaluated using,

$$u = \frac{1}{\sqrt{\varepsilon\mu}}. \tag{2.14}$$

Using the analogy derived between electromagnetic propagation and circuit theory, the velocity in a transmission line section will reduce eq. (2.14) to, [2.1]

$$u = \frac{1}{\sqrt{\frac{C}{\Delta z}\frac{L}{\Delta z}}}. \tag{2.15}$$

The time step necessary for the wave to travel across the node is linked to material parameters and length as,

$$\Delta t = \frac{\Delta z}{u} = \Delta z \times \sqrt{\frac{L}{\Delta z}\frac{C}{\Delta z}} = \sqrt{LC}. \tag{2.16}$$

Solving transmission line circuits as shown fig. 2.1 requires the knowledge of the characteristic impedance, which is calculated using [2.1],

$$Z_{TL} = \sqrt{\frac{L}{C}}, \tag{2.17}$$

where Z_{TL} is the characteristic impedance of transmission line and L and C are the impedance and capacitance respectively.

2.2 One-dimensional TLM method

The TLM method is a time domain method in which the field is calculated in a time stepping fashion during the whole period of the simulated time. It discretisizes the problem geometry into small sections of interconnected transmission lines which are then represented by RLC circuits. The TLM method algorithm can be broken down

into three main processes, namely initialization, connection and scattering, of which connection and scattering are repeated for every time step during the simulation until field convergence is achieved. The first process is the initialization, in which the mesh size, time step, material allocation and geometry parameters are initialized. The second process is the scattering calculations, in which the reflected voltages for each node are calculated based on the incident and nodal voltages. The scattering process for each node is independent of its adjacent nodes. In the connection process the reflected voltages at each time step become incident at their neighbour nodes. TLM is an algorithm of a causal system, in which nodal calculations are dependent on the voltages from previous time steps, and it is therefore an unconditionally stable numerical technique [2.1].

Figure 2.2 is an example of an intersection of two sections of a lossless transmission line at node n, where ${}_kV_n$ is the total voltage at node n during the time step k. ${}_kVR_n^i$ and ${}_kVL_n^i$ are the incident voltages at node n during the time step k from the right(R) and the left(L) respectively. Reflected voltages are presented in the same manner as ${}_kVR_n^r$ and ${}_kVL_n^r$. Neighbouring nodes on the left and right have nodal voltages ${}_kV_{n-1}$ and ${}_kV_{n+1}$ respectively.

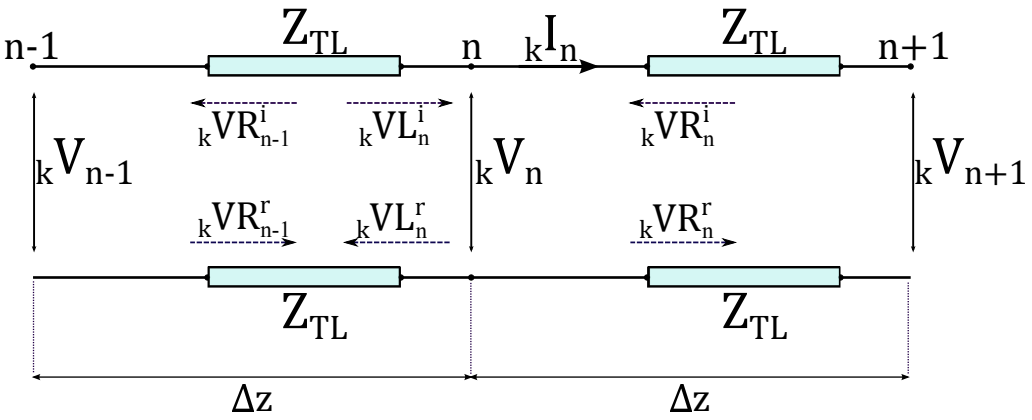

Figure 2.2: The general circuit representation for a transmission line section

The nodal voltage calculation at node n during the time step k is calculated based on

the local incident voltages from both directions to the left and to the right as,

$$ {}_kV_n =_k V_nL^i +_k V_nR^i. \tag{2.18} $$

The reflected voltages to the left and to the right for node n during time step k are evaluated as,

$$ {}_kV_nL^r =_k V_n -_k V_nL^i. \tag{2.19} $$

$$ {}_kV_nR^r =_k V_n -_k V_nR^i \tag{2.20} $$

The connection process interchanges the calculated reflected voltages between adjacent nodes, which will become the incident voltages in the next time step $k+1$, i.e.,

$$ {}_{k+1}V_nL^i =_k V_{n-1}L^r. \tag{2.21} $$

$$ {}_{k+1}V_nR^i =_k V_{n+1}R^r \tag{2.22} $$

Repeating the previous steps, and considering suitable boundary conditions for each modelling case, represents the main algorithm of 1D-TLM method. The processes described in this section may be extended to include the 2D and 3D cases and the equivalent circuit equations to be compared with the corresponding field equation. The 2D case is considered in Section 2.3

2.3 Two-dimensional TLM method

In engineering systems many 3D problems can be approximated to an equivalent 2D one and solved with a good degree of accuracy. A typical case for this approximation is modelling propagation in waveguides and resonators. The advantages of the 2D TLM method are that it is much simpler than the 3D case and less computationally expensive. The 2D method can accommodate two types of EM propagation, Transverse Electric (TE) and Transverse magnetic (TM). TE propagation allows for only one magnetic field component along the longitudinal direction H_z, and transverse electric fields, E_x and E_y, which are modelled by a 2D-TLM series node. TM

propagation on the other hand allows for an only electric field component in the longitudinal direction E_z, and transverse magnatic fields components H_x and H_y which are modelled by a 2D-TLM shunt node.

Figure 2.3 shows a schematic of the two different configurations of the 2D-TLM node; the series TLM node is shown in Figure 2.3a and the shunt TLM node is shown in Figure 2.3b. Both series and shunt nodes consist of four sections of transmission line, as shown in Figure 2.3, with the main difference being in the way they intersect. In the next section the TLM-TE formulation is presented as it is the node configuration used for modelling the EM aspects of the electro-thermal problems described in this thesis.

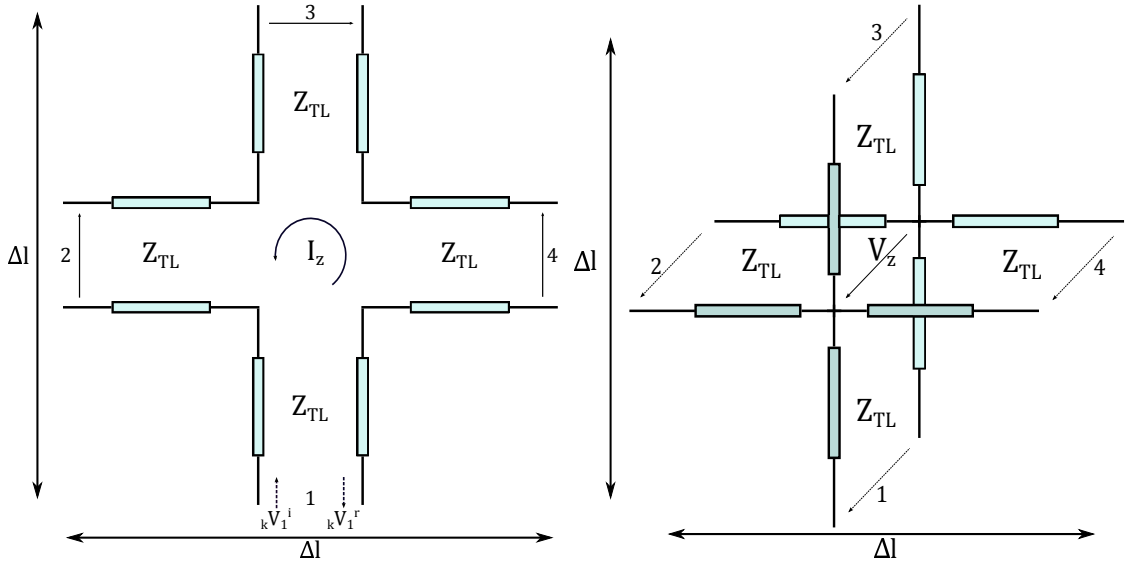

(a) Series TLM node (TE) **(b)** Shunt TLM node (TM)

Figure 2.3: 2D-TLM node schematic for TE and TM cases,(a) Series Node "TE" and (b) Shunt node "TM"

2.3.1 TLM Series node

In 2D-TLM the problem domain is described by a finite number of cells in the x and y directions considered here of equal length ($\Delta x = \Delta y = \Delta l$). The node parameters

such as characteristic impedance and time step have to be arranged in a way to suit the circuit configuration in 2D. The series node configuration involves an over estimation of the inductance by a factor of 2. This is due to the fact that loop current passes through the same inductance twice [2.1]. The characteristic impedance in 2D is evaluated using,

$$Z_{TL} = \sqrt{\frac{L}{2C}}\,, \tag{2.23}$$

in which inductance is halved to compensate for the overestimation. Similarly the time step in a 2D-series node is scaled to,

$$\Delta t = \frac{\Delta l}{(\sqrt{2}u)}, \tag{2.24}$$

The voltage and current calculations at any given node at location ($i\Delta x$,$j\Delta y$) during the time step k are calculated using:

$$\begin{aligned} {}_kI_z(i,j) &= \frac{{}_kV_1^i(i,j) - {}_kV_2^i(i,j) - {}_kV_3^i(i,j) + {}_kV_4^i(i,j)}{2Z_{TL}}, \\ {}_kV_x(i,j) &= \frac{{}_kV_1^i(i,j) + {}_kV_3^i(i,j)}{2}, \\ {}_kV_y(i,j) &= \frac{{}_kV_2^i(i,j) + {}_kV_4^i(i,j)}{2}, \end{aligned} \tag{2.25}$$

where ${}_kI_z$ is the current in the z direction and ${}_kV_x$ *and* ${}_kV_y$ are the voltages in x and y directions respectively. The voltages ${}_kV_1^i(n_x,n_y)$, ${}_kV_2^i(n_x,n_y)$, ${}_kV_3^i(n_x,n_y)$ *and* ${}_kV_4^i(n_x,n_y)$ represent the voltages incident from the different ports of the node indicated by (1,2,3 and 4) in fig. 2.3.

According to the analogy between circuit theory and wave parameters described in section 2.1 and the assumption of equal dimensions of the nodes, field parameters can be obtained as:

$$H_z = \frac{I_z}{\Delta l}, \qquad E_x = -\frac{V_x}{\Delta l} \qquad \text{and} \qquad E_y = -\frac{V_y}{\Delta l} \tag{2.26}$$

The scattered voltage from each node port is calculated from the general expression,

$${}_kV^r = {}_kV - {}_kV^i, \tag{2.27}$$

Applying eq. (2.25) to eq. (2.27) using Port 1 as an example, the reflected voltage is obtained as,

$$\begin{aligned} {}_kV^r &= 2{}_kV_1^i - IZ_{TL} - {}_kV_1^i \\ &= 0.5({}_kV_1^i + {}_kV_2^i + {}_kV_3^i - {}_kV_4^i). \end{aligned} \tag{2.28}$$

The reflected voltages for the other ports can be obtained similarly. Using all the reflected voltages the scattering process can be expressed in matrix form as,

$$\begin{bmatrix} {}_kV_1^r \\ {}_kV_2^r \\ {}_kV_3^r \\ {}_kV_4^r \end{bmatrix} = 0.5 \begin{bmatrix} 1 & 1 & 1 & -1 \\ 1 & 1 & -1 & 1 \\ 1 & -1 & 1 & 1 \\ -1 & 1 & 1 & 1 \end{bmatrix} \begin{bmatrix} {}_kV_1^i \\ {}_kV_2^i \\ {}_kV_3^i \\ {}_kV_4^i \end{bmatrix}, \tag{2.29}$$

where

$$\begin{aligned} {}_kV^r &= \begin{bmatrix} {}_kV_1^r & {}_kV_2^r & {}_kV_3^r & {}_kV_4^r \end{bmatrix}^T, \\ {}_kV^i &= \begin{bmatrix} {}_kV_1^i & {}_kV_2^i & {}_kV_3^i & {}_kV_4^i \end{bmatrix}^T, \\ {}_kV^r &= \mathbf{S}\ {}_kV^i, \end{aligned}$$

and $\mathbf{S}$ is the scattering matrix for the series 2D-TLM node shown in fig. 2.3a.

The connection process evaluates the incident voltages for the next time step $(k+1)$ based on the reflected voltages from the adjacent nodes at the current time step (k), and can be expressed as,

$$\begin{aligned} {}_{k+1}V_1^i(i,j) &=_k V_3^r\big(i,(j-1)\big) \\ {}_{k+1}V_2^i(i,j) &=_k V_4^r\big((i-1),j\big) \\ {}_{k+1}V_3^i(i,j) &=_k V_1^r\big(i,(j+1)\big) \\ {}_{k+1}V_4^i(i,j) &=_k V_2^r\big((i+1),j\big) \end{aligned} \tag{2.30}$$

2.4 Modelling different materials using a stub technique

The propagation speed of an electromagnetic wave is dependent on the medium in which the wave travels and varies with different material parameters. For problems that contain different material parameters it is challenging to keep the mesh size of the TLM method fixed without having different time steps for different materials in the model. On the other hand keeping the time step fixed in the presence of different materials parameters enforces the mesh size to be changed. Both cases have undesired effects as the synchronization of incident and reflected voltages and ports' direct connection will not be maintained. The stub technique allows the time step and mesh size to remain the same for different materials that are being modelled. The idea behind the stub technique is to use the same characteristic impedance throughout the model that acts as a background material [2.1]. The capacitance and inductance differences between modelled and background material will be added in the forms of capacitive or inductive stubs which will mimic the slowing down of propagation due to passing through different materials.

Practical implementations of an electromagnetic TLM (EM-TLM) method use free space parameters for modelling the background material. The reason behind this choice is that electromagnetic waves are fastest in free space. Using free space as the background material guarantees having a positive impedance difference between background and modelled materials and hence guarantees having a positive stub impedance which maintains the algorithm stability and is explained later in this section. This section shows the implementation of the stub technique in 1D-TLM using the example of a capacitive stub. Using free space as the background material leads to having a speed of propagation and characteristic impedance of the

transmission line as,

$$u = c = \frac{1}{\sqrt{\varepsilon_o \mu_o}} \tag{2.31}$$

$$Z_{TL} = Z_o = \sqrt{\frac{\mu_o}{\varepsilon_o}} \tag{2.32}$$

respectively, where ε_o, μ_0, Z_o, c and their units are described in Table 2.1.

Table 2.1: Symbols and units

Symbol	Unit	Name
ε_o	F/m	Electric permittivity of free Space
μ_o	H/m	Magnetic permeability of free space
Z_o	Ω	Impedance of free space
c	m/s	Speed of light in free space
ε_r	——	Electric relative permittivity
μ_r	——	Magnetic relative permeability
χ_e	——	Electric susceptibility

Figure 2.4 shows the 1D-TLM capacitive stub which consists of a section of open circuited transmission line connected at the node centre n. A capacitive stub is necessary when modelling a material with a higher permittivity than that of free space. The material's permittivity (ε) is linked to the permittivity of free space (ε_o) as,

$$\varepsilon = \varepsilon_o \varepsilon_r = \varepsilon_o(1 + \chi_e) \tag{2.33}$$

where the dimensionless quantities ε_r and χ_e are described in Table 2.1.

The signal round trip time in the stub has to be equal to the node time step Δt in order to maintain synchronization within the nodal calculations. This means that the signal spends only half of the time step to reach the other end of the capacitive stub which has a transmission line characteristic impedance Z_c. It can be shown

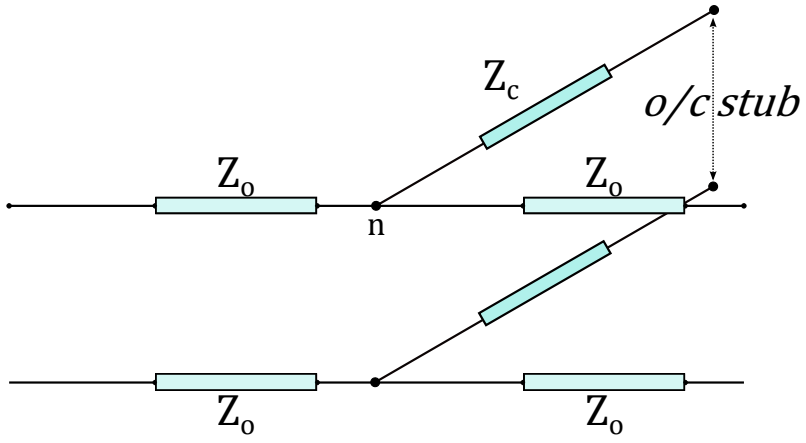

Figure 2.4: The 1D-TLM transmission line with added capacitive stub

from eqs. (2.16) and (2.17) that the capacitance and inductance of the transmission line are related to the time step as [2.1],

$$C = \frac{\Delta t}{Z_{TL}}, \qquad L = \Delta t Z_{TL}, \tag{2.34}$$

and therefore using the half time step the stub capacitance can be related to stub characteristic impedance through

$$Z_c = \frac{\Delta t/2}{C_s}, \tag{2.35}$$

where C_s is the stub capacitance and is related to the modelled material's total capacitance C_t using eq. (2.36)

$$\begin{aligned} C_t &= \varepsilon \Delta l = \varepsilon_o \varepsilon_r \Delta l \\ &= \varepsilon_0 \Delta l + \varepsilon_o(\varepsilon_r - 1)\Delta l \\ &= \varepsilon_0 \Delta l + \varepsilon_o \chi_e \Delta l \\ &= C_o + C_s \\ &= C_o + C_o \chi_e, \end{aligned} \tag{2.36}$$

where C_o is the free space background capacitance.

It can be shown [2.1] using eqs. (2.34) to (2.36) that the stub impedance can be represented as,

$$Z_c = \frac{\Delta t/2}{\frac{\Delta t}{Z_o}\chi_e} = Z_o \frac{1}{2\chi_e} \tag{2.37}$$

Solving the nodal equation is done by obtaining the Thevenin equivalents for the transmission line sections [2.1]. Figure 2.5 shows a section of transmission line and its equivalent Thevenin circuit. The transmission line section shown in fig. 2.5.a is terminated with an open circuit. The travelling pulse V^i is associated with a current pulse equal to $I = \frac{V^i}{Z_o}$ [2.1] but, as it is terminated with an open circuit, a reflected negative current pulse is generated so that the total current is $I = 0$. The reflected pulse increases the voltage pulse on the transmission line to $2V^i$ for a finite transient time equal to $\Delta t = \frac{\Delta x}{c}$. This transmission line section can be represented by a voltage source equal to twice of the incident pulse connected in series with the transmission line impedance as shown in fig. 2.5.b.

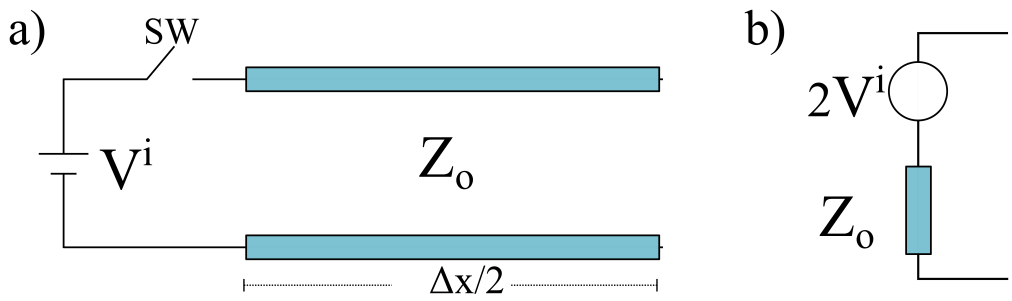

Figure 2.5: (a) A section of transmission line with open circuit termination and (b) Its Thevenin equivalent as a voltage source connected in series with the Transmission Line impedance.

Figure 2.6 shows the Thevenin equivalent circuit for 1D-TLM node that has a stub connected at the node centre. Hence, it can be shown [2.1]that the nodal voltage at the time step k for a 1D node is modified in the presence of a capacitive stub to

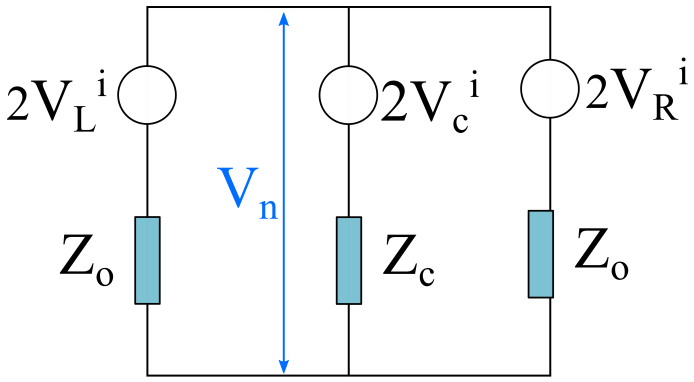

Figure 2.6: 1D-TLM node with a stub connected at the node centre.

be,

$$
\begin{aligned}
{}_kV_n &= \frac{\left(\frac{2_kVL_n^i}{Z_o}\right) + \left(\frac{2_kVR_n^i}{Z_o}\right) + \left(\frac{2_kVC_n^i}{Z_c}\right)}{\frac{2}{Z_o} + \frac{1}{Z_c}} \\
&= \frac{{}_kVL_n^i + {}_kVR_n^i + 2_kVC_n^i \cdot \chi_e}{1 + \chi_e}
\end{aligned}
\tag{2.38}
$$

where the ${}_kVC_n^i$ represents the incident voltage from the capacitive stub during time step k at the node n. The reflected voltage in the stub is added to the calculations as,

$$
{}_kVC_n^r = {}_k\,V_n - {}_k\,VC_n^i, \tag{2.39}
$$

where ${}_kVC_n^r$ is the reflected voltage of the capacitive stub. In the connection process the new incident voltage on the stub is obtained as,

$$
{}_{k+1}VC_n^i = {}_k\,VC_n^r. \tag{2.40}
$$

In a similar way the stub technique can be implemented for material with higher magnetic permeability as an inductive stub [2.1]. This stub technique can be implemented for 2D and 3D cases as well.

2.5 TLM Condensed Node

An alternative TLM formulation using the bilinear $Z-$transform and digital filters was introduced by Paul as the condensed node in [2.2,2.10–2.12]. This formulation

allows for more flexibility with non-linearity and materials with complex material parameters. In the next subsection this method is presented leading to a description of a 2D-TLM series condensed node.

2.5.1 Formulation

The curl Maxwell equation from eqs. (2.1a) and (2.1b) represented the time domain solution of the EM field. Equation (2.41) present the corresponding frequency domain soulition of the EM field in the matrix form [2.2,2.10–2.12],

$$\begin{bmatrix} \nabla \times \overline{\mathcal{H}} \\ -\nabla \times \overline{\mathcal{E}} \end{bmatrix} = \begin{bmatrix} \overline{\mathcal{J}}_e \\ \overline{\mathcal{J}}_m \end{bmatrix} + \frac{\partial}{\partial t} \begin{bmatrix} \overline{\mathcal{D}} \\ \overline{\mathcal{B}} \end{bmatrix}. \tag{2.41}$$

where $\overline{\mathcal{H}}$, $\overline{\mathcal{E}}$, $\overline{\mathcal{D}}$, $\overline{\mathcal{B}}$, $\overline{\mathcal{J}}_e$ and $\overline{\mathcal{J}}_m$ are real functions in frequency and space, e.g $\overline{\mathcal{H}}(x, y, z; \omega(\text{natural frequency rad/s}))$, representing magnetic field vector, electric field vector, electric flux density, magnetic flux density, electric current density and magnetic voltage density respectively.

Equation (2.41) involves material behaviours that are described in the frequency domain as well. The TLM method on the other hand involves time domain calculations. In the case of linear materials the inverse transform from the frequency domain to the time domain is straightforward and is applied only to the electric and magnetic fields, considering other parameters as constants. A dispersive material representation in the frequency domain has frequency dependent parameters that can not be ignored as shown in eqs. (2.42) to (2.45) [2.9,2.13],

$$\overline{\mathcal{D}}(\omega) = \varepsilon_o \overline{\mathcal{E}}(\omega) + \varepsilon_o \chi_e(\omega) \overline{\mathcal{E}}(\omega) \tag{2.42}$$

$$\overline{\mathcal{B}}(\omega) = \mu_o \overline{\mathcal{H}}(\omega) + \mu_o \chi_m(\omega) \overline{\mathcal{H}}(\omega) \tag{2.43}$$

$$\overline{\mathcal{J}_{\mathbf{e}}}(\omega) = \sigma_e(\omega) \overline{\mathcal{E}}(\omega) \tag{2.44}$$

$$\overline{\mathcal{J}_{\mathbf{m}}}(\omega) = \sigma_m(\omega) \overline{\mathcal{H}}(\omega) \tag{2.45}$$

where ω is the natural frequency in [rad/s], χ_m is magnetic susceptibility, σ_e describes the electric conductivity in $[S/\mathrm{m}]$ and σ_m describes a magnetic resistivity in $[\Omega/\mathrm{m}]$. The polarization response of a frequency-dependent material when it is subjected to a time varying electric field can't be instantaneous, such a dynamic response can be described only by a convolution (causal) constitutive relationship.

The multiplication of harmonic functions in the frequency domain is equivalent to convolution in the time domain and the electric flux density is,

$$\begin{aligned} \mathbf{D}(t) &= \varepsilon_o \mathbf{E}(t) + \varepsilon_o \int_{\tau=0}^{\infty} \chi_e(\tau) \mathbf{E}(t-\tau) d\tau \\ &= \varepsilon_o \mathbf{E}(t) + \varepsilon_o \chi_e(t) * \mathbf{E}(t) \end{aligned} \tag{2.46}$$

where the $\chi_e(t)$ is the inverse Fourier transform of $\chi_e(\omega)$ and $*$ is the time domain convolution operator. Similarly magnetic flux density, magnetic voltage density and electric current density are expressed in the time domain form as,

$$\mathbf{B}(t) = \mu_o \mathbf{H}(t) + \mu_o \chi_m(t) * \mathbf{H}(t) \tag{2.47}$$

$$\mathbf{J_e}(t) = \sigma_e(t) * \mathbf{E}(t) \tag{2.48}$$

$$\mathbf{J_m}(t) = \sigma_m(t) * \mathbf{H}(t) \tag{2.49}$$

Substituting eqs. (2.46) to (2.49) into eq. (2.41) leads to the time domain representation that can describe frequency dependent materials,

$$\begin{bmatrix} \nabla \times \mathbf{H} \\ -\nabla \times \mathbf{E} \end{bmatrix} = \begin{bmatrix} \sigma_e * \mathbf{E} \\ \sigma_m * \mathbf{H} \end{bmatrix} + \frac{\partial}{\partial t} \begin{bmatrix} \varepsilon_o \mathbf{E} + \varepsilon_o \chi_e * \mathbf{E} \\ \mu_o \mathbf{H} + \mu_o \chi_m * \mathbf{H} \end{bmatrix}. \tag{2.50}$$

The TLM condensed node model is a discrete time representation of eq. (2.50) using $Z-$transform. The field components evaluated in series and shunt condensed nodes are the same as the fields evaluated in the original nodes presented in section 2.3. The series 2D-TLM formulation using the condensed node method is now presented. More detailed formulation for the 1D, 2D shunt node and 3D node can be found in [2.2]. Figure 2.7 shows the 2D-TLM series condensed node using Paul's port numbering system [2.2]. The node length choice is ($\Delta x = \Delta y = \Delta z = \Delta l$) as stated in section 2.3.1 .

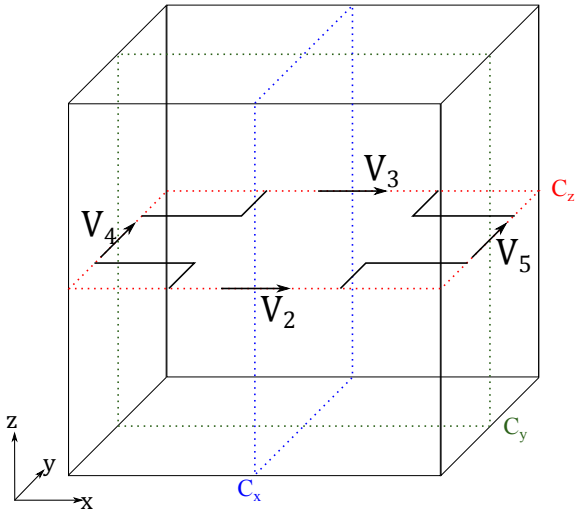

Figure 2.7: The series 2D-TLM condensed node representation

Equation (2.50) is reduced in the case of the series 2D-series node, for which the only non-zero field components are E_x, E_y and H_z, to give:

$$\begin{bmatrix} (\nabla \times H)_x \\ (\nabla \times H)_y \\ (-\nabla \times E)_z \end{bmatrix} = \frac{\partial}{\partial t} \begin{bmatrix} \varepsilon_o E_x \\ \varepsilon_o E_y \\ \mu_o H_z \end{bmatrix} + \begin{bmatrix} \sigma_e * E_x \\ \sigma_e * E_y \\ \sigma_m * H_z \end{bmatrix} + \frac{\partial}{\partial t} \begin{bmatrix} \varepsilon_o \chi_e * E_x \\ \varepsilon_o \chi_e * E_y \\ \mu_o \chi_m * H_z \end{bmatrix}. \tag{2.51}$$

In the original implementation of the condensed node in [2.2,2.10–2.12] a normalization process was introduced for convenience. In this normalization step all the field quantities were represented as voltages and all other quantities were normalized so that they became dimensionless. The electric conductivity and magnetic resistivity

are transformed to dimensionless quantities in the TLM representation as,

$$\sigma_e = \frac{G_e}{\Delta l} = \frac{g_e}{\Delta l}.\frac{\sqrt{2}}{Z_o} \qquad \sigma_m = \frac{R_m}{\Delta l} = \frac{r_m}{\Delta l}.\frac{Z_o}{\sqrt{2}} \tag{2.52}$$

where g_e is the normalized electric conductance and r_m is the normalized magnetic resistance. The impedance of the 2D-TLM series node used in the normalization process is for a free space node $Z_{TL} = \frac{Z_o}{\sqrt{2}}$ and is evaluated as shown in eq. (2.23).

A similar normalization step is applied to the current component I_z used to evaluate the magnetic field so that it will have a voltage dimension rather than an ampere one. This step is done by normalizing the current component using the node impedance so that the circuit representation of the field is as follows,

$$E_{x,y} = -\frac{V_{x,y}}{\Delta l} \qquad H_z = -\frac{I_z}{\Delta l} = -\frac{i_z}{\Delta l}.\frac{\sqrt{2}}{Z_o} \tag{2.53}$$

where i_z is the normalized current.

Equation (2.51) is transformed to the Z-domain by transforming the time derivative to the frequency-domain using a Laplace transform and then to the Z-domain using the bilinear transform [2.2], i.e.

$$\frac{\partial}{\partial t} \rightarrow s = \frac{\bar{s}}{\Delta t} \rightarrow \frac{2}{\Delta t}\left(\frac{1-z^{-1}}{1+z^{-1}}\right), \tag{2.54}$$

where s is the Laplace variable (complex frequency), $\bar{s}$ is the normalized Laplace variable and z is the time-shift operator ($Z-$transform variable).

Finally the spatial derivative is normalized as ,

$$\frac{\partial}{\partial x} = \frac{1}{\Delta l}\frac{\partial}{\partial \bar{x}} \tag{2.55}$$

where $\bar{x}$ is the dimensionless normalized spatial coordinates representing the node index. This spatial normalization is extendible to the curl operation so that it can be normalized as,

$$\overline{\nabla} \times ... = \Delta l \, .\nabla \times ... \tag{2.56}$$

where $\overline{\nabla}$ is the normalized curl operator.

Using algebraic manipulation by substituting all the normalization steps introduced in eqs. (2.52) to (2.56) into eq. (2.51) a normalized TLM representation for the reduced Maxwell's equations can be presented as,

$$\begin{bmatrix} (\overline{\nabla} \times \bar{i})_x \\ (\overline{\nabla} \times \bar{i})_y \\ (-\overline{\nabla} \times \overline{V})_z \end{bmatrix} = \overline{s} \begin{bmatrix} V_x \\ V_y \\ 2i_z \end{bmatrix} + \begin{bmatrix} g_e V_x \\ g_e V_y \\ r_m i_z \end{bmatrix} + \overline{s} \begin{bmatrix} \chi_e V_x \\ \chi_e V_y \\ 2\chi_m i_z \end{bmatrix}. \tag{2.57}$$

Stoke's theorem converts the surface integral of curl equations to a line integral over the surface boundary and is written in the general form as

$$\iint_S curl\ \boldsymbol{F}.\ dS = \oint_C F\ .\ dr \tag{2.58}$$

where $\boldsymbol{F}$ is a vector field existing over an open surface S and is enclosed by a closed curve c.

Stoke's theorem is applied to eq. (2.57) using the integration contours $C_y,\ C_x,\ and\ C_z$ shown in fig. 2.7. The top view for the integration contours is shown in fig. 2.8 illustrating the intersections between the port voltages and the integration contours for the 2D-TLM series node.

The curl fields from the left hand side of eq. (2.57) are transformed using Stokes' theorem as follows,

$$\begin{bmatrix} (\overline{\nabla} \times \bar{i})_x \\ (\overline{\nabla} \times \bar{i})_y \\ (-\overline{\nabla} \times \overline{V})_z \end{bmatrix} \rightarrow \begin{bmatrix} \oint_{C_x} \bar{i}_x.dx \\ \oint_{C_y} \bar{i}_y.dy \\ -\oint_{C_z} \bar{V}_z.dz \end{bmatrix} \rightarrow \begin{bmatrix} (V_2 + V_3) \\ (V_4 + V_5) \\ -(V_2 + V_5 - V_3 - V_4) \end{bmatrix} \tag{2.59}$$

Equation (2.57) becomes,

$$\begin{bmatrix} (V_2 + V_3) \\ (V_4 + V_5) \\ -(V_2 - V_3 - V_4 + V_5) \end{bmatrix} = \overline{s} \begin{bmatrix} V_x \\ V_y \\ 2i_z \end{bmatrix} + \begin{bmatrix} g_e V_x \\ g_e V_y \\ r_m i_z \end{bmatrix} + \overline{s} \begin{bmatrix} \chi_e V_x \\ \chi_e V_y \\ 2\chi_m i_z \end{bmatrix}. \tag{2.60}$$

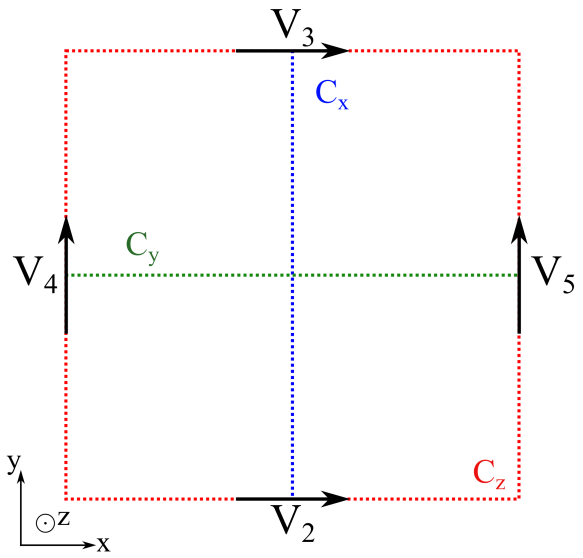

Figure 2.8: Top view of the series 2D-TLM node showing the integration contours C_x, $C_y$andC_z

The four sections of transmission lines forming the 2D-TLM series node are then transformed to a simple TLM circuit using both the Thevenin equivalent circuit from fig. 2.5.b and eq. (2.60). The 2D-TLM series node and its Thevenin equivalent circuit are shown in fig. 2.9.

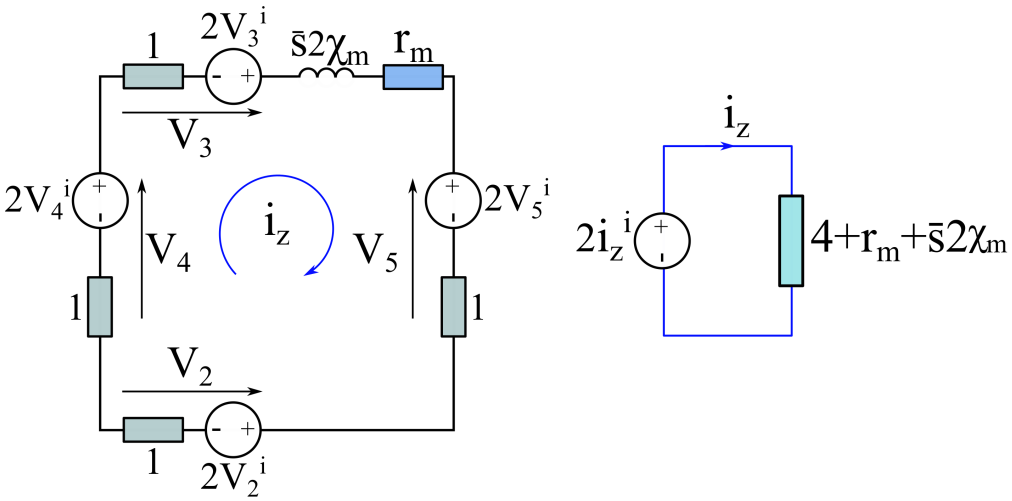

Figure 2.9: 2D TLM series node and its Thevenin equivalent circuit

where V_2^i,V_3^i,V_4^i and V_5^i are the incident voltages of the node ports.

Equation (2.60) is then modified in order to obtain the nodal voltages using incident

pulses. The incident and reflected voltage impulses at each node now can be defined using $\boldsymbol{V}^i$ and $\boldsymbol{V}^r$ matrices respectively in the form of

$$\begin{aligned} \boldsymbol{V}^i &= \begin{bmatrix} V_2^i & V_3^i & V_3^i & V_4^i \end{bmatrix}^T, \\ \boldsymbol{V}^r &= \begin{bmatrix} V_2^r & V_3^r & V_3^r & V_3^r \end{bmatrix}^T, \end{aligned} \tag{2.61}$$

where the superscript T denotes transpose of the matrix.

The nodal excitation fields matrix $\boldsymbol{F}^i$ is related to the incident voltages as [2.2]

$$\boldsymbol{F}^i = \begin{bmatrix} V_x^i & V_y^i & i_z^i \end{bmatrix}^T,$$

$$\begin{bmatrix} V_x^i \\ V_y^i \\ i_z^i \end{bmatrix} = \begin{bmatrix} 1 & 1 & 0 & 0 \\ 0 & 0 & 1 & 1 \\ 1 & -1 & -1 & 1 \end{bmatrix} \times \begin{bmatrix} V_2^i \\ V_3^i \\ V_3^i \\ V_4^i \end{bmatrix} = \boldsymbol{R}^i \boldsymbol{V}^i \tag{2.62}$$

where $\boldsymbol{R}^i$ is the cell excitation matrix.

Using the Thevenin equivalent circuit from fig. 2.9 the nodal voltage and nodal current are then obtained from the excitation field matrix using

$$\boldsymbol{F} = \begin{bmatrix} V_x & V_y & i_z \end{bmatrix}^T,$$

$$\begin{bmatrix} V_x \\ V_y \\ i_z \end{bmatrix} = \begin{bmatrix} t_{ex} & 0 & 0 \\ 0 & t_{ey} & 0 \\ 0 & 0 & -t_{mz} \end{bmatrix} \times \begin{bmatrix} V_x^i \\ V_y^i \\ i_z^i \end{bmatrix} = \boldsymbol{T} \boldsymbol{F}^i \tag{2.63}$$

where $\boldsymbol{T}$ is the transmission coefficient matrix and t_{ex}, t_{ey} and t_{mz} depend on the normalized parameters of the modelled material. For a material with constant electric and magnetic parameters the general transmission coefficients for the 2D-TLM

series node are obtained from [2.2] as

$$\begin{aligned} t_{ex} = t_{ey} &= \frac{2}{2 + g_e + \bar{s}\chi_e}, \\ t_{mz} &= \frac{2}{4 + r_m + 2\bar{s}\chi_m}. \end{aligned} \tag{2.64}$$

Reflected voltages can be calculated based on the calculated nodal fields, V_x, V_y *and* i_z, to be

$$\begin{bmatrix} V_2 \\ V_3 \\ V_4 \\ V_5 \end{bmatrix}^r = \begin{bmatrix} V_x + i_z - V_3^i \\ V_x - i_z - V_2^i \\ V_y - i_z - V_5^i \\ V_y + i_z - V_4^i \end{bmatrix} \tag{2.65}$$

Frequency dependent materials can be implemented using non-constant parameters i.e, $\chi_e(\omega)$ and $\sigma(\omega)$ before applying the Laplace and Z-transforms. Implementation of such materials is presented in chapter 4 which describes electromagnetic-thermal and how a dispersive plasma can be modelled.

2.6 Summary

The transmission line modelling (TLM) method is introduced and derived from first principles, showing the analogy between circuit theory and solving Maxwell's equations. Different techniques have been introduced to model complex and dispersive materials giving more generality to the numerical method. Only the electromagnetic (EM) side of the TLM method is introduced in this chapter for solving the propagation term of the general wave equation.

References

[2.1] C. Christopoulos, *The Transmission-Line Modeling Method TLM*. Piscataway, NJ: IEEE Press, 1995.

[2.2] J. Paul, "Modelling of general electromagentic material properties in TLM," PhD thesis, Univeristy of Nottingham, 1998.

[2.3] J. C. Maxwell, "A Dynamical Theory of the Electromagnetic Field," *Philosophical Transactions of the Royal Society of London*, vol. 155, pp. 459–512, 1865.

[2.4] O. Heaviside, *Electromagnetic theory*. London: "The Electrician" printed and published, 1893, vol. 1.

[2.5] ——, *Electromagnetic theory*. London: "The Electrician" printed and published, 1899, vol. 2.

[2.6] B. J. Hunt, "Oliver Heaviside: A first-rate oddity," *Physics Today*, vol. 65, no. 11, p. 48, 2012.

[2.7] S. Ramo, J. R. Whinnery, and T. Van Duzar, *Fields and Waves in Communication Electronics*, 3rd ed. John Wiley & Sons, Inc., 1997.

[2.8] C. Christopoulos, *An introduction to applied electromagnetism*. John Wiley & Sons, 1990.

[2.9] D. H. Staelin, *Electromagnetics and Applications*. Department of Electrical Engineering and Computer Science, Massachusetts Institute of Technology, 2011. [Online]. Available: https://ocw.mit.edu/courses/electrical-engineering-and-computer-science/6-013-electromagnetics-and-applications-spring-2009/readings/MIT6_013S09_

notes.pdf

[2.10] J. Paul, C. Christopoulos, and D. Thomas, "Generalized material models in TLM - part 3: Materials with nonlinear properties," *IEEE Transactions on Antennas and Propagation*, vol. 50, no. 7, pp. 997–1004, 2002.

[2.11] J. Paul, C. Christopoulos, and D. D. W. P. Thomas, "Generalized material models in TLM part II. Materials with anisotropic properties," *IEEE Transactions on Antennas and Propagation*, vol. 47, no. 10, pp. 1535–1542, 1999.

[2.12] J. Paul, C. Christopoulos, and D. W. P. Thomas, "Generalized material models in TLM Part I : Materials with frequency-dependent properties," vol. 47, no. 10, pp. 1528–1534, 1999.

[2.13] C. A. Balanis, *Advanced Engineering Electromagnetics*. Wiley, New York, 1989.

3

Thermal diffusion in TLM

This chapter focuses on the transmission line modelling (TLM) method for thermal diffusion problems. Heat conduction is represented in this chapter as a phenomenon that falls under this type of problem. Thermal TLM has been used previously for a variety of applications such as modelling of heat conduction in transistors [3.1], microwave food heating [3.2,3.3], heat transfer in complex geometrics such as a jet engine turbine blade [3.4], and for the thermal investigation of insulator gate bipolar transistors (IGBT) [3.5]. A magneto-optic mutli-layered media was modelled in [3.6,3.7] which compares results of thermal TLM with semi-analytical methods. Transient 3D heat flow analysis for integrated circuit devices using thermal TLM is presented in [3.8] and recent work has been done modelling thermal diffusion in biological tissues as a method to identify the areas with tumour cells as presented in [3.9].

This chapter overviews the theoretical background of diffusion problems followed by a derivation of the analogy between the heat conduction process and transmission line equivalent circuits. A formulation of the thermal 2D-TLM node is given. A stub technique for modelling materials with different thermal properties is also presented. Practical differences, such as

the choice of background material between the electromagnetic TLM (EM-TLM) method introduced in chapter 2 and thermal-TLM are highlighted throughout the chapter.

* * *

3.1 Heat diffusion

Scientists had started to experiment on heat flow in the eighteenth and early nineteenth centuries. Several attempts led by different scientists to explain the process of heat transfer came to same conclusion stating that "The overall driving force for heat flow processes is the cooling (or levelling) of the thermal gradient within our universe" [3.10]. This fact meant that heat transfer between objects will continue until thermal equilibrium with the surroundings is achieved [3.10]. Conduction, convection and radiation are the only known heat transfer forms.

Thermal conduction has been experimented with for a long time. Joseph Fourier formulated the complete expositions of the heat conduction theory in his book in 1822 [3.10,3.11]. Fourier's law stated that the heat flux $\mathbf{q}_{th}(W/m^2)$ caused by thermal conductance is proportional to the magnitude of temperature gradient and opposite to it in sign, which can be written in the 3D form to be as [3.10],

$$\mathbf{q}_{th} = -k_{th}\nabla T \tag{3.1}$$

where k_{th} is the thermal conductivity in $[W/m.K]$, ∇ is the gradient operator and in the case of a 3D Cartesian coordinate system is $\nabla = (\frac{\partial}{\partial x}, \frac{\partial}{\partial y}, \frac{\partial}{\partial z})$, and ∇T is temperature gradient as function of space and time $\rightarrow \nabla T(x, y, z; t)$ in Kelvin[K].

Solving complex systems based on equations that arise only from eq. (3.1) is near impossible due to the fact that T and $\mathbf{q}_{th}$ are mutually dependent variables. Ap-

plying the first law of thermodynamics on a closed system can be used to eliminate the $\mathbf{q}_{th}$ term to obtain a general solution for thermal diffusion in complex systems. Only energy is allowed in or out of a closed system preventing any mass or matter transfer between the system and the surrounding enclosure, [3.12].

The first law of thermodynamics is similar to the conservation of energy law and can be written for a closed system as [3.12],

$$\Delta U = \underbrace{q}_{\text{heat J}} + \underbrace{w}_{\text{work J}} \tag{3.2}$$

where ΔU is the change in internal energy U, q is the heat energy added or removed from the system and w is the work done on or by the system. In other words this law states that the internal energy of a closed system can either be increased or decreased based on whether heat is delivered or withdrawn from the system when there is no work done on or by the system. The energy interaction is considered a heat transfer if temperature difference is the deriving force of such an interaction. In practical engineering applications, studying the heat and the energy transfer rate is more important than studying the values of these quantities i.e. (heat and energy exchanged). The rate of change with time for these quantities in Equation (3.2) can be rewritten as ,

$$\underbrace{\frac{dU}{dt}}_{\substack{\text{Positive when}\\ \text{the system's}\\ \text{energy increases}}} = \underbrace{Q}_{\substack{\text{Positive toward}\\ \text{the sytem}}} + \underbrace{W}_{\substack{\text{Positive toward}\\ \text{the sytem}}} \tag{3.3}$$

where $Q = \frac{dq}{dt}$ is the heat transfer rate in (J/s) or Watts(W), $W = \frac{dw}{dt}$ is the work transfer rate and $\frac{dU}{dt}$ is thermal internal energy rate of change. The heat transfer analysis can be obtained without referring to work transfer rate but in real systems there are many situations in which they are combined. This chapter focuses only on the thermal energy transfer (heat transfer) therefore the work caused by heat transfer, such as the change in volume or pressure, is not considered in final calculations. If a system was allowed to have a variable volume and pressure, the work term will have a contribution towards the calculations. The modelled engineering applications

in this thesis were considered to be under a constant pressure and volume therefore the work transfer rate component can be omitted from further calculations reducing eq. (3.3) to [3.10,3.12]

$$Q = \frac{dU}{dt} \tag{3.4}$$

In thermodynamics, the heat transfer rate in eq. (3.4) is commonly studied for two special cases of systems (a) constant volume and varying pressure (b) constant pressure and varying volume. For both cases the heat transfer rate is linked to the rate of change in the system temperature as,

$$\begin{aligned} &\text{Constant volume process :} \quad Q = \frac{dU}{dt} = mc_v \frac{dT}{dt} \\ &\text{Constant pressure process :} \quad Q = \frac{dH}{dt} = mc_p \frac{dT}{dt} \end{aligned} \tag{3.5}$$

where p is pressure and V is volume, $H = U + pdV$ is referred to as enthalpy and is related to fluids and gases states more than solid state and also is referring to the work done by the system (pdV), c_v and c_p are the specific heat capacities at constant volume and constant pressure respectively in (J/kg K). Liquids and solids are often referred to as incompressible materials in which the material volume stays constant for any value of pressure. For incompressible materials the two specific heat capacities are equal. Equation (3.4) can be reduced for incompressible materials as, [3.10,3.12]

$$Q = \frac{dU}{dt} = mc_h \frac{dT}{dt} \tag{3.6}$$

where $c_h = c_v = c_p$. In later chapters specific heat capacity at constant volume is used when gaseous materials are modelled, otherwise materials are considered incompressible. The approximation of a constant volume was followed for any modelled application throughout the thesis.

Figure 3.1 shows a control volume for a closed system of a thermal conducting material for analysis using Fourier's law eq. (3.1) and the first law of thermodynamics eq. (3.2). The system surface and volume are denoted as S and R respectively. A surface element indicated as dS is considered for analyzing the heat flow out of the

system. Two vectors are identified on the surface element dS: one is the unit normal to the surface $\hat{n}$ and the other one is the heat flux away from the system obtained using the Fourier law as $\mathbf{q}_{th} = -k_{th}\nabla T$.

A possibility for the system to have a distributed volumetric internal heat release source as $\dot{q}(r)\ W/m^3$ is allowed. This heat release source might be due to a chemical or nuclear reaction or, as considered in this thesis, due to Joule heating (electric resistance heating).

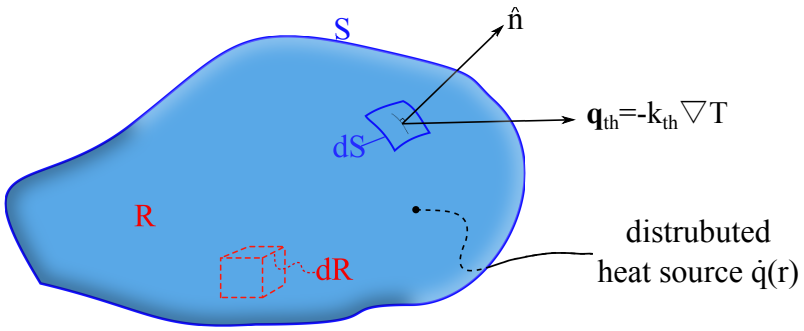

Figure 3.1: Control volume of for a closed volume R of a thermally conducting material surrounded by a closed surface S.

The heat energy conducted normal to dS in Watts becomes,

$$(-k_{th}\nabla T).\ (\hat{n}dS). \tag{3.7}$$

Therefore the overall heat energy in the volume R is obtained using,

$$Q = \iint_S ((-k_{th}\nabla T).\hat{n}dS))\ ds + \iiint_R \dot{q}dR \tag{3.8}$$

Applying thermodynamic laws from eq. (3.6) to the system and considering the volumetric calculation allows the rate of internal energy increase to be obtained as,

$$\frac{dU}{dt} = \iiint_R \left(\rho c_h \frac{\partial T}{\partial t}\right)\ dR \tag{3.9}$$

where ρ is the volumetric mass density in $(\mathrm{kg/m^3})$.

Substituting eq. (3.8) and eq. (3.9) into eq. (3.6) and rearranging the terms leads to,

$$\iint_S k_{th} \nabla T . \hat{n} dS = \iiint_R \left[\rho c_h \frac{\partial T}{\partial t} - \dot{q} \right]. \tag{3.10}$$

Gauss's theorem can be used to convert a surface integral to a volume integral. Gauss's theorem states that for any continuous function $\mathbf{g}$ in space it can be converted to volume integral as,

$$\iint_S \mathbf{g}.\ \mathbf{n} dS = \iiint_R \nabla . \mathbf{g} dR. \tag{3.11}$$

Therefore, if $\mathbf{g}$ is identified as $(k_{th} \nabla T)$, eq. (3.10) reduces to,

$$\iiint_R (\nabla\ .\ k_{th} \nabla T - \rho c_h \frac{\partial T}{\partial t} + \dot{q}) dR = 0. \tag{3.12}$$

Since the volume R is arbitrary the only way for the integral to vanish is by having the integrand equal to zero, i.e.

$$\nabla . k_{th} \nabla T + \dot{q} = \rho c_h \frac{\partial T}{\partial t} \tag{3.13}$$

Assuming an homogeneous medium that has fixed and temperature independent thermal conductivity everywhere, and in the absence of self-generated heat ($\dot{q} = 0$), rearranging eq. (3.13) leads to the heat diffusion equation that describes the temperature distribution in a system over time as [3.10],

$$\nabla^2 T = \frac{\rho c_h}{k_{th}} \frac{\partial T}{\partial t} = \frac{1}{\alpha} \frac{\partial T}{\partial t} \tag{3.14}$$

where α is the thermal diffusivity in $[m^2/s]$ and is a measure of how rapidly a material can divert heat from the source.

Equation (3.14) represents the main equation describing a heat transfer in a system which is used in the next section to draw the analogy between TLM and heat diffusion. In this equation an assumption was made for the thermal conductivity to be independent of the material temperature. This assumption is not true for many real life applications where thermal conductivity is dependent on the material temperature. This is one of the limitations of the presented model in this thesis and is further discussed in the conclusion in chapter 7

3.2 Formulation of thermal 2D-TLM

In this section the analogy between the heat diffusion equation, eq. (3.14), and the TLM method is presented for a general 2D case. Equation (3.14) is reduced to the 2D case by requiring that $\frac{\partial}{\partial z} = 0$ and temperature is represented as a function of two spatial coordinates and time, i.e. $T(x, y; t)$, and obeys

$$\frac{\partial^2 T}{\partial x^2} + \frac{\partial^2 T}{\partial y^2} = \frac{\rho C_p}{K_{th}} \frac{\partial T}{\partial t} = \frac{1}{\alpha} \frac{\partial T}{\partial t}. \tag{3.15}$$

The wave equation propagating in a lossy material was introduced in eqs. (2.6) to (2.8) and (2.13). Following the same representation, the lossy 2D-shunt node in TLM can be represented as [3.13],

$$\frac{\partial^2 \phi}{\partial x^2} + \frac{\partial^2 \phi}{\partial y^2} = \underbrace{4R_d C_d \frac{\partial \phi}{\partial t}}_{\text{Diffusion term}} + \underbrace{2L_d C_d \frac{\partial^2 \phi}{\partial t^2}}_{\text{Wave Term}}, \tag{3.16}$$

where ϕ is a scalar function representing the potential of the network $\phi = V$. Equation (3.16) supports both wave and diffusion like behaviour. If the time step was chosen so that $(4R_d C_d \frac{\partial \phi}{\partial t} \gg 2L_d C_d \frac{\partial^2 \phi}{\partial t^2})$, the TLM method is then considered to be suitable for modelling only a diffusion like behaviour. Rewriting the TLM solution to accommodate only a diffusion behaviour and replacing the scalar function with Voltage V, eq. (3.16) takes the form of,

$$\frac{\partial^2 V}{\partial x^2} + \frac{\partial^2 V}{\partial y^2} = 4R_d C_d \frac{\partial V}{\partial t}. \tag{3.17}$$

Comparing eq. (3.15) with eq. (3.17) heat diffusion as thermal conduction can be modelled in TLM when the corresponding variables between the EM transmission line circuit and thermal analogy are matched as,

$$V \leftrightarrow T, \qquad R_d = \frac{1}{2K_{th}.A}, \qquad C_d = \frac{\rho C_p.A}{2}, \tag{3.18}$$

where $A = \Delta l \Delta z$ is the nodal area that includes the thickness of block of material in the z-direction. As in chapter 2 the assumption will be made that node dimensions are the same, i.e., $\Delta x = \Delta y = \Delta z = \Delta l$.

A lossy 2D-TLM node representation for diffusion problems is shown in Figure 3.2.

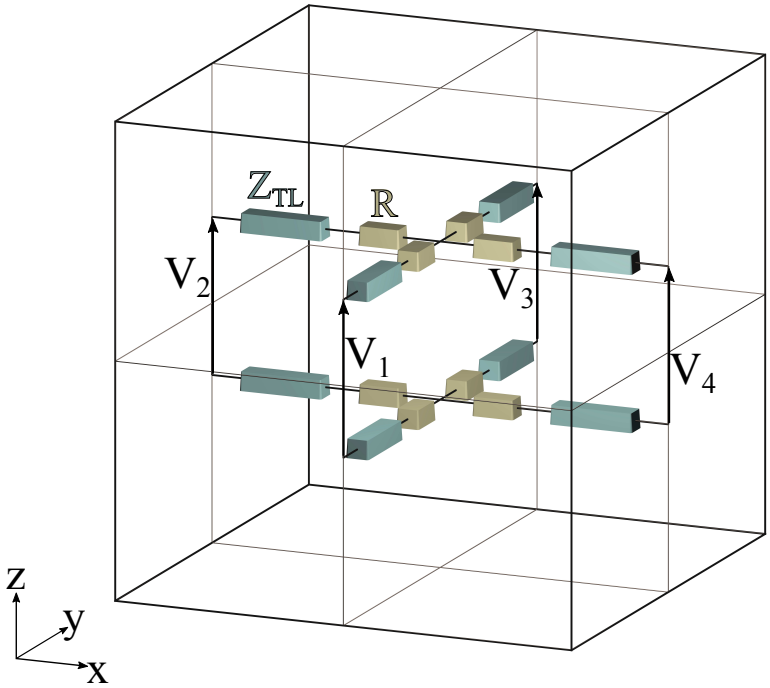

Figure 3.2: A lossy 2D-TLM shunt node representation

The transmission line description of thermal diffusion only contains capacitance and resistance, specifically there is no inductance in the model, unlike the electromagnetic (EM) transmission line model introduced in chapter 2 that in the lossy case utilizes all 4 parameters (R,G,L,C)] [3.14]. This propriety of thermal diffusion requires the TLM impedance to be calculated from the capacitive component only.

Recall from chapter 2 that the important properties of TLM i.e., velocity of propagation and characteristic impedance for the transmission line, are

$$u = \sqrt{\frac{1}{\frac{L}{\Delta l}\cdot\frac{C}{\Delta l}}} \quad , \qquad Z_{TL} = \sqrt{\frac{L}{C}} \tag{3.19}$$

Starting from the fact that the speed of propagation is also $u = \frac{\Delta l}{\Delta t}$, then the

transmission line impedance can be obtained from

$$Z_{TL} = \frac{\Delta t}{C}. \tag{3.20}$$

Summarizing the analogy, it can be seen that 2D-TLM can be used for solving heat conduction problems when the following transmission line parameters are used,

$$R = R_d \Delta l = \frac{\Delta l}{2K_{th}A}, \qquad C = C_d \Delta l = \frac{\rho C_p A \Delta l}{2}, \qquad Z_{TL} = \frac{\Delta t}{C}. \tag{3.21}$$

The implementation of the lossless 2D-TLM series node (i.e. no resistance included) was presented in section 2.3. In the other hand the thermal node depends only on the thermal capacitance and resistance introducing losses to the calculations. The Thevenin equivalent circuit for the general lossy 2D-TLM shunt node of Figure 3.2 is shown in Figure 3.3 [3.14,3.15].

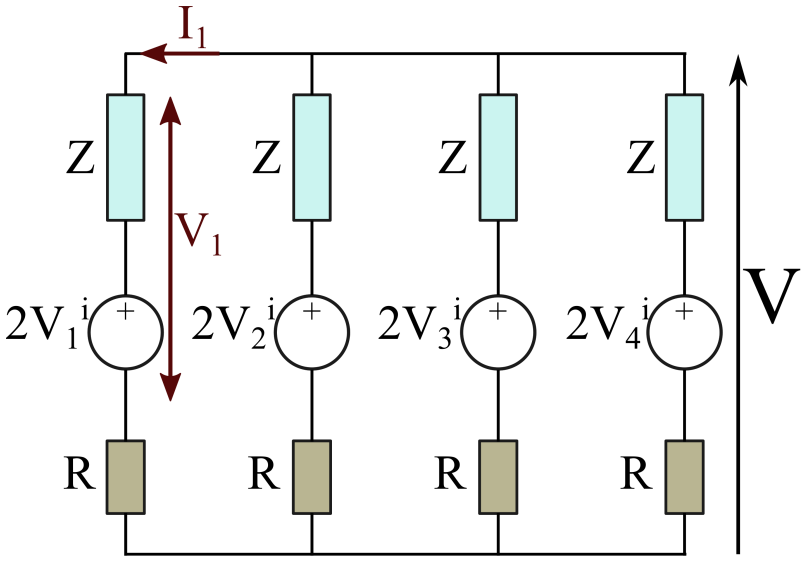

Figure 3.3: Lossy 2D-TLM shunt node Thevenin equivalent circuit

where $V_1^i(n_x, n_y)$, $V_2^i(n_x, n_y)$, $V_3^i(n_x, n_y)$ *and* $V_4^i(n_x, n_y)$ represent the voltages incident at ports. Voltages in this section actually refer to the temperature T but are kept as voltages to keep the description consistent with the TLM algorithm. The voltage at the node (n_x, n_y) i.e.V shown in Figure 3.3, at time step k is represented

by ${}_kV(n_x, n_y)$ and can be calculated from,

$$
\begin{aligned}
{}_kV(n_x, n_y) &= \frac{\left(\frac{2_kV_1^i(n_x,n_y)}{R+Z} + \frac{2_kV_2^i(n_x,n_y)}{R+Z} + \frac{2_kV_3^i(n_x,n_y)}{R+Z} + \frac{2_kV_4^i(n_x,n_y)}{R+Z}\right)}{\left(\frac{4}{R+Z}\right)} \\
&= 0.5\Big({}_kV_1^i(n_x, n_y) + {}_kV_2^i(n_x, n_y) + {}_kV_3^i(n_x, n_y) + {}_kV_4^i(n_x, n_y)\Big).
\end{aligned}
\tag{3.22}
$$

Lossy TLM has a different scattering process to the general TLM node considered in Section 2.3.1. The voltage at the resistance is not considered during the scattering process. This reduces the scattered voltage at the node proportionally to the resistance value, hence introducing losses in the model. The scattering is described using port(1) as an example.

The current passing through port(1) can be calculated from,

$$
I_1 = \frac{V - 2_kV_1^i}{R + Z}. \tag{3.23}
$$

Then the voltage V_1 shown in fig. 3.3 is obtained from,

$$
V_1 = 2_kV_1^i + I_1Z = V - I_1R \tag{3.24}
$$

The reflected voltage at port(1) will then be,

$${}_kV_1^r = V_1 - {}_kV_1^i = \frac{0.5Z({}_kV_2^i + {}_kV_3^i + {}_kV_4^i)}{R + Z} + \frac{R - 0.5Z}{R + Z}{}_kV_1^i. \tag{3.25}$$

The reflected voltages at the other ports can be obtained in a similar way and represented in matrix form as:

$$
\begin{bmatrix} {}_kV_1^r \\ {}_kV_2^r \\ {}_kV_3^r \\ {}_kV_4^r \end{bmatrix} = \frac{0.5Z}{R+Z} \begin{bmatrix} \frac{2R}{Z} - 1 & 1 & 1 & 1 \\ 1 & \frac{2R}{Z} - 1 & 1 & 1 \\ 1 & 1 & \frac{2R}{Z} - 1 & 1 \\ 1 & 1 & 1 & \frac{2R}{Z} - 1 \end{bmatrix} \begin{bmatrix} {}_kV_1^i \\ {}_kV_2^i \\ {}_kV_3^i \\ {}_kV_4^i \end{bmatrix} \tag{3.26}
$$

The connection process will exchange information between the adjacent ports of different nodes. According to the port numbering shown in Figure 3.2 the connection

process is [3.14–3.16],

$$
\begin{aligned}
{}_{k+1}V_1^i(n_x, n_y) &=_k V_3^r\big(n_x, (n_y - 1)\big),\\
{}_{k+1}V_2^i(n_x, n_y) &=_k V_4^r\big((n_x - 1), n_y\big),\\
{}_{k+1}V_3^i(n_x, n_y) &=_k V_1^r\big(n_x, (n_y + 1)\big),\\
{}_{k+1}V_4^i(n_x, n_y) &=_k V_2^r\big((n_x + 1), n_y\big).
\end{aligned}
\tag{3.27}
$$

3.3 Modelling different materials in thermal TLM

Real life applications rarely consist of a single material. As described in Chapter 2 different materials are implemented in the TLM method using the stub technique. In the EM-TLM described in chapter 2 free space was used to represent the background material, allowing other materials to be modelled by adding capacitive or inductive stubs that represent the dielectric or magnetic properties of the material respectively. Thermal materials on the other hand don't have a reference material in which heat will diffuse faster than all other materials. Therefore an extra step is necessary before modelling any thermal application, in which a comparison between the modelled materials is done to obtain the values for a material that can be used as background for that specific thermal model.

The importance of the background material in thermal modelling is due to the fact that the thermal-TLM time step is related to the background material's parameters.The time step of thermal-TLM has to be significantly less than the time constant (RC) [3.16] in order to satisfy the condition of a modelling diffusion phenomenon; the thermal time step is evaluated using,

$$
\Delta t \ll RC \longrightarrow \Delta t \ll \frac{\rho C_p \Delta l^2}{4K_{th}},
\tag{3.28}
$$

Choosing the time step to be much smaller than RC will guarantee that the condition specified in 3.16 for modelling diffusion behaviour to hold. The "optimum" material to be used as a background material would have minimum density and heat capacity

and a maximum thermal conductance. A comparison of different Δt parameters obtained for the different materials to be modelled is needed before creating the model. This step will a guarantee stability of the model due to the fact that all the additional stubs will be of the form of an added impedance (positive). This step allows for more flexibility with the time step choice in the thermal TLM method compared to the EM-TLM as shown in chapter 2.

Material capacitance is, when modelled using the stub technique, split into the link-line (characteristic) impedance and stub impedance. The extra capacitance of the modelled material is equal to the difference between the modelled capacitance and the background capacitance.

$$C_s = C_m - C_{bk} \tag{3.29}$$

where C_s is the extra capacitance modelled using the stub, which is then used to evaluate the capacitive stub impedance, as previously shown in section 2.4 for the EM 1D-TLM case. From [3.7],

$$Z_s = \frac{\Delta t/2}{C_s} \tag{3.30}$$

The Thevenin equivalent for the 2D-TLM node when the stub impedance is included is shown in Figure 3.4, where V_s and Z_s are the incident voltage at the stub and the stub impedance respectively.

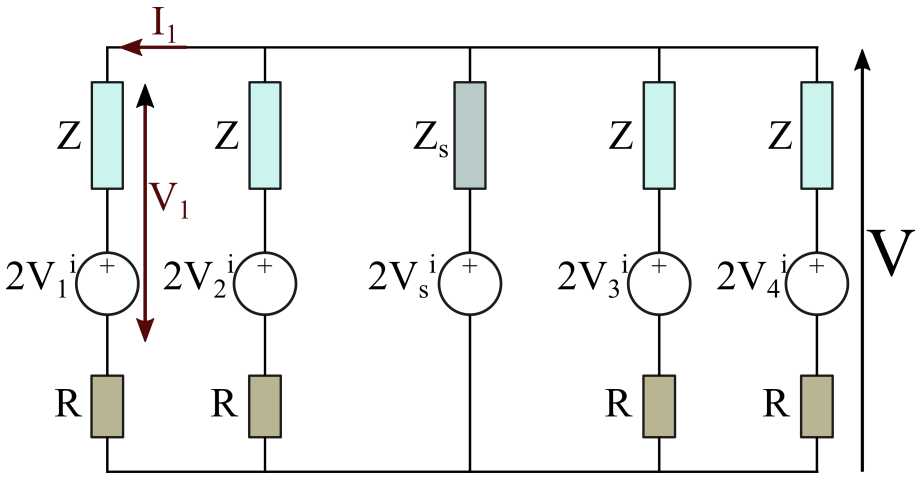

Figure 3.4: The Thevenin equivalent circuit for a lossy 2D-TLM shunt node with stub

Nodal voltage calculation is now modified to accommodate the stub incident voltage ${}_kV_s^i(n_x, n_y)$ and the stub impedance Z_s and is calculated as,

$$ {}_kV(n_x, n_y) = \frac{\left[\frac{2_kV_1^i(n_x,n_y)}{R+Z} + \frac{2_kV_2^i(n_x,n_y)}{R+Z} + \frac{2_kV_3^i(n_x,n_y)}{R+Z} + \frac{2_kV_4^i(n_x,n_y)}{R+Z} + \frac{2_kV_s^i(n_x,n_y)}{Z_s}\right]}{\left[\frac{4}{R+Z} + \frac{1}{Z_s}\right]}. \tag{3.31} $$

The scattering process is implemented using a similar approach to that applied to the lossy shunt 2D-TLM node in section 3.2. The port current is evaluated and then used to calculate the reflected voltage considering the losses introduced by the port resistance. This process is shown here for port 1 and the current at the port 1 is

$$ I_1 = \frac{V - 2_kV_1^i}{R+Z}, \tag{3.32} $$

and the voltage V_1 on the transmission line is

$$ V_1 = 2_kV_1^i + I_1Z = V - I_1R \tag{3.33} $$

The reflected voltage is obtained as,

$$ \begin{aligned} {}_kV_1^r &= V_1 - {}_kV_1^i = {}_kV_1^i + I_1Z \\ &= \frac{Z(V - 2V_1^i)}{R+Z} + V_1^i. \end{aligned} \tag{3.34} $$

Reflected voltages at the other ports $2_kV_2^r$, $2_kV_3^r$ and $2_kV_4^r$ are obtained similarly.

The reflected voltage of the stub is evaluated from,

$$ V_s^r = V - V_s^i. \tag{3.35} $$

The connection process is the same as for the general node and as described in eq. (3.27). For the stub voltage the incident voltage at the time step $k+1$ is,

$$ {}_{k+1}V_s^i = {}_kV_s^r. \tag{3.36} $$

3.4 Heat source modelling

In many applications, such as optical nano-heat sources and arc discharges [3.17, 3.18] the presence of an external heat source is needed. External heat sources are important to model heat release in the system, and can be implemented either as a voltage source (equivalent to a temperature input) or as a current source (equivalent to a heat energy input). Figure 3.5 shows an external current I_s as a heat source. It is important to consider the units used for the current source when assigning a value. The heat source represented in Figure 3.5 has units of Watts(W) which will require scaling a heat flux input using the thermal node dimensions. This will be described in detail in chapter 4.

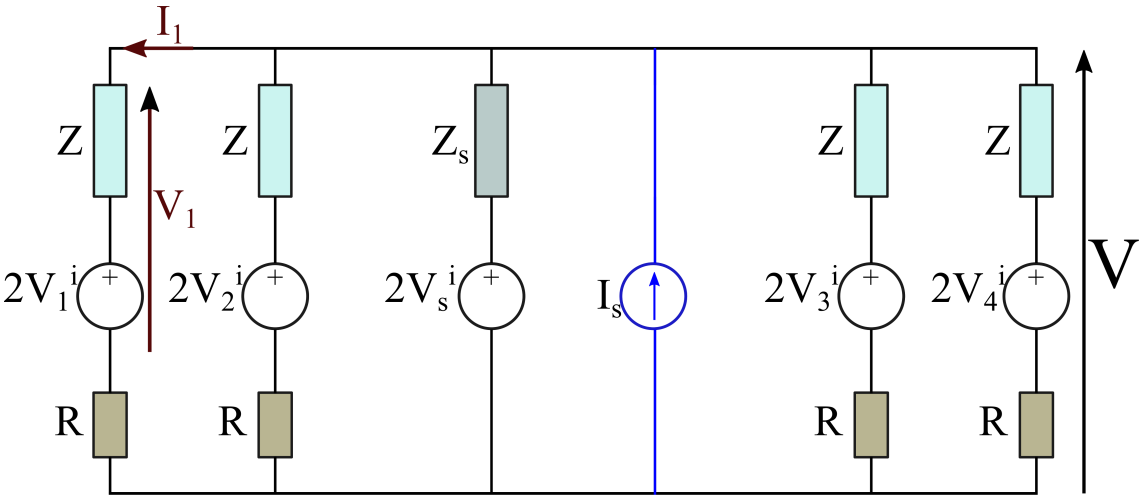

Figure 3.5: The Thevenin equivalent circuit for a lossy 2D-TLM shunt node after adding the current source and the capacitive stub

The nodal voltage calculation in the presence of an external heat source obtained from circuit in fig. 3.5,

$$ {}_kV(n_x,n_y) = \frac{\left[\frac{2_kV_1^i(n_x,n_y)}{R+Z} + \frac{2_kV_2^i(n_x,n_y)}{R+Z} + \frac{2_kV_3^i(n_x,n_y)}{R+Z} + \frac{2_kV_4^i(n_x,n_y)}{R+Z} + + \frac{2_kV_s^i(n_x,n_y)}{Z_s} + I_s\right]}{\left[\frac{4}{R+Z} + \frac{1}{Z_s}\right]}. \tag{3.37} $$

while the scattering and connection process remain unchanged.

3.5 Summary

This chapter introduced the thermal model and derived the analogy between circuit theory and heat diffusion equations. It demonstrated the practical differences between EM-TLM and thermal TLM in term of modelling different materials and time step calculations. As both EM and thermal TLM have now have been introduced, the next chapter focuses on the coupling of the two methods.

References

[3.1] R. Hocine, A. Boudghene Stambouli, and A. Saidane, "A three-dimensional TLM simulation method for thermal effect in high power insulated gate bipolar transistors," *Microelectronic Engineering*, vol. 65, no. 3, pp. 293–306, 2003.

[3.2] C. Flockhart, "The simulation of coupled electromagnetic and thermal problems in microwave heating," in *Second International Conference on Computation in Electromagnetics*, vol. 1994, no. 4. London: IEE, 1994, pp. 267–270.

[3.3] C. Christopoulos, "The application of time-domain numerical simulation methods to the microwave heating of foods," *IMA Journal of Management Mathematics*, vol. 5, no. 1, pp. 385–397, 1993.

[3.4] S. Pulko, A. Mallik, and P. B. Johns, "Application of transmission-line modelling (TLM) to thermal diffusion in bodies of complex geometry," *International Journal for Numerical Methods in Engineering*, vol. 23, no. 12, pp. 2303–2312, 1986.

[3.5] R. Hocine, S. H. Pulko, A. B. Stambouli, and A. Saidane, "TLM method for thermal investigation of IGBT modules in PWM mode," *Microelectronic*

Engineering, vol. 86, no. 10, pp. 2053–2062, 2009.

[3.6] E. W. Williams, H. C. Patel, D. D. Cogan, and S. H. Pulko, "TLM modelling of thermal processes in magneto-optic multi-layered media," *Journal of Physics D: Applied Physics*, vol. 29, no. 5, pp. 1124–1132, 1996.

[3.7] H. C. Patel, "Non-linear 3D modelling heat of flow in magneto-optic multilayered media," Ph.D. dissertation, University of Keele, 1994.

[3.8] T. Smy, D. Walkey, and S. Dew, "Transient 3D heat flow analysis for integrated circuit devices using the transmission line matrix method on a quad tree mesh," *Solid-State Electronics*, vol. 45, no. 7, pp. 1137–1148, 2001.

[3.9] A. Amri, A. Saidane, and S. Pulko, "Thermal analysis of a three-dimensional breast model with embedded tumour using the transmission line matrix (TLM) method." *Computers in Biology and Medicine*, vol. 41, no. 2, pp. 76–86, 2011.

[3.10] J. H. Lienharad IV and J. H. Lienharad V, *A heat transfer textbook*, 3rd ed. Massachusetts,USA: Phlogiston Press, 2008.

[3.11] J. Fourier, *The analytical theory of heat*. London: Cambridge University Press, 1878.

[3.12] A. Gurses and M. Ejder-Korucu, *Thermodynamics - Fundamentals and Its Application in Science*, R. Morales-Rodriguez, Ed. InTech, 2012. [Online]. Available: http://www.intechopen.com/books/thermodynamics-fundamentals-and-its-application-in-science/a-view-from-the-conservation-of-energy-to-chemical-thermodynamic

[3.13] P. B. Johns, "A simple explicit and unconditionally stable numerical routine for the solution of the diffusion equation," *International Journal for Numerical Methods in Engineering*, vol. 11, no. 8, pp. 1307–1328, 1977.

[3.14] C. Christopoulos, *The Transmission-Line Modeling Method TLM.* Piscataway,NJ: IEEE Press, 1995.

[3.15] D. De Cogan, *Transmission Line Matrix (TLM) techniques for diffusion applications.* Amesterdam, The Netherlands: Gordon and Breach Science Publishers, 1998.

[3.16] D. De Cogan and A. De Cogan, *Applied numerical modelling for engineers.* Oxford: Oxford Univeristy Press, 1997.

[3.17] A. Elkalsh, A. Vukovic, P. D. Sewell, and T. M. Benson, "Electro-thermal modelling for plasmonic structures in the TLM method," *Optical and Quantum Electronics*, vol. 48, no. 4, p. 263, 2016.

[3.18] A. Elkalsh, A. Vukovic, P. Sewell, and T. M. Benson, "Coupled arc discharge models in the TLM method," in *2015 IEEE International Symposium on Electromagnetic Compatibility (EMC).* IEEE, 2015, pp. 987–990.

4

Plasma modelling and coupled model

This chapter introduces plasma as a frequency dependent material in the electromagnetic (EM) transmission line modelling (TLM) method. The condensed node introduced in chapter 2 is further investigated here to model plasma. This chapter further discusses the convergence of the thermal TLM method for different spatial discretisations. These topics provide the necessary background before using the plasma model and different coupling algorithms to couple EM and thermal TLM in chapters 5 and 6, where they are applied to different engineering applications.

* * *

4.1 Plasma

Matter around us usually is in one of the general material states solid, liquid or gaseous. Plasma is considered to be the fourth state of matter which is less common naturally on earth. Plasma is argued to occupy 99.9% of the universe known to us [4.1]. In plasma, there are a large number of electrons that wander freely between the atoms due to the high energy content in the material. This makes plasma

different from other states of matter where electrons move between atoms. The free electrons in plasma that was freed from atoms cause an approximate equal number of ions, defining plasma as a highly ionized material. Plasma has to be electrically neutral with balanced number of negative and positive charges.

Plasma can be created from other states of matter by increasing the material energy level, freeing the electrons by either using heat or an electric field. Under extreme electric field or heat, material becomes highly ionized and qualifies to be plasma that conducts and sustains an electric field due to its lossy dielectric properties. Modelling plasma is crucial for many applications, as will be demonstrated in chapters 5 and 6. Therefore a detailed EM-TLM plasma model implementation is presented here.

4.1.1 Plasma modelling in TLM

Plasma material can be described and modelled using the Drude model which represents plasma as a material with a frequency dependent dielectric constant (permittivity) [4.2]

$$\begin{aligned} \varepsilon(\omega) &= \varepsilon_o \left(1 + \frac{\omega_p^2}{\omega(j\nu_c - \omega)}\right) = \varepsilon_o(1 + \chi_e(\omega)) \\ &= \varepsilon_{re}(\omega) - j\varepsilon_{im}(\omega) \end{aligned} \tag{4.1}$$

where ω_p is the plasma frequency in rad/s, ν_c is the plasma collision frequency, ω is the angular frequency, ε_o is the permittivity of free space, $\chi_e(\omega)$ is the frequency dependent electric susceptibility, ε_{re} is the real part of the plasma permittivity and ε_{im} is the imaginary part of the plasma permittivity. The imaginary part of the permittivity is related to the power loss in the plasma and is highly relevant for the thermal TLM model as will be explained in chapters 5 and 6.

As presented in chapter 2 the nodal voltage and nodal current are obtained from

eq. (2.63) which is repeated here for convenience,

$$\boldsymbol{F} = \begin{bmatrix} V_x & V_y & i_z \end{bmatrix}^T,$$

$$\begin{bmatrix} V_x \\ V_y \\ i_z \end{bmatrix} = \begin{bmatrix} t_{ex} & 0 & 0 \\ 0 & t_{ey} & 0 \\ 0 & 0 & -t_{mz} \end{bmatrix} \cdot \begin{bmatrix} V_x^i \\ V_y^i \\ i_z^i \end{bmatrix} = \boldsymbol{T}\boldsymbol{F}^i \tag{4.2}$$

where $\boldsymbol{T}$ is the transmission coefficient matrix and t_{ex}, t_{ey} and t_{mz} depend on the normalized parameters of the modelled material. These transmission coefficients are generally obtained as presented in chapter 2 from [4.3],

$$\begin{aligned} t_{ex} = t_{ey} &= \frac{2}{2 + g_e + \bar{s}\chi_e}, \\ t_{mz} &= \frac{2}{4 + r_m + 2\bar{s}\chi_m}. \end{aligned} \tag{4.3}$$

Equation (4.3) was introduced in chapter 2 for materials with constant electromagnetic parameters. In plasma, χ_e is a frequency dependent electric susceptibility and is obtained from eq. (4.1) as,

$$\chi_e(\omega) = \frac{\omega_p^2}{\omega(j\nu_c - \omega)}. \tag{4.4}$$

Applying the Laplace transform to eq. (4.4) using $s = j\omega$, the plasma's electric susceptibility in the Laplace domain is obtained from,

$$\chi_e(s) = \frac{\omega_p^2}{s(\nu_c + s)}, \tag{4.5}$$

and therefore the transmission coefficients t_{ex} and t_{ey} are represented in the Laplace domain as,

$$t_{ex} = t_{ey} = \frac{2}{2 + g_e(s) + \bar{s}\chi_e(s)}. \tag{4.6}$$

The numerical implementation of the condensed TLM node transforms eq. (4.2) initially into the discrete frequency domain (z-domain), to be later transformed back into digital time domain using an inverse $Z-$transform. A bilinear transform is used to convert the s-domain(Laplace) to $Z-$domain using ($s = \frac{2}{\Delta t}\frac{1-Z^{-1}}{1+Z^{-1}}$) [4.4].

The equation describing propagation in the x and y directions using the z-domain representation becomes,

$$\frac{V_x}{V_x^i} = \frac{V_y}{V_y^i} = t_{ex} = t_{ey} = \frac{2}{2 + g_e(z) + 2\left(\frac{1-Z^{-1}}{1+Z^{-1}}\right)\chi_e(z)} \tag{4.7}$$

where the electric susceptibility in the z-domain is obtained from

$$\chi_e(z) = \frac{\omega_p^2}{\frac{2}{\Delta t}\left(\frac{1-Z^{-1}}{1+Z^{-1}}\right)\left(\nu_c + \frac{2}{\Delta t}\left(\frac{1-Z^{-1}}{1+Z^{-1}}\right)\right)}. \tag{4.8}$$

The frequency dependent conductivity term is ignored here ($g_e(z) = 0$) as plasma conductivity information is included in the electric susceptibility term. Substituting eq. (4.8) into eq. (4.7), and using algebraic manipulations, eq. (4.7) is reduced to,

$$\frac{V_x}{V_x^i} = \frac{V_y}{V_y^i} = t_{ex} = t_{ey} = \frac{\frac{2\Delta t\nu_c+4}{K_o} + \left(\frac{2\Delta t\nu_c-4}{K_o}\right)Z^{-1}}{1 + \left(\frac{K_o-8}{K_o}\right)Z^{-1}} \tag{4.9}$$

where $K_o = \Delta t(2\nu_c + \omega_p^2\Delta t) + 4$.

Equation (4.9) can be rearranged to be,

$$V_{x,y}[Z] = V_{x,y}^i[Z]\left(\frac{2\Delta t\nu_c + 4}{K_o} + Z^{-1}\left[\frac{2\Delta t\nu_c - 4}{K_o}\right]\right) - V_{x,y}[Z]\left(Z^{-1}\left[\frac{K_o - 8}{K_o}\right]\right), \tag{4.10}$$

which can be represented in a digital filter form as shown in fig. 4.1.

Using the inverse z-transform, eq. (4.10) is transferred to the digital time domain representation as,

$$V_{x,y}[n\Delta t] = \frac{2\Delta t\nu_c + 4}{K_o}V_{x,y}^i[n\Delta t] + \left(\frac{2\Delta t\nu_c - 4}{K_o}\right)V_{x,y}^i[(n-1)\Delta t] - \left(\frac{K_o - 8}{K_o}\right)V_{x,y}[(n-1)\Delta t] \tag{4.11}$$

where $n\Delta t$ represent the current time step, and $(n-1)\Delta t$ represent the previous time step. Equation (4.11) represents the plasma node calculations in a two dimensional (2D) TLM series condensed node. The next section discusses the convergence and implementation issues in the TLM thermal node.

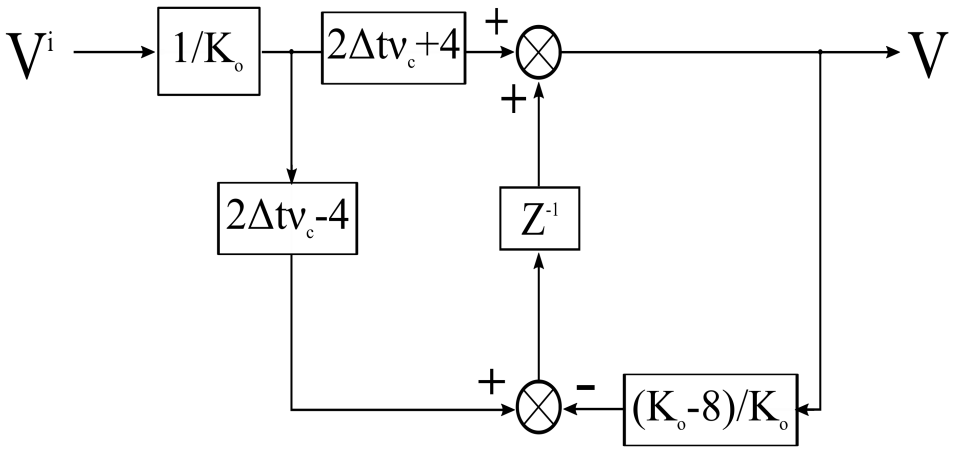

Figure 4.1: Digital filter representation for modelling plasma in a 2D-TLM series node.

4.2 Thermal TLM model convergence

This section highlights the important issues that need to be considered during the implementation of the heat sources in the thermal TLM model. The heat source implementation in the thermal TLM plays an important role in the coupling process between EM and thermal TLM, and maintaining a self-consistent model and converging results. As described in chapter 3, the thermal excitation in the thermal-TLM node can either be represented as a current or a voltage source representing a heat or temperature source respectively. The voltage source (temperature source) is only suitable for cases where knowledge about the structure's temperature is available. The model in this case evaluates only the heat diffusion from the structure with known temperature in the surroundings. On the other hand, the current source (heat source) is more suitable to model the increase in system temperature and the transient response as a result of heat energy input to the structure. The current source for the thermal TLM is more suitable for the modelling of multi-physics applications as heat energy is used as an input to evaluate the system's temperature; hence it was introduced in chapter 3 and the source implementation is further investigated in this chapter.

4.2.1 Scaling of the thermal source

Modelling a two dimensional (2D) problem in electromagnetic (EM) and thermal TLM does not completely ignore the third dimension (depth) in the modelling process. . In thermal TLM, surface area and depth are used to calculate resistance and capacitance as shown in eqs. (3.18) and (3.21). In this thesis for convenience, and to follow the original implementations of the TLM method [4.5], the assumption is made that node dimensions are the same, i.e., $\Delta x = \Delta y = \Delta z = \Delta l$ as presented in chapters 2 and 3.

This section examines the necessary scaling for the thermal sources in the thermal 2D-TLM node as consequence of using different discretisations. This follows the source scaling that was implemented in [4.6] for the 1D sources. A scaling factor for the current source in the thermal node is necessary to ensure that the results converge with respect to the mesh sizes. The scaling process introduced for the thermal source has to consider the source's size and excitation time. This is demonstrated here on the example of a simple 2D-model that represent a material sheet of dimensions $w = 8.2cm$ and $h = 8.2cm$ as presented in fig. 4.2. The source node is placed at the centre of the 2D sheet, as shown, in fig. 4.2 and has dimensions of $w_s = 0.2cm$ and $h_s = 0.2cm$. The boundary conditions are chosen to represent a perfect heat sink i.e. matched boundary conditions. The model describes thermal diffusion in an homogeneous thermal material; therefore the thermal energy diffuses evenly around the source node. Using this feature of modelling a homogeneous material, plotting the thermal profile across the mid y-axis i.e. $y = 4.1cm$ is considered a sufficient representation for the thermal profile.

The thermal properties of the 2D-sheet and the background material were assumed be of as presented in table 4.1 for the purpose of straight forward calculations and easier representation following a similar example from [4.6].

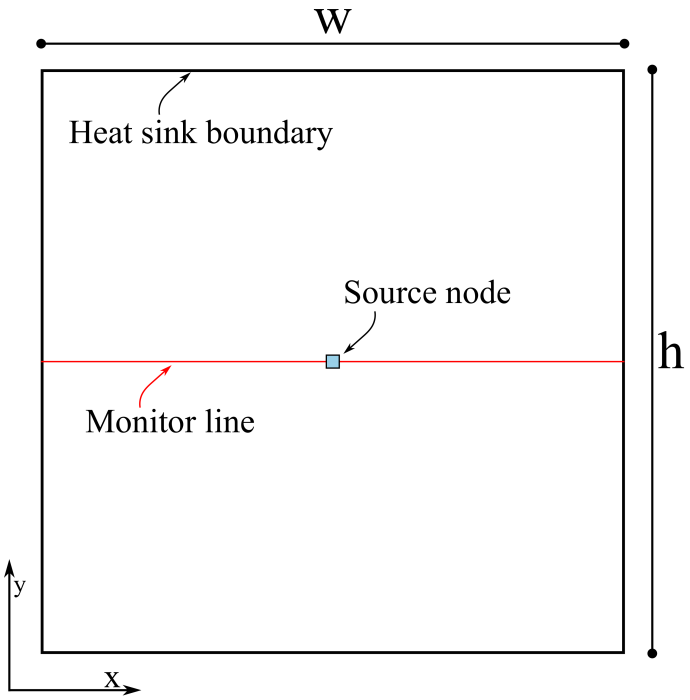

Figure 4.2: A material sheet of dimensions w and h excited by a source node at the centre

Table 4.1: The thermal properties of the materials used in the test case

Material	Specific heat capacity $J.kg^{-1}.K^{-1}$	Thermal conductivity $W.m^{-1}.K^{-1}$	Density $kg.m^{-3}$
Sheet material	2000	0.2	1000
Background	1000	0.5	1000

The model convergence was tested using three different mesh sizes which were chosen for this test case to be $\Delta l = 0.2cm$, $\Delta l = 0.1cm$ and $\Delta l = 0.05cm$. The thermal model time step has to satisfy the stability conditions in eq. (3.28) as demonstrated in chapter 3. It is a commonly accepted practice to chose the time step to be a maximum of one tenth the value of the time constant RC [4.7]. For this particular test case it was chosen to be,

$$\Delta t = 0.05RC \tag{4.12}$$

The thermal time steps evaluated for mesh sizes $\Delta l = 0.2cm$, $\Delta l = 0.1cm$ and $\Delta l = 0.05cm$ are $0.4s$, $0.1s$ and $0.025s$ respectively.

The heat source at the centre was chosen to represent a burst of energy that lasts for a duration of time $T_s = 0.4s$ and to have a value equal to $I_s = 2000$ Watts. It is clear that this choice of heat source leads to, when mesh size $\Delta l = 0.2cm$ is used, a single excited node that lasts for a duration of a single time step. The centre of this source node can not be used as a node centre for finer meshes. Also finer meshes result in a smaller time step, and therefore more time steps are needed to represent the excitation time T_s. The 2D modelling of a thermal problem using different mesh sizes indicates modelling different volumes as well due to the difference in the node depth. The heat source is therefore scaled according to the depth ratio between the different mesh sizes to maintain the overall consistency and convergence. The heat source in this case is scaled to be $\frac{I_s}{n}$ where n is the ratio between the mesh size of the original source and the refined mesh. The duration on the real source is maintained the same, i.e. T_s, but may be spread over multiple model time steps while modelling using fines mesh sizes. The scaling of the current source in this test case at different mesh sizes is illustrated in fig. 4.3 [4.7]

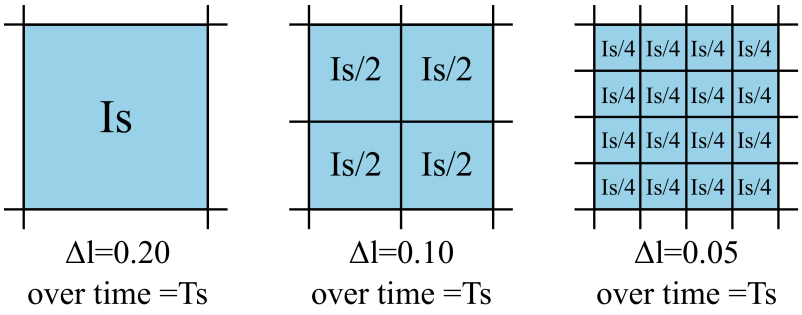

Figure 4.3: The source node representation for the different mesh sizes used in the model

Figure 4.4 compares the temperature profile of the problem in fig. 4.2 at $y = 4.1cm$ using this scaling approach for different mesh sizes. The temperature profile is plotted after a simulated time of 600s. This demonstrates the validity of the current source implementation in the 2D thermal TLM node while using different mesh sizes.

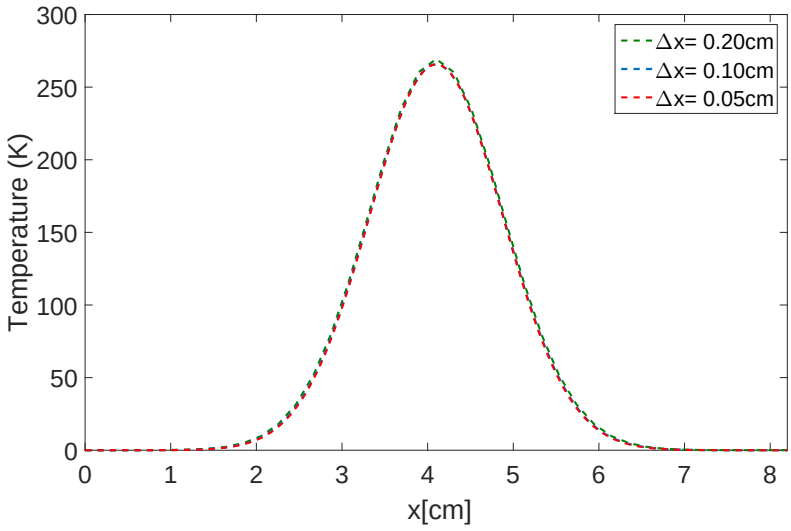

Figure 4.4: The temperature profile at the model centre y=4.2cm for different mesh sizes at time t=600s

The coupling between electrical and thermal TLM model uses the same concept of scaling to guarantee a self-consistent and converging model. The dissipated power in the electromagnetic model is obtained from [4.8],

$$P_d = \frac{1}{2}\sigma_e |E|^2 \quad [Watt/m^3]. \tag{4.13}$$

The dissipated power has to be scaled using the mesh volume before it is used as a heat source for the thermal model.The current source for the thermal model is obtained from the EM model using,

$$I_S = P_d \times \Delta l^3 \quad [Watts]. \tag{4.14}$$

This approach guarantees a converging results and is further investigated for the engineering examples presented in chapters 5 and 6.

4.3 Summary

This chapter highlighted some of the practical issues that need to be considered in the numerical implementation of the electromagnetic (EM) and thermal models. In the first part of the chapter a detailed implementation for the plasma material in the EM-TLM was provided. This was followed by thermal source implementation in the thermal TLM in the second part of this chapter. It also shows the source scaling factor when different discretisation sizes are used, and links it to the coupling between the EM and thermal TLM models. This chapter concludes all the basic theoretical and practical implementations of the EM and thermal TLM models. The following chapters will build upon these basics to model different engineering applications such as nano heat sources and arc discharge phenomenon.

References

[4.1] U. S. Inan and M. Golkowski, *Principles of plasma physics for engineers and scientists*. New York, USA: Cambridge University Press, 2011.

[4.2] R. Luebbers, F. Hunsberger, and K. Kunz, "A frequency-dependent finite-difference time-domain formulation for transient propagation in plasma," *IEEE Transactions on Antennas and Propagation*, vol. 39, no. 1, pp. 29–34, 1991.

[4.3] J. Paul, "Modelling of general electromagentic material properties in TLM," Ph.D. dissertation, Univeristy of Nottingham, 1998.

[4.4] J. Paul, C. Christopoulos, and D. W. P. Thomas, "Generalized material models in TLM Part I : Materials with frequency-dependent properties," vol. 47, no. 10, pp. 1528–1534, 1999.

[4.5] C. Christopoulos, *The Transmission-Line Modeling Method TLM*. Piscataway, NJ: IEEE Press, 1995.

[4.6] D. De Cogan, S. Pulko, and W. O'Connor, *Transmission line matrix (TLM) in computational mechanics*. CRC Press, 2005.

[4.7] D. De Cogan and A. De Cogan, *Applied Numerical Modelling for Engineers*. Oxford: Oxford Univeristy Press, 1997.

[4.8] S. J. Orfanidis, *Electromagnetic Waves and Antennas*, 2014. [Online]. Available: http://www.ece.rutgers.edu/{~}orfanidi/ewa/

5

Plasmonic nano heat sources

In the previous chapters a coupled electromagnetic-thermal model for modelling temperature evolution in a non-linear and dispersive plasma material was introduced. This chapter utilizes the coupled electromagnetic(EM)-thermal model for modelling temperature evolution in nano-size plasmonic heat sources. The stability and accuracy of the coupled EM-thermal model is analysed on an example of a nano-tip plasmonic heat source.

This chapter is organised as follows: in the next section a brief introduction for the modelled cases in this chapter, in section 5.2 the plasma model and a brief description of the EM and thermal model are given, expanding the introduction to the models given in chapters 2 to 4, followed by a description of the coupled EM-thermal algorithm. This is followed by the results on temperature distribution, thermal field convergence and temperature rise for a variety of input mesh sizes and power excitations to demonstrate the convergence and self-consistency of the model. The results are also compared to those calculated and obtained experimentally by [5.19]. In [5.19] the optical simulations were performed using Finite-Difference Time Domain (FDTD) and Finite Element Method (FEM) analyses and the thermal simulations by a FEM approach. Finally some conclusions are given in section 5.4.

5.1 Introduction

Plasmonic waveguides and devices have attracted large attention in the research community in the past decade due to the ability of a metallic-dielectric interface to support surface-plasmon (SP) modes at optical frequencies [5.1]. This is a consequence of the fact that at optical frequencies metals behave as lossy dielectrics and can support SP modes that are highly sensitive to changes in the surrounding medium. Large losses in the metal limit the propagation of SP modes to distances of 10∼100μm [5.2]. The same losses cause heating of the metallic surface and have opened the way for thermoplasmonics i.e., nano-controlled plasmonic heat sources and applications in the areas of thermal photovoltaics [5.3], liquid heating [5.4,5.5], thermal memory [5.6], imaging and spectroscopy [5.7], and medicine [5.8].

The emerging field of thermoplasmonics faces challenges concerning the accurate measurement of the transient temperature variation. A number of experimental approaches have been used to measure the dynamics of metal nanoparticle heating [5.7–5.14]. The numerical modelling of these phenomena has been restricted to either modelling of a purely thermal process using a time-domain diffusion equation [5.9,5.10], or using an electromagnetic-thermal approach whereby the steady state solution of the electromagnetic (EM) field is used as an input excitation to the thermal model [5.9–5.11]. Although in these models the essence of the EM and thermal field evolution is captured, the EM and thermal domain models are essentially decoupled and the material parameters are assumed to be constant. This is schematically shown in fig. 5.1.a, where cumulative power loss of the EM model is used to excite the thermal simulation and where electromagnetic EM and thermal simulations are performed separately, generally using different time steps $\Delta t_{EM} \neq \Delta t_{th}$ for the same real time T_{max}. This is clearly inadequate if temporal sources are considered, and in scenarios where the material parameters are frequency dependent as is the case of a metal at optical frequencies [5.15].

In this chapter a coupled time-domain electromagnetic and thermal method based on the Transmission Line Modelling (TLM) method introduced in chapters 2 and 3 is developed to reflect the multi-physics nature of the optically induced heating process; the method is validated against experimental and numerical results. In the field of Plasmonics, the electromagnetic properties of plasma and a range of plasmonic devices, such as a Surface Plasmon Polariton Waveguide Bragg Grating (SPP-WBG) and a dielectric surface grating for beam focusing applications, have been modelled previously in TLM using the digital filter approach [5.16,5.17].

The multi-physics nature of optical heating is described in this chapter as follows: The electromagnetic TLM model is used to model the electromagnetic scattering of the optical wave in the plasmonic waveguide. The metal at optical frequencies cannot be assumed to be a perfect conductor and is highly lossy, dispersive and frequency dependent. As such the metal is described using the Drude model [5.18] and the $Z-$transform that facilitates the translation between frequency responses of the filter to the time domain of the numerical method. The losses in the metal will give rise to the heating which is used as a heat source when solving the temporal heat diffusion using the thermal TLM model. The coupling process used specifically in this chapter i.e. in the case of nano heat source, is presented in fig. 5.1.b where coupling is done from the EM to thermal models at specified time intervals Δt_{th} and where both EM and thermal simulations are run in parallel. The temporal time step of the EM simulation is fixed but the time step of the thermal simulation can in practice be much larger than that of the EM simulation; in the present model it can be m times larger where m is a positive integer.

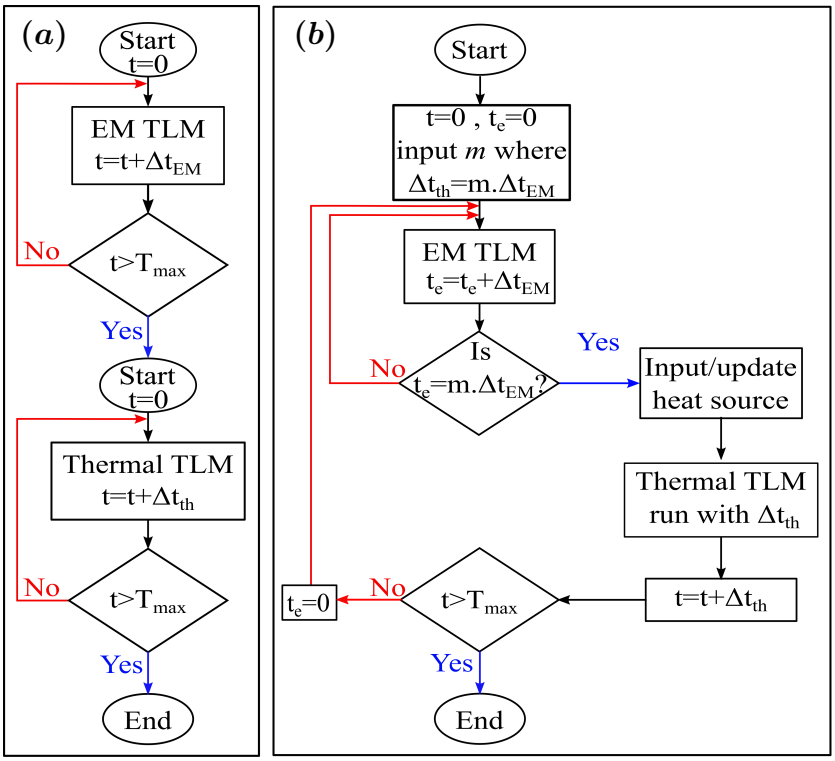

Figure 5.1: The flowchart for (a) decoupled model and (b) coupled model

It is clear that the choice of the coupling interval which determines the thermal time steps would affect the stability, self-consistency and accuracy of the overall coupling method. This is investigated on an example of a plasmonic silicon(Si) waveguide utilizing a tapered nano-tip as a heat source [5.19], as shown in fig. 5.2. The tapered part of the Si waveguide is submerged in gold (Au). The fundamental transverse magnetic (TM) mode, with the electric field polarised in y-direction, is excited in order to activate the plasmon mode at the Si-gold interface. In the TM mode in the 2D TLM sense, the magnetic field (H) is in the out of page direction and is implemented using the series node. The strong confinement of the EM field at the waveguide tip will result in high Ohmic losses and heating of the Au around the waveguide tip.

This chapter is organised as follows: in the next section the plasma model and a brief description of the EM and thermal model are given, expanding the introduc-

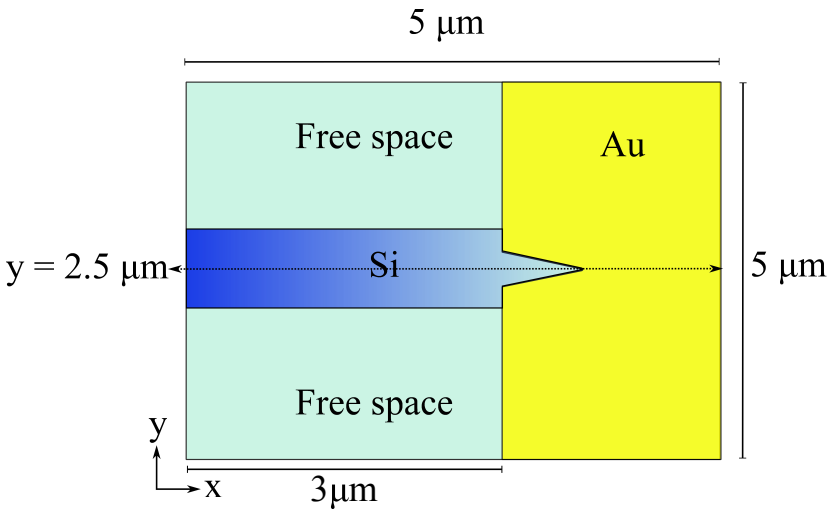

Figure 5.2: The 2D Geometry of the plasmonic waveguide with the nanotip surrounded by gold

tion to the models given in chapters 2 to 4, followed by a description of the coupled EM-thermal algorithm. This is followed by the results on temperature distribution, thermal field convergence and temperature rise for a variety of input mesh sizes and power excitations to demonstrate the convergence and self-consistency of the model. The results are also compared to those calculated and obtained experimentally by [5.19]. In [5.19] the optical simulations were performed using Finite-Difference Time Domain (FDTD) and Finite Element Method (FEM) analyses and the thermal simulations by a FEM approach. Finally some conclusions are given in section 5.4.

5.2 The Electromagnetic (EM) model

In order to simulate the propagation of the fundamental TM optical mode, the series TLM node is used to allow for a magnetic field component along the (out of page) direction H_z and electric fields components E_x and E_y. The silicon is modelled in the TLM node as a material with a constant permittivity and constant electric

susceptibility substituted in eq. (2.64). Gold on the other hand is a metal that has the properties of a lossy dielectric at optical frequencies; its dielectric properties are described using the Drude model [5.20]

$$\begin{aligned}\varepsilon(\omega) &= \varepsilon_o\left(1+\frac{\omega_p^2}{\omega(j\nu_c-\omega)}\right) = \varepsilon_o(1+\chi_e(\omega)) \\ &= \varepsilon_{re}(\omega) - j\varepsilon_{im}(\omega)\end{aligned} \tag{5.1}$$

where $\varepsilon_o(\omega)$ is the frequency dependent permittivity, ω_p the plasma frequency in rad/s, ν_c is the collision frequency, ε_o is the permittivity of free space, ω is the angular frequency,$\chi(\omega)$ is the frequency dependent electric susceptibility, and $\varepsilon_{im}(\omega)$ and $\varepsilon_{re}(\omega)$ are the imaginary and real components of the plasma permittivity respectively. The complex dielectric constant is implemented in the TLM method using the Z-transform and digital filter method [5.21] introduced in chapter 2. The material(plasma) behaviour is implemented in the Z-domain TLM method by substituting the frequency dependent susceptibility in eq. (2.64) as implemented in section 4.1.

The imaginary part of the complex dielectric index represents the material conductivity component that is responsible for the power dissipation in the metal. The heat source of the thermal model is obtained from the instantaneous power losses in the EM model as a consequence of the material conductivity. At optical frequencies the conductivity of a plasmonic material is approximated to be [5.15],

$$\sigma_e = \frac{\omega_p^2}{4\pi\nu_c} \tag{5.2}$$

where $\sigma_e$is electrical conductivity in S/m. The instantaneous power loss at every TLM node can be obtained using the general formula for dissipated power density [5.22]

$$P_d[n] = \frac{1}{2}\sigma_e\left|\overline{\mathbf{E}}[n]\right|^2 \tag{5.3}$$

where n represents the node, P_d is the power dissipated per unit volume at the node in W/m^3 and $\overline{\mathbf{E}}$ is the electric field in V/m at each node, obtained as $\overline{\mathbf{E}} =$

$\sqrt{E_x^2 + E_y^2}$.

The value of the current source at each thermal node is obtained at coupling intervals using eq. (5.3), where the mapping from power to current is given by

$$I_s = P_d[n] \times \Delta l A \tag{5.4}$$

where A is the nodal area.

The thermal node used for this model was introduced earlier in section 3.4 and is illustrated in fig. 3.5. The thermal parameters of the materials used in the model are those for an ambient temperature of 25^oC. The outer boundary conditions for the thermal model are modelled as a heat sink at ambient temperature. The principal difficulty in coupling the EM and thermal TLM models lies in the fact that the simulation time steps of the EM and thermal models are different. The simulation time step of the thermal model defines its stability and needs to satisfy [5.23]

$$\Delta t_{th} \ll R_{th} C_{th} \tag{5.5}$$

where R_{th} and C_{th} the thermal resistance and thermal capacitance that give the lowest thermal product $R_{th}C_{th}$ in the thermal model.

Typically, the time step of the thermal model that satisfies eq. (5.5) is many orders of magnitude higher than the time step of the EM model, which means that that the overall timescales of EM and thermal models are different. The choice of thermal time step is thus important for stable coupling between the EM and thermal models. Generally setting the thermal time step to be equal to the electrical time step will guarantee the stability of the thermal model due to the fact that thermal diffusion is much slower than the interaction of the EM waves. However, this choice would increase the computational resources of the model. It would be desirable to increase the thermal time step and coupling intervals so that both the accuracy and the stability of the method are ensured and both EM and thermal simulations are effectively running in parallel over the same time frame as shown in fig. 5.1.b. In

the following section the choice of the thermal time step is discussed in terms of the accuracy and stability of the coupled method.

5.3 EM-thermal results and convergence of the model

In this section the coupled EM-thermal model is used to simulate the EM field propagation and conduction heat diffusion for the 2D nanotip waveguide structure shown in fig. 5.2. The silicon slab waveguide has an assumed width of 1 μm and a length of 3 μm. The triangular tapered area has a base width of 0.45 μm and a length of 1μm with the nanotip of 20 nm diameter to focus the light at the end of the waveguide. The silicon waveguide core, of refractive index n_m =3.477 [5.24], has a depth (z-direction) of 450nm and an effective refractive index of n_{ef} =3.3917 at the operating wavelength of 1.55 μm, and excites the fundamental TM mode, and the air as the outer cladding material. The material parameters for gold are plasma frequency $\omega_p = 1.36734 \times 10^{16} rad.s^{-1}$ and collision frequency $\nu_c = 6.46 \times 10^{13} Hz$ [5.15]. The silicon is considered to be lossless in this model. All EM material parameters are kept constant in the model.

The material properties for the gold, air and silicon used in the thermal model are the specific heat capacity, density and thermal resistance at the ambient temperature of 25^oC; these are summarised in table 5.1 [5.25,5.26]. The background material is an artificial material with assumed thermal parameters so that it will have a lower diffusion constant than all the other materials used in the model in order to satisfy the stability condition in eq. (5.5) [5.23].

Table 5.1: Material properties used in the thermal model

Material	Properties of the materials used in the thermal model		
	Specific heat capacity $J.kg^{-1}.K^{-1}$	Thermal conductivity $W.m^{-1}.K^{-1}$	Density $kg.m^{-3}$
Gold(Au)	129	317	19320
Air	1005	0.0262	1.2928
Silicon(Si)	710	148	2330
Background	250	0.0262	1.2928

5.3.1 Excitation signal setup

The fundamental TM mode was excited at the operating wavelength of λ =1.55 μm and when cladding and substrate materials were of air with refractive index $n_c = 1$. The H_z field component was excited in the TLM for the waveguide slab as presented in this chapter, and is obtained from [5.22,5.27]

$$H_z = \begin{cases} A_{mp}\cos(K_n d_0) \times \exp(-\gamma_c(y - d_0)) & y > d_0 \\ A_{mp}\cos(K_n y) & |y| < d_0 \\ A_{mp}\cos(K_n d_0) \times \exp(\gamma_c(y + d_0)) & y < -d_0 \end{cases} \tag{5.6}$$

where $K_n = \frac{2\pi}{\lambda}\sqrt{n_m^2 - n_{eff}^2}$, $d_0 = 0.5\mu m$ is the half width of the waveguide, A_{mp} is the field amplitude and $\gamma_c = \frac{2\pi}{\lambda}\sqrt{n_{eff}^2 - n_c^2}$. The excitation signal satisfies the continuity of the magnetic field at the waveguide boundaries as shown in fig. 5.3. Note that the propagation direction is assumed to be the x-direction. The signal was then time modulated by a sinusoidal signal to excite the fundamental mode at the operating wavelength λ of $1.55\mu m$.

In the slab waveguide represented in this chapter the electic field component in the y-direction can be obtained from the magnetic field component H_z using [5.22]

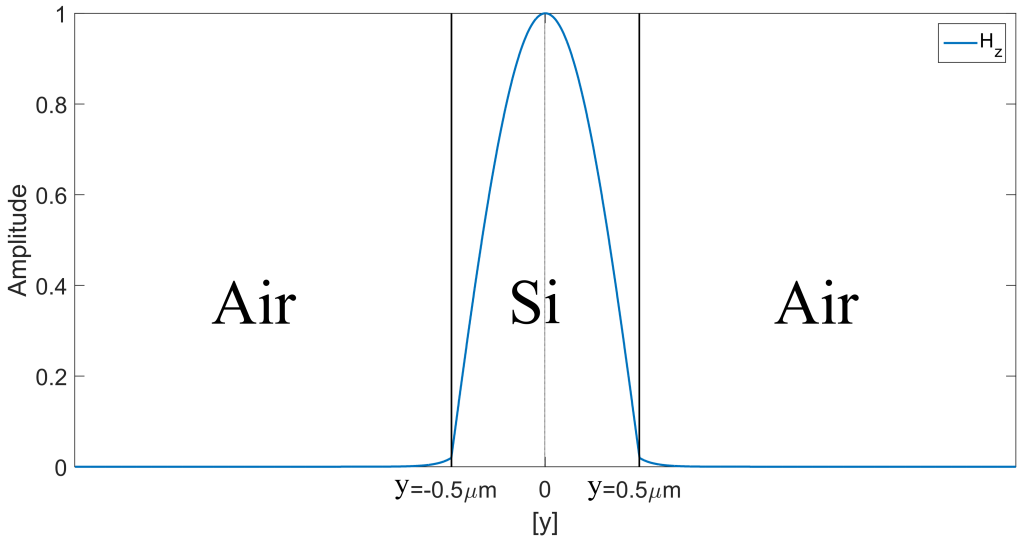

Figure 5.3: Field profile of the E_y field component at the steady state

,

$$E_y = \begin{cases} \frac{\beta\lambda}{2\pi c\varepsilon_0 n_c^2} H_z = \frac{n_{eff}}{c\varepsilon_0 n_c^2} H_z & y > d_0 \\ \frac{n_{eff}}{c\varepsilon_0 n_m^2} H_z & |y| < d_0 \\ \frac{n_{eff}}{c\varepsilon_0 n_c^2} H_z & y < -d_0 \end{cases} \tag{5.7}$$

where $\beta = n_{eff}\frac{2\pi}{\lambda}$ is the propagation constant, c is the speed of propagation in free space and ε_0 is the permittivity of free space.

The power inside the wave guide in the direction of propagation (x) is obtained from [5.22]

$$P = \frac{1}{2}|E_y H_z| = \frac{1}{2}\eta|H_z|^2 \tag{5.8}$$

where $\eta = \frac{\beta\lambda}{2\pi c\varepsilon_0 n_m^2}$ is the wave impedance for the TM mode.

The amplitude of the H_z field, for the excitation signal, is then decided by the required amount of power in the waveguide. In the case of 10mW per the waveguide area, the amplitude of the excitation field in the H_z is obtained as

$$\frac{10mW}{A} = \frac{10mW}{1\mu m \times 450nm} = P_x = \eta|A_{mp}|^2 \tag{5.9}$$

5.3.2 Results and discussion

The electromagnetic field distribution of the E_y field component, due to the fundamental TM mode excitation as described in section 5.3.1, is shown in fig. 5.4 for the case when the optical power is 10mW, the mesh size is $\Delta l = 10nm$, the time step is $\Delta t_{EM} = 2.3586 \times 10^{-17}$s and the simulation time is 63.6ps. Figure 5.4 shows that the maximum of the field is at the nano-tip, which will effectively result in large Joule heating in this area.

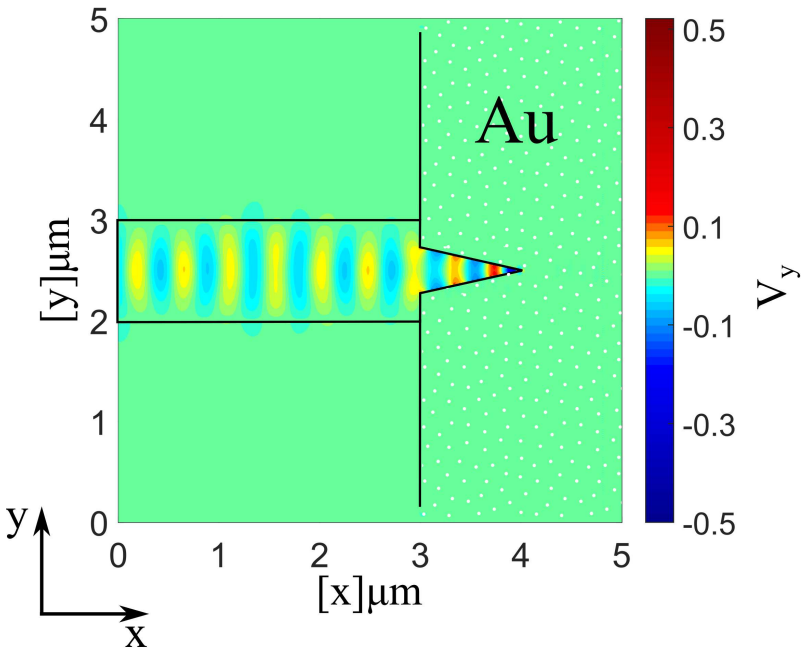

Figure 5.4: Field profile of the E_y field component at the steady state

In order to investigate the convergence of the coupled-method results with the mesh size, Figures 5.5a and 5.5b show the temperature distribution along the middle of the plasmonic waveguide, i.e., in the y=2.5μm plane, for different mesh sizes, namely $\Delta l = 25nm$, $\Delta l = 20nm$ and $\Delta l = 10nm$. The time steps of the EM and thermal models are kept the same as $\Delta t_{EM} = \Delta t_{th} = 2.3586 \times 10^{-17}s$. Two different cases are considered, namely (a) an uncoupled EM-thermal model where a complete EM simulation is done until the field reaches steady state and the power losses at the

end of simulation are used as an input to the thermal model, and (b), where the power losses of the EM model are used as an input to the thermal model at every time step. The input optical source power in both cases is taken to be 10mW.

Figure 5.5a shows that as the mesh size is reduced the temperature distribution converges but the temperature distribution is spread across the waveguide tip. Similarly, in the case of coupling at every time step, fig. 5.5b shows that as the mesh size is reduced the thermal distribution converges. Comparing with fig. 5.5a it can be seen that the thermal profile of fig. 5.5b results in a thermal distribution that is much more focused at the tip of the waveguide, i.e at $x \cong 4\mu m$

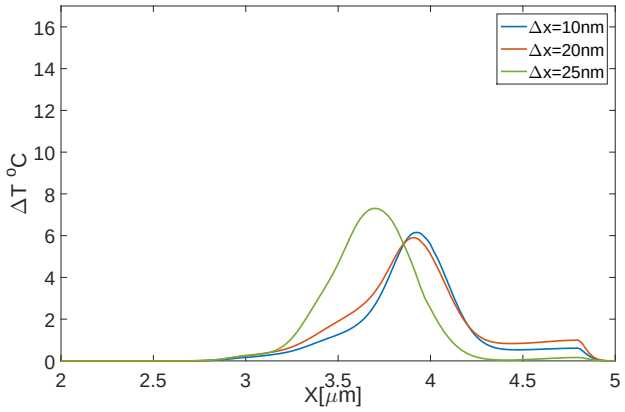

(a)

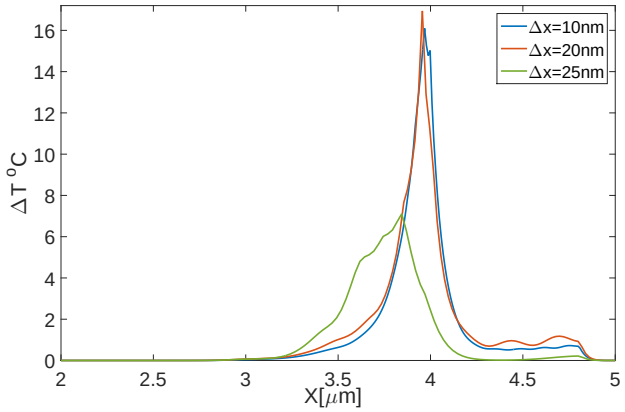

(b)

Figure 5.5: Temperature distribution at y=2.5μm for different mesh sizes for (a) coupling at the end of EM simulation and (b) coupling at every EM time step

Additionally, the maximum temperature achieved at the waveguide tip is much higher in the case of EM-thermal coupling every time step. In both cases the coarse mesh with the discretisation $\Delta x = 25nm$ does not represent the nano-tip thermal profile accurately, resulting in the maximum temperature just before rather than at the tip of the taper itself; this is a consequence of the stair-casing error that is common when discretising planes that do not align with Cartesian coordinates. As the mesh size is reduced the taper profile is modelled more accurately resulting in the simulated maximum field being located at the tip of the taper. As expected Figure 5.5 confirms that the convergence is reached for a mesh size of 20nm or smaller. The results comapare well with expermintal and computational results obtained from [5.19]. Figure 5.6 is the original results from [5.19] and was presented here for comparison purposes only.

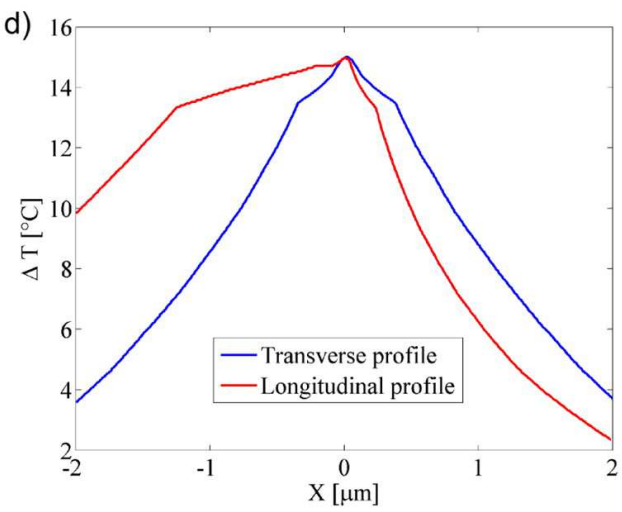

Figure 5.6: The thermal profile at the nanotip and the surrounding area as published in [5.19]

To further investigate the thermal profile, Figure 5.7 plots the thermal field distribution after 82.78 ps of simulation time for (a) the uncoupled and (b) the coupled cases using $\Delta x = 20nm$ and an input optical power of 10mW. The uncoupled model results show a wider spatial spread but lower maximum temperature rise (8^oC) due

to the fact that all the thermal energy is given once at the beginning of the modelling process as shown in fig. 5.7a. Figure 5.7b shows that thermal profile of the coupled EM-thermal model results in a more focused profile with higher maximum temperature compared to fig. 5.7a. In the case of the coupled model the regular application of the input thermal source resulting from the EM simulation leads to higher temperatures and a temperature distribution that is more focused at places where the EM field is strongest, as was shown in fig. 5.5. The result of fig. 5.5b compares very well with the simulations and measurements of [5.19] where the maximum temperature rise is $\sim 15^{o}$C. The small differences might occur due to the fact that a two dimensional model is considered in this chapter while the original computations were obtained in three dimensional.

Results reported in figs. 5.5b and 5.7b assume coupling from the EM model to thermal at every time step and that both thermal and EM time steps are equal. For a mesh size of $\Delta x = 20nm$ the the EM time step is $\Delta t_{EM} = 4.717 \times 10^{-17} s$ and the maximum stable time step for the thermal model is $t_{Th} \approx 1.57 \times 10^{-13} s$. Running the thermal simulation at the EM time step is clearly not computationally efficient. However, the significant difference in the maximum stable time steps allows for the thermal time step to be as small as the EM time step and up to a maximum of $\Delta t_{th}(max)$ determined by equation eq. (5.5) in order to maintain the stability of the thermal model. It is clearly more efficient to run the thermal model at time steps $\Delta t_{th} > \Delta t_{EM}$ whilst still ensuring that the coupling from the EM model to thermal model is done at every Δt_{th}.

Figure 5.8 plots the maximum temperature rise in the model using different thermal time steps such that they are integer multiples of the EM time step Δt_{EM}. The results are shown for $\Delta t_{th}/\Delta t_{EM} = 1, 625, 1350$ and 2500 and are also compared with the uncoupled approach of fig. 5.1.a. Other ratios such as $\Delta t_{th}/\Delta t_{EM} = 2, 50, 125, 250$ and 500 were used as well but they have shown negligible difference

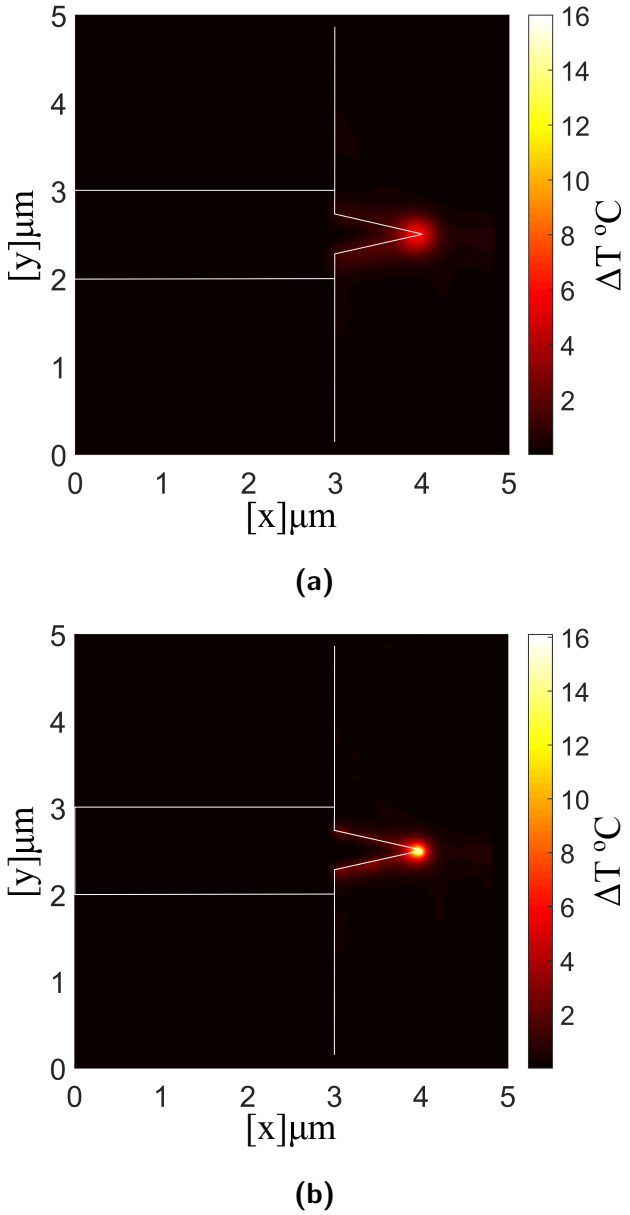

Figure 5.7: The thermal profile for (a) the uncoupled model and (b) coupled model

compared with $\Delta t_{th}/\Delta t_{EM} = 1$. The results of fig. 5.8 show that for a ratio of $\Delta t_{th}/\Delta t_{EM} < 625$ there is no big difference compared to the case when both thermal and EM time steps are the same ($\Delta t_{th}/\Delta t_{EM} = 1$). The uncoupled method does not accurately predict the maximum temperature rise.

The maximum temperature rise within the same time frame will depend on the input power intensity of the optical source. The relationship between the optical

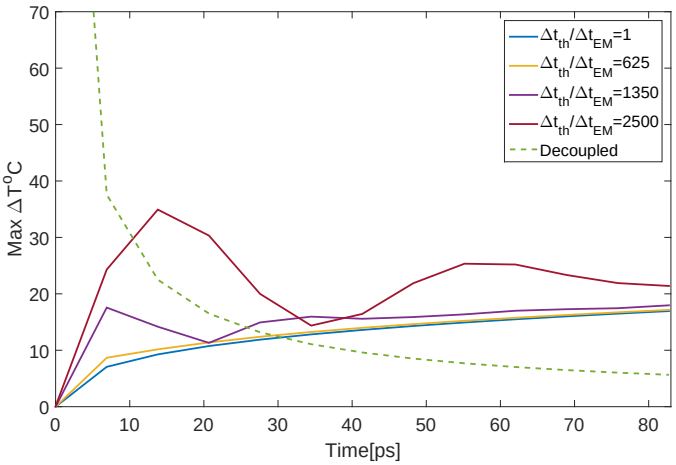

Figure 5.8: Maximum temperature rise as a function of total time simulated using different thermal time steps and compared to results from the decoupled model

source power and the maximum temperature at the same overall simulation time of 82.76ps is plotted in fig. 5.9 for the mesh size $\Delta x = 20nm$. The results are plotted for different thermal time steps namely $\Delta t_{th}/\Delta t_{EM} = 1, 625, 1350$ and 2500 and the EM to thermal coupling is done every thermal time step. Figure 5.9 shows that in all cases the maximum temperature is linearly dependent on the input optical power which compares well with the experimental results of [5.19]. It also shows that when the time step ratio $(\Delta t_{th}/\Delta t_{EM})$is equal to 625, the results are almost identical to the case when $\Delta t_{th}/\Delta t_{EM} = 1$. This allows the thermal model to be run using longer timesteps to save computational power and time, whilst maintaining accurate results.

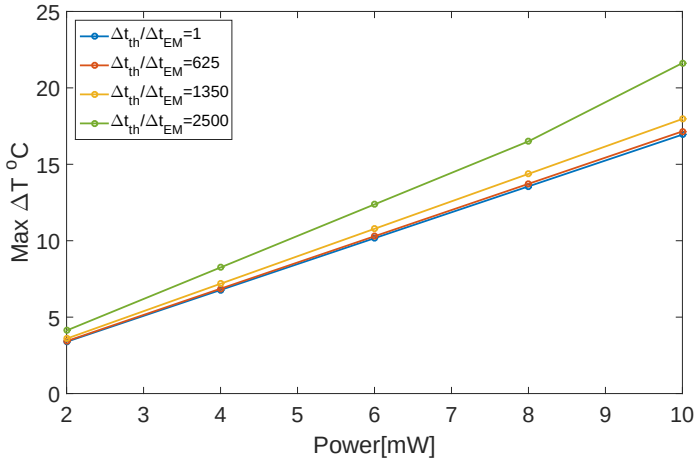

Figure 5.9: Maximum temperature rise as a function of source power at the same simulated time (82.76ps) calculated using different thermal time steps. The EM model is coupled to the thermal one at every thermal timestep.

5.4 Summary

A stable electromagnetic (EM) -thermal multi-physics coupled model of EM-induced heating in a plasmonic tapered waveguide is demonstrated. The model calculates the accumulative power loss in the EM model and uses it as a source for the thermal model at regular time intervals. The results show that regular coupling from the EM model to the thermal method is an important factor to consider, and that this will affect the accuracy of the overall coupling method. The results show that the computational efficiency of the coupled method can be improved if the thermal time step is up to 625 times the EM model time step whilst ensuring that the EM to thermal coupling is done at every thermal time step. The simulated results compare very well with the experimental results of [5.19]. The linear relation between the optical source power and the maximum temperature rise is also verified and compares well with the experimental results. The presented model in this chapter did not consider the change in the material's EM properties due to the increase in the

material temperature. This assumption was based on the fact that, the overall increase in the model temperature was not significant enough to cause a major alteration in the EM and thermal properties used in the model. The next chapter utilises the electro-thermal coupling technique to model an arc discharge case, where EM properties are strongly dependent on the thermal profile of the materials. The next chapter uses the fully coupled approach where the thermal model is used to update the EM properties of the materials.

References

[5.1] J. a. Schuller, E. S. Barnard, W. Cai, Y. C. Jun, J. S. White, and M. L. Brongersma, "Plasmonics for extreme light concentration and manipulation." *Nature materials*, vol. 9, no. 3, pp. 193–204, 2010.

[5.2] H. M. G. Wassel, D. Dai, M. Tiwari, J. K. Valamehr, L. Theogarajan, J. Dionne, F. T. Chong, and T. Sherwood, "Opportunities and Challenges of Using Plasmonic Components in Nanophotonic Architectures," *IEEE Journal on Emerging and Selected Topics in Circuits and Systems*, vol. 2, no. 2, pp. 154–168, 2012.

[5.3] H. A. Atwater and A. Polman, "Plasmonics for improved photovoltaic devices," *Nature Materials*, vol. 9, no. 10, pp. 865–865, 2010.

[5.4] Z. Fang, Y. R. Zhen, O. Neumann, A. Polman, F. J. García De Abajo, P. Nordlander, and N. J. Halas, "Evolution of light-induced vapor generation at a liquid-immersed metallic nanoparticle," *Nano Letters*, vol. 13, no. 4, pp. 1736–1742, 2013.

[5.5] G. L. Liu, J. Kim, Y. Lu, and L. P. Lee, "Optofluidic control using photother-

mal nanoparticles." *Nature materials*, vol. 5, no. 1, pp. 27–32, 2006.

[5.6] L. Wang and B. Li, "Thermal memory: A storage of phononic information," *Physical Review Letters*, vol. 101, no. 26, pp. 1–4, 2008.

[5.7] D. Boyer, P. Tamarat, A. Maali, B. Lounis, and M. Orrit, "Photothermal imaging of nanometer-sized metal particles among scatterers." *Science (New York, N.Y.)*, vol. 297, no. 5584, pp. 1160–1163, 2002.

[5.8] A. M. Gobin, M. H. Lee, N. J. Halas, W. D. James, R. a. Drezek, and J. L. West, "Near-infrared resonant nanoshells for combined optical imaging and photothermal cancer therapy," *Nano Letters*, vol. 7, no. 7, pp. 1929–1934, 2007.

[5.9] G. Baffou, R. Quidant, and F. J. García de Abajo, "Nanoscale control of optical heating in complex plasmonic systems." *ACS nano*, vol. 4, no. 2, pp. 709–16, 2010.

[5.10] G. Baffou, R. Quidant, and C. Girard, "Heat generation in plasmonic nanostructures: Influence of morphology," *Applied Physics Letters*, vol. 94, no. 15, p. 153109, 2009.

[5.11] X. Chen, Y. Chen, M. Yan, and M. Qiu, "Nanosecond photothermal effects in plasmonic nanostructures." *ACS nano*, vol. 6, no. 3, pp. 2550–7, 2012.

[5.12] M. Hu and G. V. Hartland, "Heat dissipation for Au particles in aqueous solution: Relaxation time versus size," *J. Phys. Chem. B*, vol. 106, no. 28, pp. 7029–7033, 2002.

[5.13] A. Plech, V. Kotaidis, S. Grésillon, C. Dahmen, and G. Von Plessen, "Laser-induced heating and melting of gold nanoparticles studied by time-resolved x-ray scattering," *Physical Review B - Condensed Matter and Materials Physics*, vol. 70, no. 19, pp. 1–7, 2004.

[5.14] E. Romanova, A. Konyukhov, D. Furniss, A. Seddon, and T. Benson, "Femtosecond laser processing as an advantageous 3-D technology for the fabrication of highly nonlinear chip-scale photonic devices," *Journal of Lightwave Technology*, vol. 27, no. 15, pp. 3275–3282, 2009.

[5.15] M. A. Ordal, R. J. Bell, R. W. Alexander, L. L. Long, and M. R. Querry, "Optical properties of fourteen metals in the infrared and far infrared: Al, Co, Cu, Au, Fe, Pb, Mo, Ni, Pd, Pt, Ag, Ti, V, and W," *Applied Optics*, vol. 24, no. 24, p. 4493, 1985.

[5.16] O. S. Ahmed, M. a. Swillam, M. H. Bakr, and X. Li, "Modeling and design of nano-plasmonic structures using transmission line modeling." *Optics express*, vol. 18, no. 21, pp. 21 784–21 797, 2010.

[5.17] J. Paul, C. Christopoulos, and D. W. P. Thomas, "Generalized material models in TLM Part I : materials with frequency-dependent properties," vol. 47, no. 10, pp. 1528–1534, 1999.

[5.18] S. Ramo, J. R. Whinnery, and T. Van Duzar, *Fields and Waves in Communication Electronics*, 3rd ed. John Wiley & Sons, Inc., 1997.

[5.19] B. Desiatov, I. Goykhman, and U. Levy, "Direct temperature mapping of nanoscale plasmonic devices." *Nano Letters*, vol. 14, no. 2, pp. 648–52, 2014.

[5.20] R. Luebbers, F. Hunsberger, and K. Kunz, "A frequency-dependent finite-difference time-domain formulation for transient propagation in plasma," *IEEE Transactions on Antennas and Propagation*, vol. 39, no. 1, pp. 29–34, 1991.

[5.21] J. Paul, "Modelling of general electromagentic material properties in TLM," Ph.D. dissertation, Univeristy of Nottingham, 1998.

[5.22] S. J. Orfanidis, *Electromagnetic Waves and Antennas*, 2014. [Online].

Available: http://www.ece.rutgers.edu/{~}orfanidi/ewa/

[5.23] D. De Cogan and A. De Cogan, *Applied numerical modelling for engineers*. Oxford Univeristy Press, 1997.

[5.24] C. D. Salzberg and J. J. Villa, "Infrared refractive indexes of silicon germanium and modified selenium glass," *Journal of the Optical Society of America*, vol. 47, no. 3, p. 244, 1957.

[5.25] W. Benenson, J. w. Harris, H. Stocker, and H. Lutz., Eds., *Handbook of Physics*, 1st ed. New York: Springer-Verlag, 2002.

[5.26] R. Min, R. Ji, and L. Yang, "Thermal analysis for fast thermal-response Si waveguide wrapped by SiN," *Frontiers of Optoelectronics*, vol. 5, no. 1, pp. 73–77, 2011.

[5.27] C. A. Balanis, *Advanced Engineering Electromagnetics*. New York, USA: John Wiley & Sons, Inc., 1989.

6

Arc discharge modelling

This chapter presents a fully coupled two-dimensional (2D) multi-physics model for predicting the location of the arc-discharge and lightning channel, and modelling its thermal and electrical behaviour as a highly conductive plasma channel. The model makes no assumptions on the physical location of the lightning channel but predicts its appearance purely from the electromagnetic field conditions. A heat diffusion model is combined with the time-varying nature of the electromagnetic problem where material properties switch from linear air material to a dispersive and non-linear plasma channel. This multi-physics model is checked for self-consistency, stability, accuracy and convergence on a canonical case where an arc-channel is established between two metal electrodes upon exposure to an intensive electric field. The model is then applied to the 2D study of a diverter strip for aircraft lightning protection.

* * *

6.1 Introduction

Arc discharges and lightning have always been an important issue in aircraft safety. Protection against electrical breakdown has been well developed by utilizing the Faraday cage concept that provides a current path away from fuel tanks and the sensitive electrical equipment. In the past decade the interest in carbon fibre composites (CFCs) in aircraft manufacturing has hugely increased due to their high strength-to-weight ratio and low weight [6.1]. Despite their remarkable strength, CFCs are not as conductive as aluminium which makes them susceptible to the lightning strike and secondary electrical breakdown. The accurate modelling and prediction of the lightning strike attachment and arc-discharge is therefore necessary for reliable aircraft prediction.

Arc discharge and lightning are caused by a concentrated electric field that causes an electrical breakdown of an insulator into a highly conductive plasma channel. The arc discharge phenomenon is widely harnessed and used in industrial applications such as welding, metal cutting and operating metal furnaces due to the high thermal energy produced during this process [6.2]. Natural arc-discharge (lightning), causes undesired direct and indirect effects that manifest themselves as thermal and mechanical damage, as well as secondary damage caused by conducting paths. The arc-discharge phenomenon is a challenging multi-physics problem in which electromagnetic (EM)-propagation, chemical reactions, heat conduction, heat convection, mass transfer, and heat radiation interact simultaneously. Plasma that forms in the arc-discharge process is often a thermal plasma that satisfies thermal equilibrium between heavy particles, but is also strongly dependent on pressure [6.3].

Numerical modelling of arc-discharges is a challenging task that requires the simultaneous modelling of electromagnetic fields, the non-linear plasma channel and the thermal effects. Numerical and mathematical models to date have a limited capability in predicting the location or the shape of the arc-discharge channel. In

mathematical models fractals are used to predict the chaotic nature of the lightning branches [6.4,6.5]. In a controlled environment such as welding, the plasma channel is considered to have a parabolic shape between the electrodes and the arc location is limited to a certain area [6.6]. The majority of the modelling work on the discharge and lightning reported to date has focused on the phenomena either from the electrical or thermal point of view or, in the case of industrial applications, on chemical processes and techniques to stabilize the arc discharge process [6.7,6.8]. The lightning channel between a cloud and the earth surface has previously been modelled as a one-dimensional (1D) Transmission Line Model (TLM) where the lightning channel resistance and capacitance are both time varying [6.9]. Plasma as a frequency dependent material is described using the Drude model and implemented in numerical time-domain techniques such as the Finite Difference Time Domain Method (FDTD) [6.10] and the Transmission Line Modelling Method (TLM) [6.11].

Numerical models mainly focus on modelling the direct effects of the lightning where the lightning is modelled as a strong current attached to the material. Most recent papers use the Finite Difference Time Domain (FDTD) method to predict the electric field distribution in CFC panels in the case of lightning strike, where the lightning strike is modelled as a strong current [6.12,6.13]. In [6.13] the current distribution from the FDTD model was used as an input to a Finite Element Analysis (FEA) model to predict the temperature and mechanical damage on CFC panels. Weak coupling between the thermal and EM model was assumed where the electrical parameters of the model do not depend on temperature. In other papers, the lightning was considered as a strong current source applied at the composite panel centre using coupled electro-thermal FEA model to demonstrate the Joule heating [6.14,6.15] involved in lightning strikes on CFCs.

The coupling between EM and thermal model using the numerical TLM method has been previously demonstrated in chapter 5 [6.16] for a simpler model of the nano-plasmonic heat source where plasma is modelled using Drude model and plasma

conductivity is assumed to have constant value at optical frequencies [6.17]. This model assumed constant plasma and collision frequencies and they were not updated due to the fact that induced temperatures (30^oC) were not high enough to significantly change plasma particle concentration, plasma frequency and collision frequency.

In this chapter we extend this coupled EM-thermal model to the modelling of arc-discharge phenomena. The problem considered is similar to the arc-discharges that occur in lightning where a build-up of charge and high electric field causes the breakdown of air. The electrical and thermal TLM methods are coupled through a plasma material model based on the Drude model [6.10]. In this chapter full feedback from the thermal to the electrical model is provided that updates the plasmas electrical parameters with temperature; this is required for the present work as an arc-discharge is highly dependent on both electric field and temperature [6.3,6.18]. A simple test model is set up to reflect the multi-physics nature of the arc discharge and consists of two highly charged aluminium electrodes placed in air as shown in fig. 6.1. A strong EM field is established between them by exciting one electrode with a source having a typical double exponential waveform [6.19] and placing a PEC wall boundary condition on the edges of computational space. The build-up of the EM field between the electrodes causes electrical breakdown of the air when it reaches a critical field value. As a result a plasma channel is established between the electrodes and creates a current path between the electrodes. Due to the high thermal energy of the arc-discharge, the plasma conductivity is assumed to be frequency dependent. In order to include frequency-dependent material parameters in the time domain model, Z-transform and digital filter implementations [6.11] are used as described in chapters 2 and 4.

This model is used to investigate how these three physical processes, namely the EM field, plasma and the thermal diffusion, can be coupled in a stable and rigorous numerical algorithm. Furthermore, the method does not assume any particular

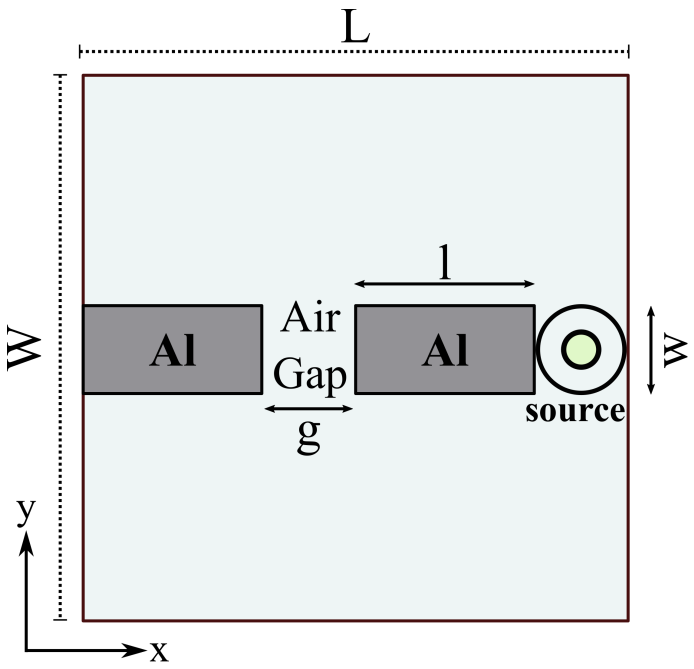

Figure 6.1: The model has two aluminium plates separated by an air gap

physical location for the arc-discharge channel which is entirely dependent on electromagnetic field conditions between the two electrodes. This implies that the model needs to be time-varying (changing material parameters from air to plasma) and nonlinear (modelling plasma). This in consequence raises the issues of stability and power conservation in numerical models which are considered in this thesis. The new multi-physics model is then applied to the illustrative study of a diverter strip for aircraft lightning protection.

This chapter is structured as follows: Section 6.2 outlines the fundamentals of the plasma model. This is followed by a description of the coupled EM-thermal method. Section 6.3 outlines the main results of the chapter and section 6.4 summarizes the main conclusions of the work in this chapter.

6.2 Model

In this section the plasma model and the EM-thermal TLM coupling method are outlined.

6.2.1 The plasma model

The model assumes that in the presence of a strong electric field air breaks down and forms a conducting plasma channel. Plasma material is described using the Drude model as a frequency dependent dielectric constant [6.10]

$$\begin{aligned}\varepsilon(\omega) &= \varepsilon_o\Big(1+\frac{\omega_p^2}{\omega(j\nu_c-\omega)}\Big) = \varepsilon_o\big(1+\chi_e(\omega)\big)\\ &= \varepsilon_o\Big(1+\frac{\sigma_e(\omega)}{-j\omega\varepsilon_o}\Big)\end{aligned} \tag{6.1}$$

where ω_p is the plasma frequency in rad/s, ν_c is the plasma collision frequency, ε_0 is the permittivity of free space, ω is the angular frequency, $\chi_e(\omega)$ is frequency dependent electric susceptibility and $\sigma(\omega)$ is frequency dependent conductivity. The plasma is assumed to be at atmospheric pressure which satisfies thermal equilibrium of heavy particles and electrons. A quasi-neutral plasma model is assumed for which electron and ion densities are nearly equal [6.3]. The plasma model has two main temperature dependent parameters: particle concentration n_e and collision frequency ν_c. The plasma frequency is directly proportional to the square root of the particle concentration and is obtained as [6.20],

$$\omega_p = \sqrt{\frac{n_e q_e^2}{\varepsilon_o m_e}} \tag{6.2}$$

where n_e is the ion concentration in m^{-3}, q_e is the electron charge and m_e is the elec-

tron mass. Collision frequency depends on particle concentration and the thermal energy in the plasma as [6.20],

$$\nu_c = 2.9 \times 10^{-12} \left(\frac{n_e \ln(\Lambda)}{T_e^{3/2}} \right) \tag{6.3}$$

where ν_c is the electron-ion collision frequency, T_{eV} is the temperature in electron volt where $1eV = 11604.3K$ and $(\ln \Lambda)$ is the plasma Coulomb logarithm which is a temperature dependent property and is obtained as, [6.20].

$$\ln(\Lambda) = 23 - \frac{1}{2} \ln \left(\frac{10^{-6} n_e}{T_e^{3/2}} \right) \tag{6.4}$$

The complex permittivity for plasma material in eq. (6.1), is implemented in the TLM method using the Z-transform and digital filter method [6.11]. A detailed description of how the plasma model is implemented in the EM-TLM model is was given in chapter 4 and how the plasma model is implemented in the coupled EM-thermal model is described in section 6.2.2.

6.2.2 Electro-thermal coupling

In this section the coupling algorithm between the EM and thermal TLM model is discussed and the connection between the two domains using the plasma model is described.

There are two principal difficulties in coupling the EM and thermal TLM models. Firstly, the process of switching from a linear material (air) to a nonlinear (plasma) in the time domain requires that the whole process maintains stability and power conservation. Secondly, the time scales, and therefore the simulation time steps of

the EM and thermal models, are very different. The simulation time step of the thermal model needs to satisfy [6.21],

$$\Delta t_{th} \ll R_{th} C_{th} \tag{6.5}$$

where R_{th} C_{th} is the lowest product of thermal resistance and the thermal capacitance in the model. Typically due to the slow nature of thermal diffusion compared to the electromagnetic propagation, the thermal time step is much bigger than the EM time step $\Delta t_{th} \ll \Delta t_{EM}$ given by$\Delta t_{EM} = \Delta l/\sqrt{2}\,c$ where Δl is the node length and c is the speed of light in free space. In the previous chapter on modelling plasmonic nano-heat structures it was shown that the thermal and EM time steps do not have to be the same and that computational resources can be saved by setting thermal time steps to be up to 600 times bigger than the EM time step for the same level of accuracy and without affecting the stability of the coupled method [6.16].

The EM-thermal modelling algorithm is described in fig. 6.2 For simplicity, the algorithm described assumes the same time step, Δt, in both domains although this will be further discussed in the results section 6.3. The EM TLM model is used to start the propagation of the EM field and set the initial parameters of plasma. As will be described in detail in section 6.3 the source signal takes the form of a double exponential; this is typical of lightning source models. Thus, in the initial stages of the simulation the EM field is relatively low and air is modelled as a linear and uniform material. As the electric field in air builds up, all nodes that have electric field greater than some critical value, E_c, undergo breakdown and become plasma. This requires that the material model in selected spatial nodes is instantly switched from a linear air model to a nonlinear and dispersive plasma model.

The plasma model has a significant conductive component that will cause power loss. At each time step the power loss obtained from the plasma EM model be-

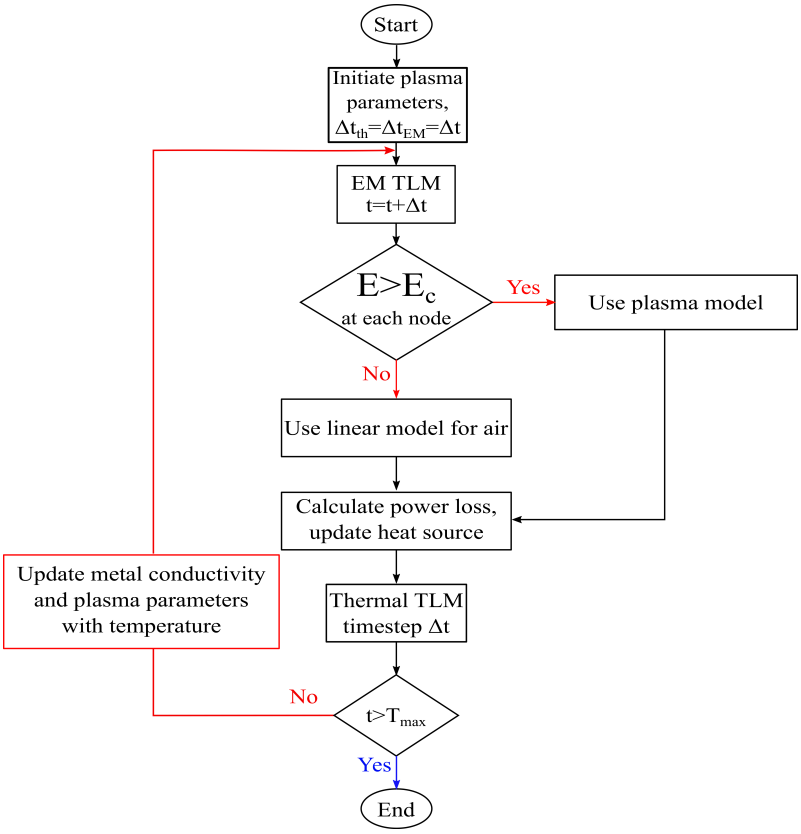

Figure 6.2: The algorithm of the coupling process between electrical and thermal models for the arc discharge

comes the heat source for the thermal model. In a feedback loop the temperature profile from the thermal model is used to update the electromagnetic properties of the plasma (collision frequency,ν_c, plasma frequency, ω_p, and particle concentration n_e) and the conductivity of the metal electrodes. Particle concentration dependence on temperature is extracted from [6.3] for air plasma at atmospheric pressure, using interpolation techniques in order to obtain a continuous curve equation over the entire range of temperature. Using the updated particle concentration and the temperature from the thermal model, collision frequency and plasma frequency are also updated. Similarly, experimental data on the temperature dependent electric conductivity of aluminium was interpolated from [6.22]. Earlier experience of modelling arc discharge updating only the plasma collision frequency was implemented in [6.23]. In this chapter the accuracy and suitability of this approach on the example

of arc discharge is further investigated in the results section 6.3.

At every time step the nodal electric and magnetic fields and dissipated power are updated. As the TLM is a time domain method and plasma parameters are defined in the frequency domain, conversion between these two domains needs to be made at every time step. Also, the connection between the electrical and thermal methods needs to be done through plasma model. The imaginary part of the plasma permittivity represents the material conductivity component that is responsible for the power loss in the EM TLM and acts as a heat source in the thermal TLM. The dissipated power loss is related to electric fields in the Laplace domain as [6.24]

$$P_d(s) = \frac{1}{2}\sigma_e(s)|\overline{E}(s|^2 \tag{6.6}$$

where P_d is the power dissipated per unit volume at a node in W/m^3 and $|\overline{E}|$ is the total electric field in V/m at each node, obtained as $|\overline{E}| = \sqrt{E_x^2 + E_y^2}$.

The frequency dependent conductivity σ_e of the plasma in the Laplace domain $s = j\omega$ is obtained from eq. (6.1) and is

$$\sigma_e(s) = \frac{\omega_p^2 \varepsilon_o}{\nu_c + s} \tag{6.7}$$

Using bilinear transform of ($s = \frac{2}{\Delta t}\frac{1-z^{-1}}{1+z^{-1}}$), plasma conductivity is transformed into $Z-$domain and is then substituted in eq. (6.6). The dissipated power density for plasma in $Z-$domain is thus obtained after some algebraic manipulation as

$$\begin{aligned} P_d[z] &= \frac{1}{2K_o}\sigma_o \Delta t|\overline{E}[z]|^2 + z^{-1}\frac{1}{K_o}\left(\frac{\sigma_o \Delta t}{2}|\overline{E}[z]|^2 - \left(K_o - \frac{4}{\nu_c}\right)P_d[z]\right) \\ &= \alpha|\overline{E}[z]|^2 + z^{-1}\Big(\alpha|\overline{E}[z]|^2 - \beta P_d[z]\Big) \end{aligned} \tag{6.8}$$

where $\sigma_o = \frac{\varepsilon_o \omega_p^2}{\nu_c}$ denotes the DC conductivity of plasma, $K_o = \Delta t - \frac{2}{\nu_c}$, $\alpha = \frac{\sigma_o \Delta t}{2K_o}$

and $\beta = -\left(1 - \frac{4}{K_o \nu_c}\right)$.

The $Z-$domain description of the dissipated power in plasma in a digital filter representation is given fig. 6.3

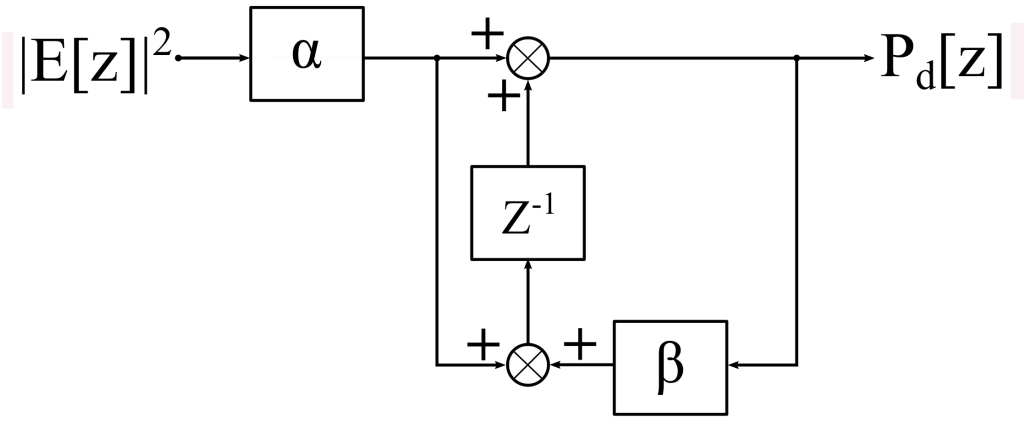

Figure 6.3: The digital filter used to calculate the frequency dependent dissipated power in plasma.

The inverse $Z-$transform is used to translate the dissipated power to the time domain as,

$$P_d[n\Delta t] = \frac{1}{2K_o}\sigma_o \Delta t \left(|\overline{E}[n\Delta t]|^2 + |\overline{E}[(n-1)\Delta t]|^2 \right) - \frac{1}{K_o}\left(K_o - \frac{4}{\nu_c} \right) P_d[(n-1)\Delta t] \tag{6.9}$$

where $n\Delta t$ represent the current time step, and $(n-1)\Delta t$ represent the previous time step. This power is translated to the heat source as in chapter 4 and the updated temperature from the thermal TLM is used to update parameters in the EM TLM method.

6.3 Results

In this section the coupled EM-thermal model is used to simulate the electric breakdown of air and thermal interaction in the structure shown in fig. 6.1. In the absence of direct experimental or modelling data we have used this model to investigate the stability and self-consistency of the method and the convergence of results. The method is then applied to a more general case of diverter strip for lightning strike protection.

The aluminium plates in fig. 6.1 have the length $l = 44mm$ and width $w = 18mm$ and are separated by a $g = 18mm$ air gap. The electrical conductivity of the aluminium plates is taken to be $3.6859 \times 10^7 S/m$ at 25^oC [6.22]. A Perfect Electric Conductor (PEC) boundary condition is placed at the boundaries of the computation space which is of size $W = 108mm$ and $L = 108mm$. The voltage source proportional to E_x field component is placed between one of the aluminium plates and the PEC boundary. The source signal has the form of a double exponential waveform [6.19] typically used to model lightning strike sources and reaches the peak amplitude of $V_c = 20kV/cm$ or $20MV/m$ within $6.5\mu s$ and drops down to half the peak value within the next $70\mu s$ and is obtained in this chapter from [6.19]

$$V = V_c \times (e^{-112001t} - e^{-670000t}) \tag{6.10}$$

When the electric field in air exceeds critical value $E_c = 25kV/cm$ or $25MV/m$ the air breaks-down [6.18] and becomes a highly ionized conductive plasma. The initial temperature of plasma is taken to be 17000 Kelvin (a typical thermal plasma,$\cong$ $1.5eV$) and particle concentration is assumed to be in the range $1 \times 10^{20} < n_e < 1 \times 10^{24} m^{-3}$ [6.3]. The plasma frequency (ω_p), collision frequency (ν_{ei}) and Coulomb logarithm $\ln \Lambda$ are calculated based on these initial conditions. Thermal material properties of aluminium, air and plasma, namely specific heat capacity, density and

thermal conductivity are summarized in table 6.1 [6.25].The background material was chosen to be a material with lower thermal constant (RC) than the plasma as done previously in chapter 5.

Table 6.1: Thermal material properties for aluminium , air and plasma

Material	Properties of the material used in the thermal model		
	Specific heat capacity $J.kg^{-1}.K^{-1}$	Thermal Conductivity $W.m^{-1}.K^{-1}$	Density $kg.m^{-3}$
Aluminium (Al)	897	237	2,707
Air	1,005	0.0262	1.2928
Plasma (at 17000 K)	12,696	3.894	5.57
Background	5,000	3.894	5.57

The results presented in this section compare three ways of coupling between the thermal and EM models. The simplest model assumes no thermal feedback and temperature independent plasma parameters are used throughout the simulation. The second approach follows the approach presented in [6.23] for modelling arc discharge in which only plasma collision frequency is updated. The third approach is the full coupled EM-thermal model that updates all temperature dependent parameters of the plasma namely the collision frequency, plasma frequency and particle concentration.

In order to establish the convergence of the physical location of the plasma channel with the mesh size, the EM-thermal process is first considered with no feedback from the thermal model to the electrical model. The particle concentration is considered to be $n_e = 1 \times 10^{22} m^{-3}$. Figure 6.4(a-c) shows the conducting plasma channel location for the plasma channel for three different spatial discretisations namely, $\Delta l = 3.0mm$, $\Delta l = 1.8mm$ and $\Delta l = 1.5mm$ at the simulation time of $9\mu s$. It can be seen that in the case of coarse discretisation fig. 6.4-a the plasma channel

(or lightning spark) is established almost across the entire gap between the metal plates. Finer meshes (Figure 6.4b-c) show clear separation into two lightning sparks connecting the points with highest field intensity that occur at metal corners due to electric field singularity. Figure 6.4 confirms that finer discretisation provides a better discretisation of the arc-like shape of lightning sparks. Based on these results further calculations presented are based on a mesh size of $\Delta l = 1.8mm$ which is found sufficient to capture and discuss all important features. In all cases, due to the symmetric nature of the model the arcs are also symmetric across the horizontal axis. It is here re-emphasized that model does not assume any particular path for the lightning spark and its appearance is defined solely by the strength of the electric field.

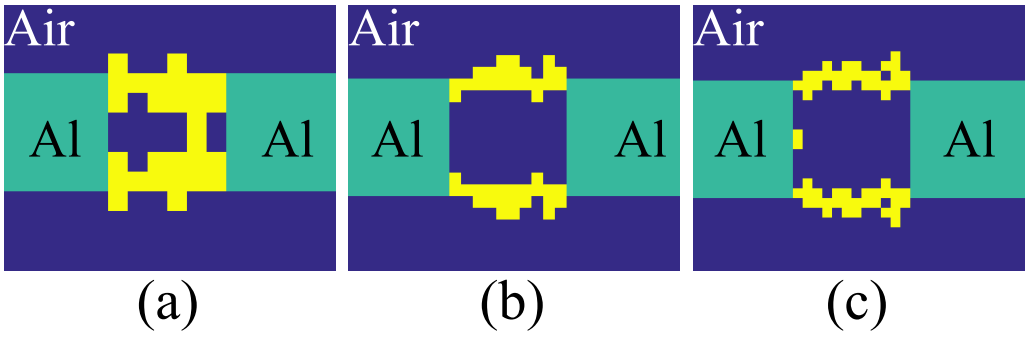

Figure 6.4: Conducting plasma channel between the aluminium plates for a) $\Delta l = 3.0mm$, b) $\Delta l = 1.8mm$ and c) $\Delta l = 1.5mm$ The colour scheme is blue for air, turquoise for aluminium and yellow for plasma.

Figure 6.5 analyses how the initial properties of the plasma affect the lightning spark formation. Figure 6.5(a-c) shows arc formation for three different cases of initial electron density typical of a thermal plasma [6.3] namely $n_e = 1 \times 10^{20}$, $n_e = 1 \times 10^{21}$ and $n_e = 1 \times 10^{23} m^{-3}$. The electron concentration of thermal plasma generally ranges from $n_e = 1 \times 10^{20} m^{-3}$ to $n_e = 1 \times 10^{24} m^{-3}$ In all cases the spatial discretization is taken to be $\Delta l = 1.8mm$ and the details of the plasma channel are again taken at the simulation time of $9\mu s$. In this case only the collision frequency is updated with temperature as in [6.23]. It can be seen that initial conditions for

particle concentration can significantly affect the shape of the arcs implying that this parameter has a strong impact on the shape of plasma channel.

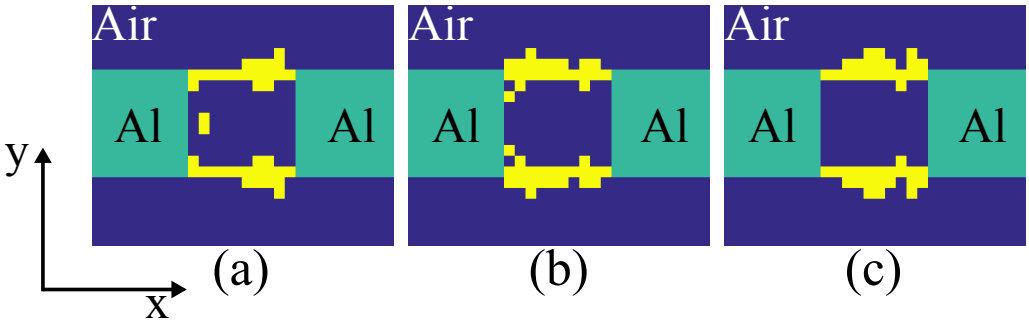

Figure 6.5: Conducting plasma channel between the aluminium plates when using initial electron density a) $n_e = 1 \times 10^{20} m^{-3}$, b) $n_e = 1 \times 10^{21} m^{-3}$ and c) $n_e = 1 \times 10^{23} m^{-3}$ for partially coupled model. The colour scheme is blue for air, turquoise for aluminium and yellow for plasma.

Figure 6.6(a-c) shows the arc channel formations in the case of fully coupled EM-thermal method where all plasma parameters are updated at every timestep. Three different starting conditions for plasma are considered namely $n_e = 1 \times 10^{20}$, $n_e = 1 \times 10^{21}$ and $n_e = 1 \times 10^{23} m^{-3}$. A spatial discretisation of $\Delta l = 1.8mm$ is assumed and the details of the shape of the plasma channel are taken at a simulation time of $9\mu s$. Particle concentration is updated from the experimental data found on page 241 of [6.3] as explained in section 6.2.2, and plasma frequency and collision frequency are updated using eqs. (6.2) to (6.4). Figure 6.6 shows that in all three cases the resulting shape of the arc channel is the same, and it can be said that the arc shape has converged with respect to plasma parameters and temperature.

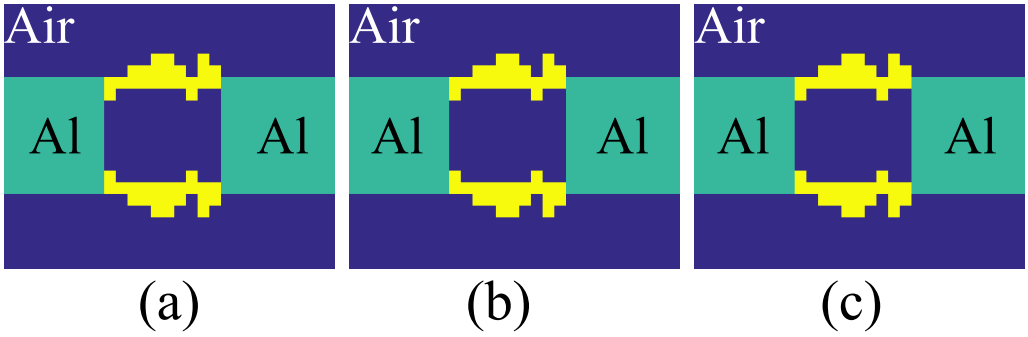

Figure 6.6: Conducting plasma channel between the aluminium plates when using initial electron density a) $n_e = 1e^{20}$, b) $n_e = 1 \times 10^{21}$ and c) $n_e = 1 \times 10^{23} m^{-3}$ for fully coupled model. The colour scheme is blue for air, turquoise for aluminium and yellow for plasma.

Previous results investigate how the shape and position of the lightning channel converge in the model. Figure 6.7 shows the temperature profile for a plasma node at $x = 4.68cm$ and $y = 4.68cm$ for the mesh size $\Delta x = 1.8mm$. The initial electron density was taken to be $n_e = 1 \times 10^{21} m^{-3}$. Figure 6.7 compares temperature in the plasma node when: a) there is weak coupling i.e. no update of plasma parameters with temperature throughout the simulation; b) only collision frequency is updated following the work presented in [6.23] and c) all plasma parameters are updated at every time step. It can be seen that weak coupling of the thermal and EM model predicts much higher temperatures compared to the case when partial or full thermal update of plasma parameters is done. Comparing temperature curves for the partial and full update of plasma parameters it can be noted that in both cases there is a similar prediction for temperature diffusion in plasma, suggesting that both approaches are similar.

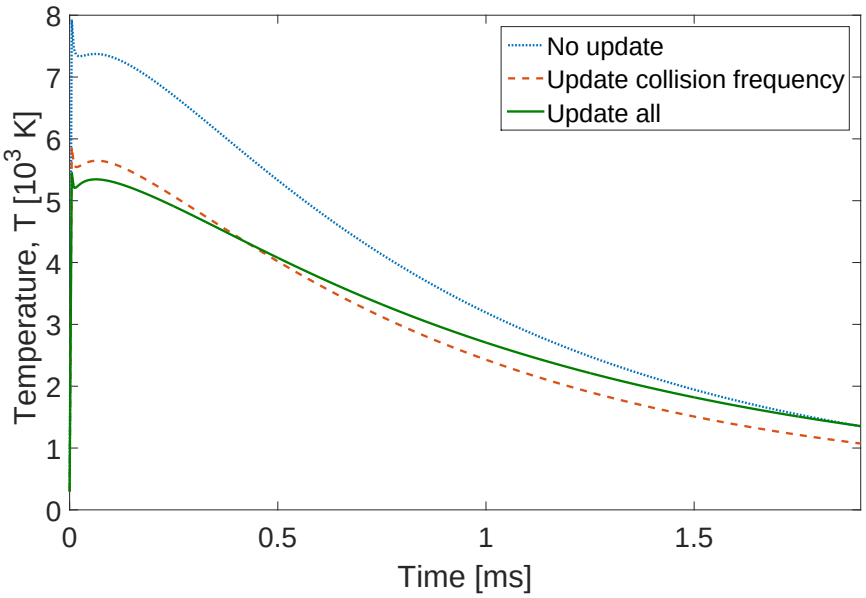

Figure 6.7: The plasma temperature versus time using different coupling methods.

This is further investigated in Figure 6.8 which compares the case of partial coupling where only collision frequency is being updated for several different starting conditions for plasma particle concentrations ($n_e = 1 \times 10^{20}, n_e = 1 \times 10^{21}, n_e = 1 \times 10^{22}, n_e = 1 \times 10^{23}$ and $n_e = 1 \times 10^{24} m^{-3}$). The temporal dependence of temperature is presented for the plasma node at $x = 4.68cm$ and $y = 4.68cm$. Figure 6.8 shows that in the majority of cases the temporal change of temperature follows a similar pattern except for the case of a particle concentration of $n_e = 1 \times 10^{20} m^{-3}$ (inset of fig. 6.8) when the method predicts a very different temperature change compared to the other cases where higher electron densities were used as the initial parameter. Note the $1 \times 10^{12} K$ temperature scale on the inset which is unphysical. This implies that the stability of the partially coupled EM-thermal method is heavily dependent on the initial parameters and establishes that these parameters should thus be updated during the simulation as in the fully coupled thermal-EM algorithm.

In order to show the convergence of the fully coupled EM-thermal model, the tem-

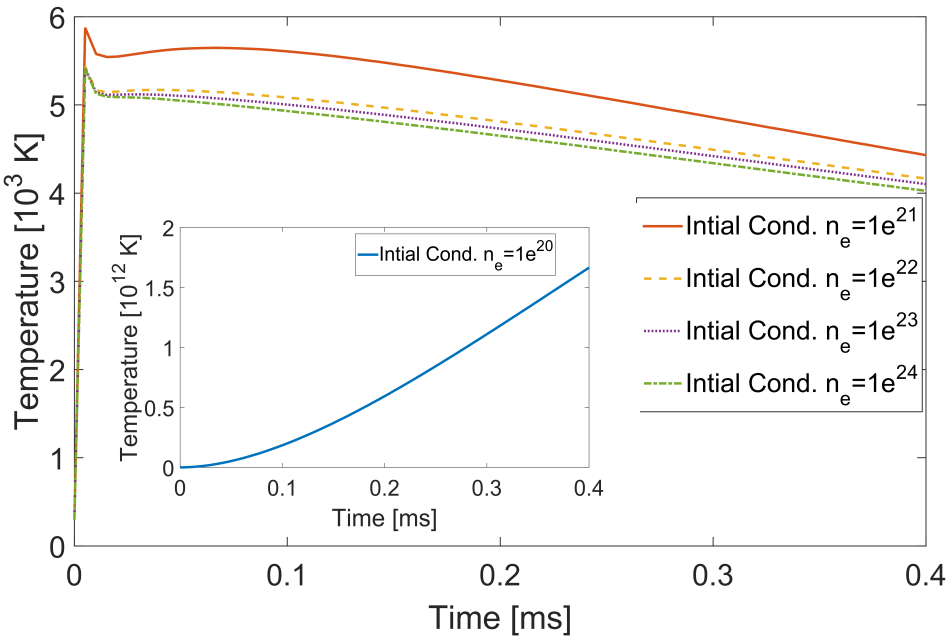

Figure 6.8: Temperature profile for a plasma node at $x = 4.68cm$, $y = 4.68cm$ using different initial electron concentrations and partially coupled EM-thermal model The instability observed for an initial electron concentration at $n_e = 1 \times 10^{20} m^{-3}$ establishes the need for fully coupled thermal-EM model.

perature distribution of the plasma channel across the horizontal plane at $y \cong 4.68cm$ at simulation time $t = 0.51ms$ is plotted in fig. 6.9 for different mesh sizes, namely $\Delta l = 3.0mm$, $1.8mm$ and $1.5mm$ and for an initial electron concentration of $n_e = 1 \times 10^{22} m^{-3}$. The temperature profile is shown here for the arc cases that were previously presented in fig. 6.4. It can be seen that the temperature profile converges as the mesh size decreases and that as mesh size becomes smaller the arc shape becomes more tightly confined. Once again it is seen that a mesh size of $\Delta l = 1.8mm$ is sufficient.

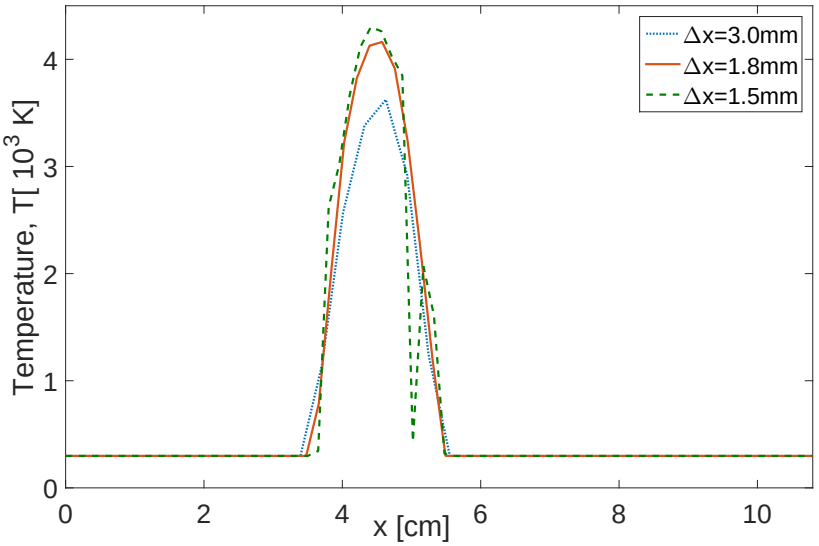

Figure 6.9: Temperature distribution in the plasma region along the horizontal line $y = 4.68cm$

There is an interesting feature in fig. 6.9 in the line representing mesh size $\Delta l = 1.5mm$ which is the apparent sudden drop in temperature profile along the y-axis. The reason for this sudden change is the presence in the discretised model of an air node surrounded by plasma. Power dissipation occurs only in plasma nodes meaning the only way for an air node to gain thermal energy is by heat conduction from surrounding plasma nodes. As plasma is a material with much lower density than air the time needed for heat to diffuse from plasma into a neighbouring air node is much longer than the simulation time presented here. This demonstrates one of the challenges in modelling the multi-physics features of arc-discharge phenomena and the limitation of the model presented in this chapter, as mass transfer and heat convection are important and should be included in the model in order to have a more complete description.

The temperature profiles in (a) the aluminium plate and (b) in the plasma channel, at 12.22ms are plotted in fig. 6.10 using $\Delta l = 1.5mm$. Figure 6.10(a) confirms that the maximum temperature in the aluminium plate is located adjacent to the

plasma channel attachment points and is higher on the side closer to the EM source. Compared to the initial formation of the plasma channel shown in figs. 6.5, 6.6 and 6.8, this fig. 6.10(b) indicates that the temperature in the plasma channel has diffused. Comparing fig. 6.10(a) and (b) it can be seen that plasma temperatures are much higher than the temperatures reached in the metal which is expected as the exposure time to the heat source is short and the mass density of the plasma heat source is low.

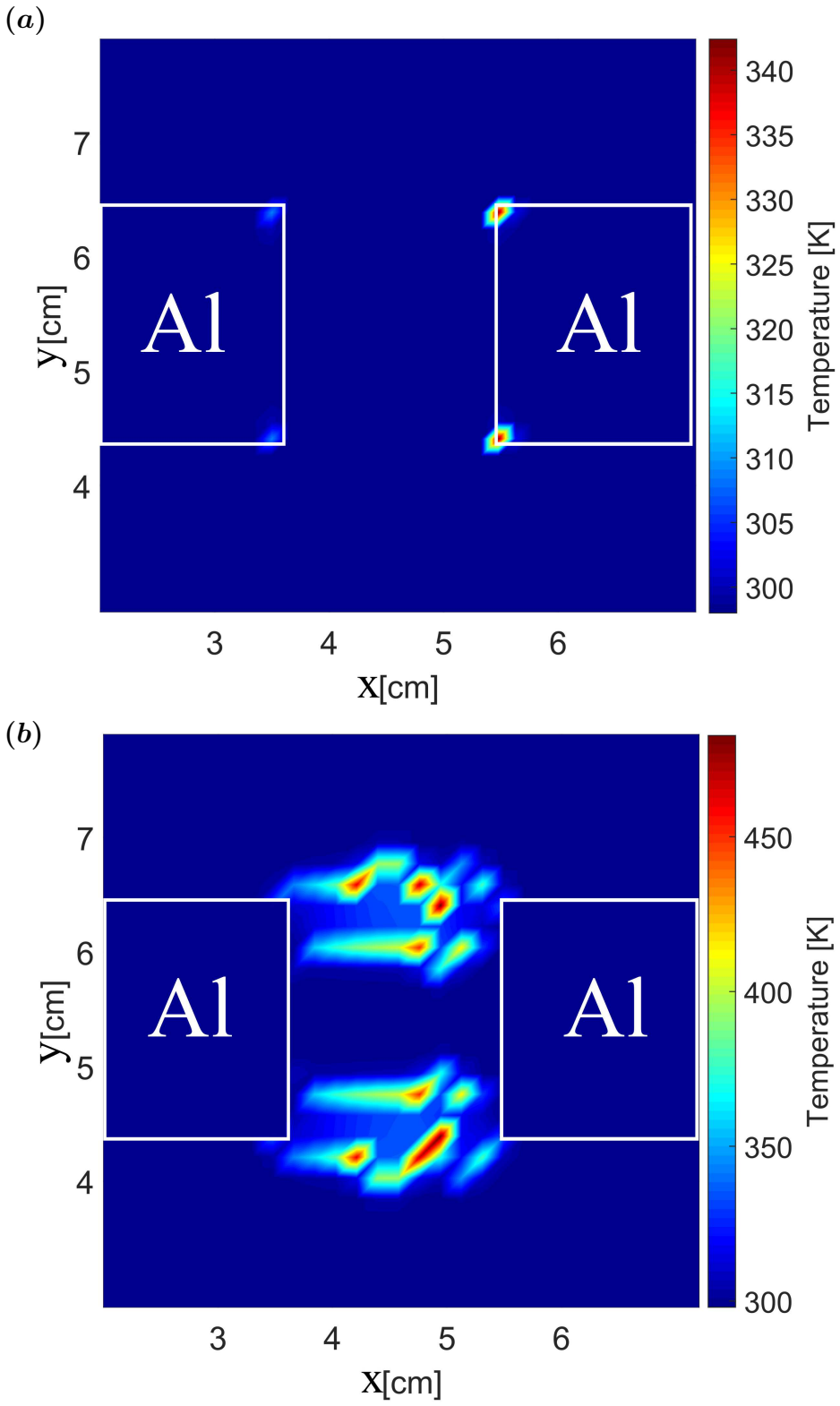

Figure 6.10: The temperature profile in the plasma arc at $12.22ms$, (a) Temperature at metal corners. (b) Temperature at plasma channels.

Results reported in figs. 6.4 to 6.10 assume that the time step is set by the requirement of the EM method and that coupling between the EM and thermal model at every time step. For a mesh size $\Delta l = 1.8mm$ the EM time step is $\Delta t_{EM} = 8.49116ps$ and the maximum stable time step for the thermal model is $t_{th} = 2.942\mu s$. Running the thermal simulation at the EM time step is clearly not computationally efficient. However, the significant difference in the time steps allows for the thermal model to have the time step as small as the EM time step and up to $\Delta t_{th} = 2.942\mu s$. It is clearly more efficient to run the thermal model at time steps $\Delta t_{th} > \Delta t_{EM}$ whilst ensuring that the coupling from the EM to thermal model is done at every Δt_{th}.

Figure 6.11 plots the temperature in a plasma node at $x = 4.68cm$ and $y = 4.68cm$ using different thermal time steps such that they are integer multiples of the EM time step Δt_{EM}. The results are shown for time step ratios of $\Delta t_{th}/\Delta t_{EM} = 1, 2, 5, 10$ and 100. The results show that actual temperature values in the node are of the same order of magnitude as in the case when $\Delta t_{th}/\Delta t_{EM} = 1$ but that, unlike the studies reported in [6.16] and chapter 5, Δt_{EM} and Δt_{th} should remain the same as increasing the ratio adds instabilities to the model which is best explained through fig. 6.12. Figure 6.12 examines the plasma distribution for the case when $\Delta t_{th}/\Delta t_{EM} = 2$ and 5. Comparing with fig. 6.6(c) it can be seen that fig. 6.12(a) as the delay in updating the EM parameters from the thermal model affects the plasma channel formation process. On the other hand fig. 6.12(b) indicates that almost the whole region around the metal plates has turned into plasma. Comparison of the results shown in fig. 6.6(c) and fig. 6.12 confirms that for the accurate plasma location prediction the time steps in both models need to be the same.

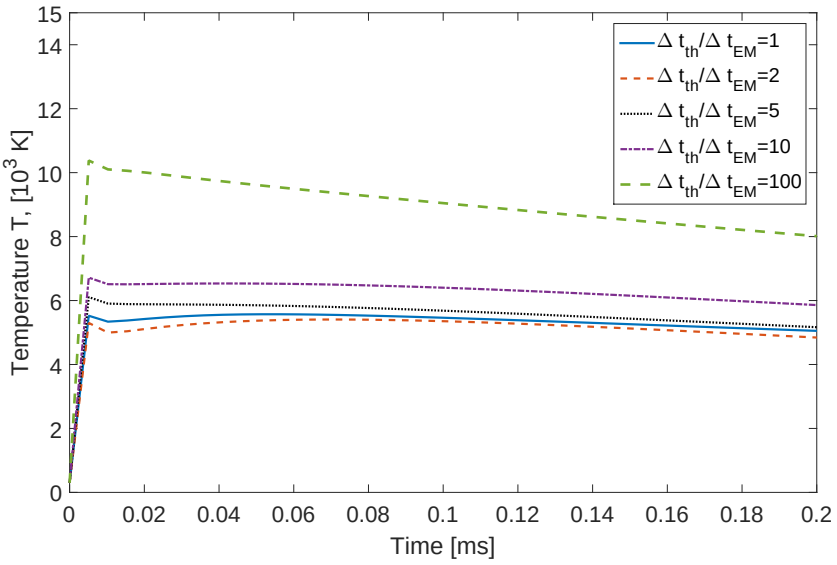

Figure 6.11: Temperature profile for a plasma node at $x = 4.68cm$, $y = 4.68cm$ using different time step ratio between EM and thermal model.

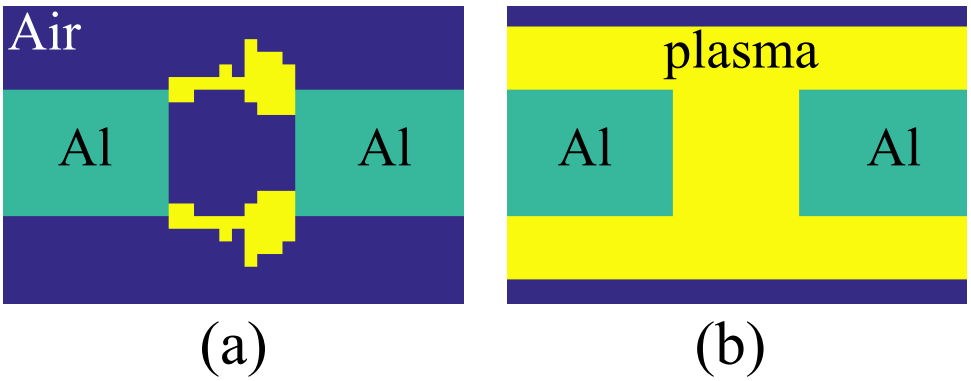

Figure 6.12: Conducting plasma channel between the aluminium plates when using different timestep ratio for EM and thermal model a $\Delta t_{th}/\Delta t_{EM} = 2$; b) $\Delta t_{th}/\Delta t_{EM} = 5$ for the fully coupled model. The colour scheme is blue for air, turquoise for aluminium and yellow for plasma.

After establishing the validity and convergence of the fully coupled EM-thermal TLM model on a simple example it is now applied to model a simplified case of a diverter strip for lightning protection. Diverter strips are installed on places of high likelihood for lightning strike and are used for lightning protection on aircraft

[6.26] A diverter strip consists of an insulator layer on top of which conductive segments (square, diamond, circular) are placed and separated by short air gaps. Once lightning hits a diverter strip, a series of cascaded breakdowns occurs in the gaps between the conductive segments with the purpose of drawing the current away from the sensitive electric instruments. The cascade breakdown exhausts the electric field over a distance and limits the destructive capability of the EM field. The simplified (2D) diverter strips geometry studied is shown in fig. 6.13 and is adopted from [6.26], where the conductive segments are of square shape with a side length of $3.6mm$, gap between the segments is $0.36mm$ and overall problem size is $W = 20.16mm$ and $L = 7.2mm$.

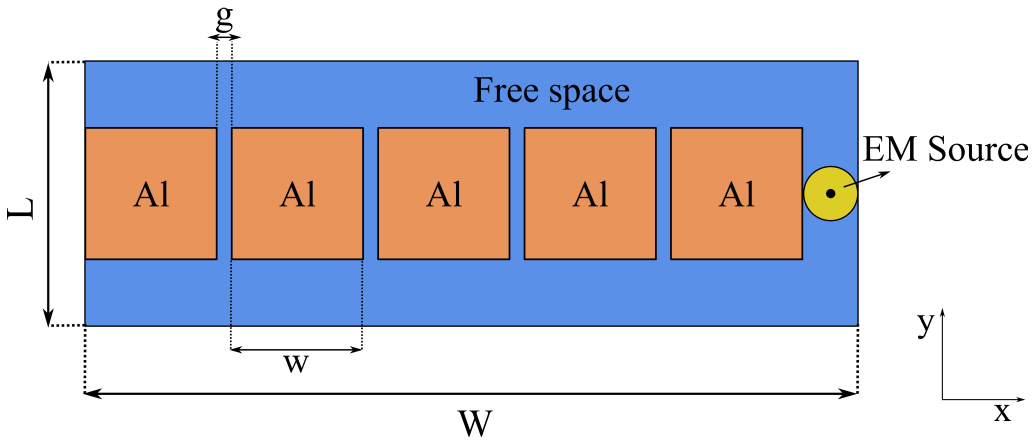

Figure 6.13: Diverter strips structure

Using the similar setup in terms of excitation and boundary conditions as for the air gap model the plasma channel was successively formed between conductive segments and as presented in fig. 6.14. The fully coupled model is used with an initial electron density of $n_e = 1 \times 10^{22} m^3$ and a mesh size of $\Delta l = 0.036mm$. Figure 6.14 shows a cascade of lightning arcs that are formed in corners of the metal plates.

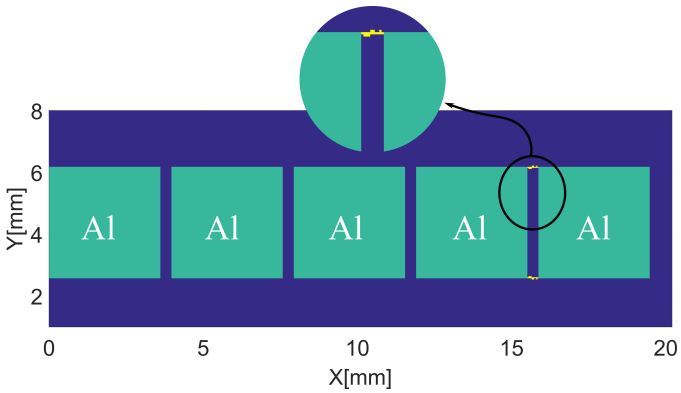

(a) $t = 4.5\mu s$

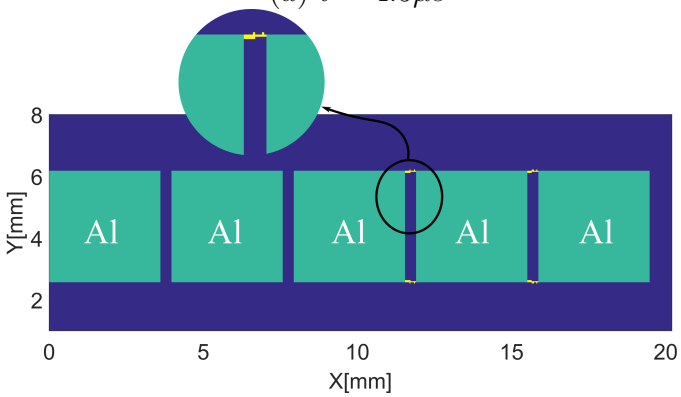

(b) $t = 4.755\mu s$

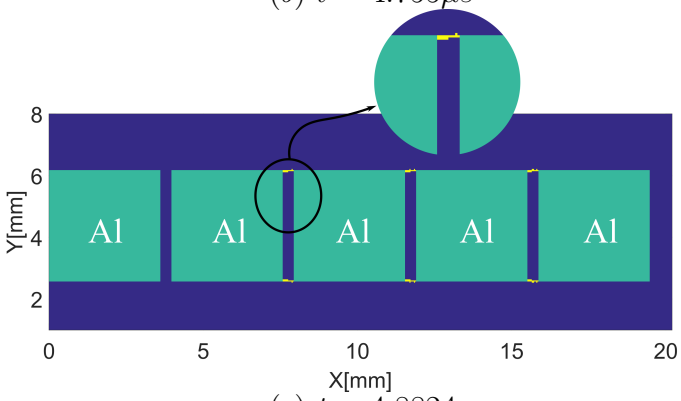

(c) $t = 4.8824\mu s$

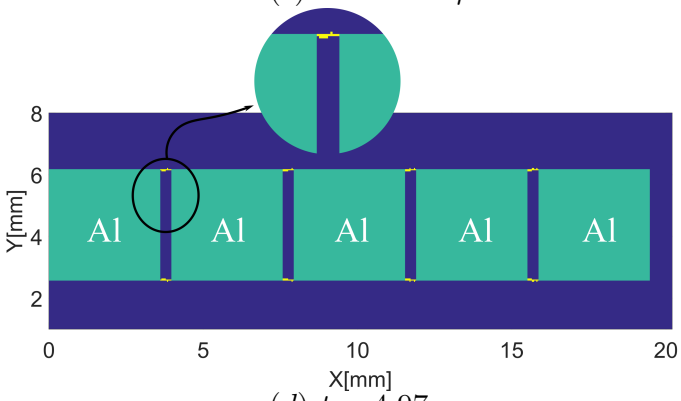

(d) $t = 4.97\mu s$

Figure 6.14: The plasma channel formation in diverter strips using $\Delta x = 0.036mm$

6.4 Summary

A stable electromagnetic EM-thermal multi-physics coupled model for modelling lightning arcs induced by the presence of a strong electric field has been demonstrated. Lightning arcs were modelled as a conductive plasma channel where a frequency dependent Drude model is used for the plasma material model. The model makes no assumptions on the physical location of the lightning channel but predicts its appearance purely from the electromagnetic field conditions. Power loss in the EM model was used as the heat source for the thermal model at regular time intervals. It was shown that stability issues require that the timesteps of both EM and thermal are kept the same. The results show that full thermal feedback from the thermal method to the EM method that updates all plasma parameters with temperature, namely plasma frequency, collision frequency and particle concentrations, is necessary for the convergence of both the shape and temperature of the plasma channel. The method was extended to the example of a diverter strip and it was shown that the lightning path propagates away from the source and connects the points of highest electric field in the model. This concludes the model development and simulation work presented in this thesis. The thesis conclusions and suggestions for future work will be presented in the final chapter.

References

[6.1] P. K. Mallick, *Fiber-reinforced composites: Materials, manufacturing, and design.* CRC press, 2007.

[6.2] H. B. Cary, *Modern welding technology.* Prentice-Hall, 1979.

[6.3] M. I. Boulos, P. Fauchais, and E. Pfender, *Thermal plasmas fundamentals and applications Volume 1.* New York: Plenum press, 1994.

[6.4] L. Niemeyer, L. Pietronero, and H. J. Wiesmann, "Fractal Dimension of Dielectric Breakdown," *Physical Review Letters*, vol. 52, no. 12, pp. 1033–1036, 1984.

[6.5] A. Luque and U. Ebert, "Growing discharge trees with self-consistent charge transport: the collective dynamics of streamers," *New Journal of Physics*, vol. 16, no. 1, p. 013039, 2014.

[6.6] J. Wendelstorf, "Ab initio modelling of thermal plasma gas discharges (electric arcs)," Ph.D. dissertation, Braunschweig University of Technology, 2000.

[6.7] M. S. Benilov, "Understanding and modelling plasmaelectrode interaction in high-pressure arc discharges: A review," *Journal of Physics D: Applied Physics*, vol. 41, no. 14, p. 144001, 2008.

[6.8] M. Tanaka and J. J. Lowke, "Predictions of weld pool profiles using plasma physics," *Journal of Physics D: Applied Physics*, vol. 40, no. 1, pp. R1–R23, 2007.

[6.9] M. Da Frota Mattos and C. Christopoulos, "A nonlinear transmission line model of the lightning return stroke," *IEEE Transactions on Electromagnetic Compatibility*, vol. 30, no. 3, pp. 401–406, 1988.

[6.10] R. Luebbers, F. Hunsberger, and K. Kunz, "A frequency-dependent finite-difference time-domain formulation for transient propagation in plasma," *IEEE Transactions on Antennas and Propagation*, vol. 39, no. 1, pp. 29–34, 1991.

[6.11] J. Paul, "Modelling of general electromagentic material properties in TLM," Ph.D. dissertation, Univeristy of Nottingham, 1998.

[6.12] H. Tsubata, T. Nishi, H. Fujisawa, Y. Baba, and M. Nakagawa, "FDTD simulation of lightning current in a multi-layered CFRP material," in *International*

Conference on Lightning & Static Electricity (ICOLSE 2015). Institution of Engineering and Technology, 2015, pp. 16 (4 .)–16 (4 .).

[6.13] R. Neufeld, "Lightning direct effects on anisotropic materials from electro-thermal simulation," in *International Conference on Lightning & Static Electricity (ICOLSE 2015)*, no. 2. Institution of Engineering and Technology, 2015, pp. 7 (5 .)–7 (5 .).

[6.14] T. Ogasawara, Y. Hirano, and A. Yoshimura, "Coupled thermalelectrical analysis for carbon fiber/epoxy composites exposed to simulated lightning current," *Composites Part A: Applied Science and Manufacturing*, vol. 41, no. 8, pp. 973–981, 2010.

[6.15] G. Abdelal and A. Murphy, "Nonlinear numerical modelling of lightning strike effect on composite panels with temperature dependent material properties," *Composite Structures*, vol. 109, no. 1, pp. 268–278, 2014.

[6.16] A. Elkalsh, A. Vukovic, P. D. Sewell, and T. M. Benson, "Electro-thermal modelling for plasmonic structures in the TLM method," *Optical and Quantum Electronics*, vol. 48, no. 4, p. 263, 2016.

[6.17] M. A. Ordal, R. J. Bell, R. W. Alexander, L. L. Long, and M. R. Querry, "Optical properties of fourteen metals in the infrared and far infrared: Al, Co, Cu, Au, Fe, Pb, Mo, Ni, Pd, Pt, Ag, Ti, V, and W," *Applied Optics*, vol. 24, no. 24, p. 4493, 1985.

[6.18] Vermon Cooray, *The Lightning Flash*, 1st ed., V. Cooray, Ed. The Institution of Engineering and Technology, Michael Faraday House, Six Hills Way, Stevenage SG1 2AY, UK: IET, 2003.

[6.19] W. Jia and Z. Xiaoqing, "Double-exponential expression of lightning current waveforms," in *The 2006 4th Asia-Pacific Conference on Environmental Elec-*

tromagnetics. IEEE, 2006, pp. 320–323.

[6.20] D. M. Goebel and I. Katz, *Fundamentals of Electric Propulasion*. Hoboken, NJ, USA: John Wiley & Sons, Inc., 2008.

[6.21] D. De Cogan and A. De Cogan, *Applied numerical modelling for engineers*. Oxford: Oxford Univeristy Press, 1997, vol. 11, no. 5.

[6.22] P. D. Desai, H. M. James, and C. Y. Ho, "Electrical resistivity of aluminum and manganese," *Journal of Physical and Chemical Reference Data*, vol. 13, no. 4, p. 1131, 1984.

[6.23] A. Elkalsh, A. Vukovic, P. Sewell, and T. M. Benson, "Coupled arc discharge models in the TLM method," in *2015 IEEE International Symposium on Electromagnetic Compatibility (EMC)*. IEEE, 2015, pp. 987–990.

[6.24] S. J. Orfanidis, *Electromagnetic Waves and Antennas*, 2014 last Accessed 18/01/2016. [Online]. Available: http://www.ece.rutgers.edu/{~}orfanidi/ewa/

[6.25] W. Benenson, J. w. Harris, H. Stocker, and H. Lutz., Eds., *Handbook of Physics*, 1st ed. New York: Springer-Verlag, 2002.

[6.26] N. Petrov, A. Haddad, G. Petrova, H. Griffiths, and R. Waters, "Study of Effects of Lightning Strikes to an Aircraft," in *Recent Advances in Aircraft Technology*. InTech, 2012.

7

Conclusions and future work

This chapter highlights the significant outcomes and the major contribution of this thesis along with overall concluding statements. Suggested future work directions are discussed, highlighting the limitations of the presented model and potential advancements.

* * *

7.1 Overview of the thesis

The aim of the research presented in this thesis was to develop a two dimensional (2D) coupled electro-thermal numerical model using the transmission line modelling (TLM) method. This model aimed to include non-linearity and multi-physics features of lightning strikes and other engineering problems such as plasmonic nano heat sources.

In chapter 1, the aim of this research was presented demonstrating the motivation to conduct this study. In this chapter a general overview of electro-thermal problems such as lightning, arc discharge and plasmonic nano-heat sources was outlined. This

was followed by a detailed explanation of the methodology in chapters 2 to 4 where the foundation of numerical modelling using the TLM method was introduced for electromagnetic (EM) and thermal TLM modelling. In these three chapters, the analogy between circuit theory and the wave and thermal equation was presented highlighting the main differences between EM and thermal modelling. The modelling of different materials in the EM and thermal TLM method was outlined using the capacitive stub technique. The plasma EM model was introduced illustrating the non-linear and frequency dependent nature of plasma. Heat source scaling while using different mesh sizes was presented in chapter 4, demonstrating the importance of the node depth when modelling a 2D thermal problem.

Chapters 5 and 6 represented the main contribution of this thesis where the electro-thermal TLM model was applied to different engineering applications. In chapter 5, a non-linear TLM plasma model was coupled with electro-thermal TLM to model a plasmonic waveguide with a tapered termination that was submerged in gold. In this particular plasmonic waveguide, the operating signal beam was focused at the end of the tapered waveguide converting the power loss to a nano-scale heat source. The presented results, using the electro-thermal TLM model, compared very well with the experimental results obtained from [7.1]. The electro-thermal coupled model used in chapter 5 was a partially coupled model i.e. the EM material properties were not updated using the temperature profile obtained from the thermal model. This partially coupled approach was chosen due to the fact that the temperature range was not high enough to cause a significant change in the EM properties. The electro-thermal coupling was limited to the use of the electrical power loss as an input heat source in the thermal model. Increasing the computational efficiency was investigated by using different coupling intervals between the EM and thermal model. It was shown that, the accuracy of the model was maintained whilst using longer coupling intervals that did not exceed 625 electrical time steps. This chapter provided a way of testing and validating the developed electro-thermal model on

a stable physical phenomenon before applying it to a more volatile and non-linear physical phenomena such as arc discharge and lightning.

In chapter 6, arc discharge was modelled using the coupled electro-thermal model. This model consisted of an air gap between aluminium electrodes which was subject to an intense electric field that had a similar waveform to a typical double exponential lightning current [7.2]. The intense electric field build up in the air gap resulted in an arc discharge by forming a conduction channel between the electrodes. The development of these conductive non-linear (plasma) channels between the electrodes was modelled entirely based on the electro-thermal analysis. The power loss in the plasma channels and metal electrodes were fed as an input heat source to the thermal model. The model self-consistence and convergence was obtained and demonstrated. Due to the high energy content and thermal energy, a fully coupled approach between the EM and thermal models was implemented. This allowed the EM material properties of plasma and aluminium to be dependent on the temperature profile obtained from the thermal model. In this chapter, different initial parameters for plasma were enforced to investigate the suitability of both the fully and the partially coupled approaches.The partially coupled approach only used the EM power loss as an input for the thermal model, while the fully coupled approach extended the calculations to use the thermal profile from the thermal model to update the EM material properties. The model was then applied to segmented strips where an arc discharge was modelled in cascaded multiple air gaps. The plasma channels' development over time was shown in these air gaps. Also this chapter highlighted some of the model limitations, such as the instability encountered when different coupling intervals between EM and thermal model were chosen. In this particular model, the encountered instability forced the EM and thermal time step to have the same time step for accurate simulation.

7.2 Future work

The proposed electro-thermal TLM model describedin this thesis can be used as a foundation to implement more complex models for lightning and arc discharge. Suggested improvements and further model developments are highlighted in this section.

In nature, a material's thermal properties are generally temperature dependent; this becomes an important factor in the model when modelling a problem that involves a wide range of temperatures such as the modelling of an arc discharge. An assumption was made in this thesis, in eq. (3.13), that the thermal properties such as thermal conduction, heat capacitance are fixed and temperature independent. Updating the material properties included in the model based on the thermal profile is a suggested area of development that can add more accuracy to the model.

Conduction is the only method of heat transport that was considered in this thesis; this represents a limitation to the model especially where fluids such as air and gaseous plasma are present in the problem under consideration. Convection is the main method of heat transport in fluids. In TLM, modelling the steady state convection has been implemented in [7.3]. The TLM convective boundary conditions were demonstrated in [7.4]. The assumption of ignoring the thermal convection in the arc discharge model, showed some non realistic features in the results, as was discussed in section 6.3. Therefore including convection in the coupled model can be considered a major future enhancement to the model, and would allow for a direct validation against experimental data such that obtained from welding arcs.

In this thesis, once the plasma channels are created using the intense electric field, its existence was assumed valid until the end of the simulation time, even after the disappearance of the EM source. In reality plasma starts to cool down and lose energy either by emitting photons or by heat diffusion to the surroundings. Even-

tually, the plasma becomes ionized air that does not have enough free electrons to conduct and sustain an electric field. Depending on the wave form of the excitation source in the EM model, switching off the plasma channel based on its temperature profile can lead to a series of triggering the plasma channel on and off. This is an interesting area of research that can be investigated.

Due to the big difference between the EM and thermal response time, the coupling between EM and thermal model using the same time step is a very computationally expensive task that was highlighted throughout this thesis. A suggested approach might be adapted from the corresponding finite difference time domain (FDTD) method version in [7.5,7.6]. This approach is suitable for modelling problems where the excitation source has a slow relaxation time, i.e., it reaches the peak value quickly but it decays at a much slower rate after that. The idea of this approach is to use a material with higher permittivity than the free space as a background material. This allows the model time step to be much higher than if free space was selected as background material. A scaling step for the fields is necessary after the simulation to mimic the results of using free space as background material. Introducing this approach to the TLM could be very beneficial.

The upgrade of the electro-thermal 2D-TLM model to a three dimension(3D) model is another area of development that can be suggested. The arc discharge model in this thesis described a 2D problem which introduces a limitation on the direction and the size of the plasma channel that could be studied. In reality, the 3D structure affects the plasma channels formation. The model upgrade to a 3D case will represent a challenge from a computational power point of view due to the big difference between the electrical and thermal time steps.

This concludes the suggested future work and the thesis as a whole.

References

[7.1] B. Desiatov, I. Goykhman, and U. Levy, "Direct temperature mapping of nanoscale plasmonic devices." *Nano Letters*, vol. 14, no. 2, pp. 648–52, 2014.

[7.2] W. Jia and Z. Xiaoqing, "Double-exponential expression of lightning current waveforms," in *The 2006 4th Asia-Pacific Conference on Environmental Electromagnetics*. IEEE, 2006, pp. 320–323.

[7.3] A. Kennedy and W. J. O. Connor, "A transmission line modelling (TLM) method for steady-state convection diffusion," *International Journal for Numerical Methods in Engineering*, vol. 72, no. 9, pp. 1009–1028, 2007.

[7.4] D. De Cogan, *Transmission Line Matrix (TLM) techniques for diffusion applications*. Amesterdam, The Netherlands: Gordon and Breach Science Publishers, 1998.

[7.5] R. Holland, "FDTD analysis of nonlinear magnetic diffusion by reduced c," *IEEE Transactions on Antennas and Propagation*, vol. 43, no. 7, pp. 653–659, 1995.

[7.6] ——, "Analysis of Magnetic Diffusion," vol. 36, no. 1, pp. 32–39, 1994.